Numerical Study of Two-Phase Turbulent Flow in Hydraulic Jumps

Seyedpouyan Ahmadpanah

A Thesis

In

The Department

Of

Building, Civil and Environmental Engineering

Presented in Partial Fulfilment of the Requirements

For the Degree of Master of Applied Science in Civil Engineering at

Concordia University

March 2017

CONCORDIA UNIVERSITY
School of Graduate Studies

This is to certify that the thesis prepared

By: Seyedpouyan Ahmadpanah

Entitled: Numerical study of two-phase turbulent flow in hydraulic jumps

and submitted in partial fulfillment of the requirements for the degree of

Master of applied science in civil engineering

complies with the regulations of the University and meets the accepted standards with respect to originality and quality.

Signed by the final examining committee:

Dr. C. Alecsandru Chair

Dr. A. Nazemi Examiner

Dr. A. Dolatabadi Examiner

Dr. S. Li Supervisor

Approved by _____
Chair of Department or Graduate Program Director

_____
Dean of Faculty

Date _____

Abstract

Numerical Study of Two-Phase Turbulent Flow in Hydraulic Jumps

Seyedpouyan Ahmadpanah

Hydraulic jump is a rapidly varied flow phenomenon that the flow changes suddenly from supercritical to subcritical. Hydraulic jumps are frequently observed to exist in natural river channels, streams, coastal water, and man-made water conveyance systems. Because of a sudden transition of flow regime, hydraulic jumps result in complex flow structures, strong turbulence, and air entrainment. Accordingly, they are two-phase flow, with air being the gas phase and water being the liquid phase. Consequences of the occurrence of hydraulic jumps include: unwanted fluctuations in the water surface with unstable waves and rollers, undesirable erosion of channel sidewalls and channel bottom, and reduced efficiency for water conveyance systems. Thus, it is important to study various aspects of the phenomenon.

So far, knowledge of the phenomenon is incomplete. The main objective of this research is to improve our understanding of the complex flow structures and distributions of air entrainment in a hydraulic jump. Previously, both experimental and computational studies of the phenomenon have typically suffered a scale problem. The dimensions of the setup being used were unrealistically too small.

In this research, we took the computational fluid dynamics (CFD) approach, and simulated hydraulic jumps at relatively large and practical dimensions. This would help reduce artificial scale effects on the results. On the basis of Reynolds averaged continuity and momentum equations, CFD simulations of hydraulic jumps were performed for four different cases in terms of the approach flow Froude number Fr_1, ranging from 3.1 to 5.1. The Reynolds number is high (between 577662 and 950347), which ensures turbulent flow conditions. The CFD model channel is discretized into 2,131,200 cells. The mesh has nearly uniform structures, with fine spatial resolutions of 2.5 mm. The volume of fluid method provides tracking of the free surface. The standard k-ε turbulence model provides turbulence closure.

For each of the simulation cases, we carried out analyses of time-averaged air volume fraction, time-averaged velocity, time- and depth-averaged (or double averaged) air volume fraction at a series of locations along the length of the model channel (Note that the terms air volume fraction

and void fraction are used interchangeably in this thesis). We compared the CFD predictions of air volume fraction with available laboratory measurements. It is important to note that these measurements were made from laboratory experiments that corresponded to essentially the same values of Fr as this CFD study, but used a channel of smaller dimensions, in comparison to the CFD model channel. The CFD results of time-averaged air volume fraction are reasonable, when compared to the experimental data, except for the simulation case with $Fr_1 = 3.8$. For all the four simulation cases, the predicted variations in air volume fraction show a trend in consistency with the experimental results. For the three simulation cases (with $Fr_1 = 3.1$, 3.8 and 4.4), the time-averaged air volume fraction in the hydraulic jumps is larger at higher Reynolds number. However, for the simulation case with $Fr_1 = 5.1$, it is smaller at higher Reynolds number. This implies that the amount of air being entrained into a hydraulic jump depends on not only Fr_1 but also the depth of the approach flow. In future studies of the hydraulic jump phenomenon, one should consider using approach flow of realistically large dimensions at various values of Fr_1, for realistic predictions of air entrainment in hydraulic jump rollers.

Acknowledgment

I would like to express my gratitude to my supervisor, Dr Samuel Li. His guidance, encouragement and support throughout the research are greatly appreciated. His abundant help and invaluable assistance, support and guidance in preparing my thesis, are especially appreciated. I am truly fortunate to have such an excellent supervisor.

I would like to thank my dear parents and sister for their endless love and support through the whole duration of my studies.

I will forever be thankful to my supportive friends Parisa Moslehi and Ali Izadpanah.

Table of Contents

List of Figures

List of Tables

List of Symbols

A	flow cross section area (m^2)
$\vec{A}$	cell cross section area related to the direction of $\vec{v}$ (m^2)
C	air volume fraction
C_{max}	maximum air volume fraction in the shear region of a hydraulic jump
C_{mean}	depth-averaged time-averaged air volume fraction
$C_{\varepsilon 1}$	$k-\varepsilon$ model constant
$C_{\varepsilon 2}$	$k-\varepsilon$ model constant
C_{μ}	$k-\varepsilon$ model constant
$C_{\mu w}$	wall function constant
D_t	turbulent diffusivity of air bubbles in air-water flow (m^2/s)
E	specific energy (m)
e	total energy (J)
E^*	empirical constant
F	bubble frequency defined as the number of detected air bubbles per unit time (Hz)
f	force (N)
F_{max}	maximum bubble frequency (Hz)
F_s	specific force (m^3)
Fr	Froude number

g	gravitational acceleration (m/s^2)
$\vec{g}$	gravitational acceleration (m/s^2)
h_l	energy head loss (m)
k	kinetic energy of turbulent fluctuations per unit mass (m^2/s^2)
κ	von Kármán constant
k_{ac}	turbulent kinetic energy at the wall adjacent cell centroid (m^2/s^2)
k_{eff}	effective thermal conductivity (W/m.K)
L	length (m)
$\dot{m}$	mass flow rate (kg/s)
Nw	weber number
p	pressure (pa)
p_0	total gage pressure with respect to the operating pressure (pa)
p_s	hydrostatic pressure with respect to the operating pressure (pa)
Q	flow discharge (m^3/s)
q	discharge per unit width (m^2/s)
Re	Reynolds number
S_{ij}	mean strain rate tensor (s^{-1})
s_{α_q}	source term of phase q, the mass of phase q which is added to the continuous phase per unit time (kg/s)
T	temperature (°C)

t	time (s)
U	volume flux ($m^3.s^{-1}.m^{-2}$)
U^*	dimensionless velocity
U_{ac}	mean velocity of fluid at the wall adjacent cell centroid (m/s)
$\overline{u_i' u_j'}$	temporal average of fluctuating velocities (m2/s2)
V	air-water velocity (m/s) or average flow velocity (m/s)
$\vec{v}$	velocity vector (m/s)
v	fluid velocity at the inlet (m/s)
V_{max}	maximum velocity in the x direction (m/s)
V_x	velocity in the x direction (m/s)
Vol	fluid volume (m^3)
x	horizontal distance from the inlet (m)
x_1	horizontal distance of the jump toe from the inlet (m)
x_i	position vector in tensor notation
y	vertical distance measured from the channel bed (m) or depth of water (m)
y^*	dimensionless distance from the wall
$Y_{0.5}$	vertical distance from the point where $V_x = V_{max}/2$ to the channel bed (m)
y_{90}	vertical distance from the point where $C = 0.9$ to the channel bed (m)
y_{ac}	distance from the centroid of the wall adjacent cell to the wall (m)

$\bar{y}_{ac}$	the mean of y_{ac} s of all the cells adjacent to the wall (m)
y_c	critical depth (m)
$Y_{C_{\max}}$	vertical distance from the point where $C = C_{\max}$ to the channel bed (m)
$Y_{F_{\max}}$	vertical distance from the point where $F = F_{\max}$ to the channel bed (m)
Y_{shear}	vertical distance of turbulent shear region upper boundary from the channel bed (m)
$Y_{V_{\max}}$	vertical distance from the point where $V_x = V_{\max}$ to the channel bed (m)
z	vertical distance from the free surface level to the centroid of the flow section (m)
α	volume fraction
Δ	change in variable
δ	boundary layer thickness (m)
ε	energy dissipation per unit mass (m^2/s^3) (W/kg)
μ	dynamic viscosity ($N.s/m^2$)
ν	kinematic molecular viscosity (m^2/s)
ν_T	kinematic eddy viscosity (m^2/s)
ρ	density of water (kg/m^3)
σ	surface tension (kg/m)
σ_k	$k-\varepsilon$ model constant
σ_ε	$k-\varepsilon$ model constant
τ_{ij}	specific Reynolds stress tensor (m^2/s^2)

τ_w	surface shear stress (N/m^2)

Subscripts:

1	upstream cross section
2	downstream cross section
a	related to phase a (fluid) in simulation
b	related to phase b (fluid) in simulation
f	related to face of the cell
m	model
p	related to the p^{th} phase (fluid) in simulation
pq	phase p to phase q
pr	prototype
q	related to the q^{th} phase (fluid) in simulation
qp	phase q to phase p
r	prototype to model ratio

Superscripts:

n	previous time step
$n+1$	new time step

Chapter 1 Introduction

1.1 Background

The hydraulic jump is a flow feature through which the flow of water transfers abruptly from the supercritical to the subcritical condition (Figure 1.1). The sudden change of flow regime is companied by considerable turbulence, loss of flow energy, and entrainment of air mass from above the water surface. Hydraulic jumps are frequently observed to occur in rivers (Figure 1.2), natural streams (Figure 1.3), lakes, coastal water, and man-made water conveyance systems (Figure 1.4). They even occur in kitchen sinks. Hydraulic jumps are classified as rapidly varied flow, as opposed to gradually varied flow. They can be free surface flow or submerged flow below the water surface. Along the length of a hydraulic jump, there is a continuous transition from high flow velocity to low flow velocity, with a corresponding increase in the depth of flow.

The phenomenon of hydraulic jumps is very common in natural water streams and man-made water channels, as shown in Figures 1.1–1.4. Hydraulic jumps have been receiving extensive research attention because of their engineering relevance. However, most of the existing studies of hydraulic jumps have considered the flow as single phase liquid flow, and unrealistically ignored air bubbles [Figure 1.1(b)] as the gas phase.

In Figure 1.2, hydraulic jumps are shown to occur after a dam chute on a natural stream in Australia. It is clear that the river flow was accompanied by river sediment suspension/re-suspension, and channel erosion. The obstacles were built in the flow path to form hydraulic jumps right after the chute. The idea was to make hydraulic jumps in a desired location, and to dissipate the energy of the high speed flow through the jumps. This would prevent the channel downstream of the dam from erosion. In natural streams, hydraulic jumps can occur due to natural obstacles at the bottom of the stream (Figure 1.3), and cause changes to the stream geometry. Such changes may have important implications to the health of the habitats of aquatic species.

The design and operation of water conveyance system must pay close attention to distributions and losses of flow energy. In Figure 1.4, a hydraulic jump is seen immediately downstream of a weir in a water conveyance system. Turbulent motions associated with hydraulic jumps (Figures 1.1 and 1.4) cause considerable loss of flow energy. The losses of flow energy due to the occurrence of hydraulic jump in water conveyance systems affects the efficiency of the systems. Thus, the energy losses need to be taken into account in the design of the systems.

(a)

(b)

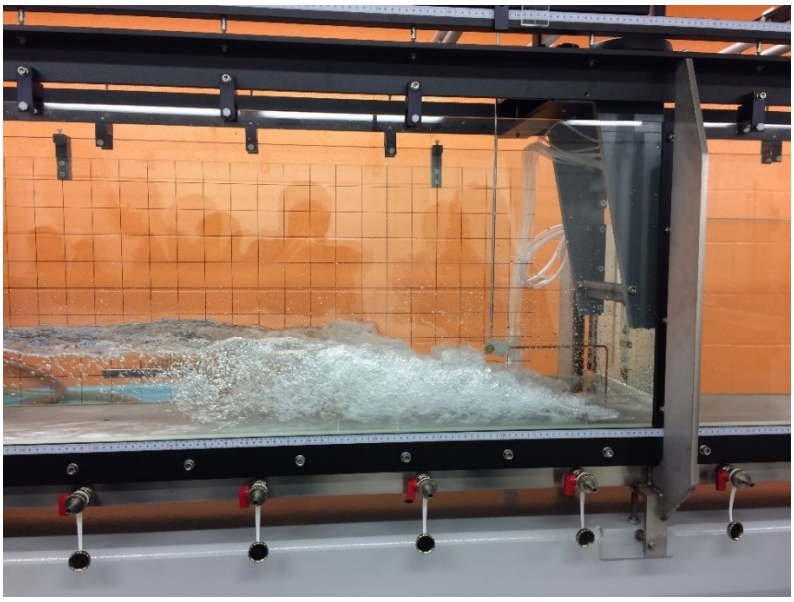

Figure 1.1 Photo of the experimental setup in Concordia University's Water Resources Engineering Laboratory: (a) a rectangular recirculation flume; (b) hydraulic jump as bubbly flow. The direction of flow was from right to left. A control sluice gate allowed a small opening and produced supercritical flow downstream of itself. At the downstream end of the flume, a control tail gate was raised, producing subcritical flow upstream of itself. The two controls created the hydraulic jump. There is an exchange of air mass across the flow surface, with a net entrainment of air mass into the flow, forming air bubbles in the flow.

Figure 1.2 Burdekin dam on the Burdekin River in Queensland, Australia, showing hydraulic jumps induced by obstructions and a gradient change. (http://www.abc.net.au/news/2016-05-26/the-burdekin-falls-dam-spills-over-as-cyclone/7446962, accessed on February 26, 2017)

Figure1.3 Hydraulic jump on the Naramatagawa River's stream. (https://commons.wikimedia.org/wiki/File:Hydraulic_jump_on_Naramatagawa_River's_stream.JPG, accessed on February 27, 2017)

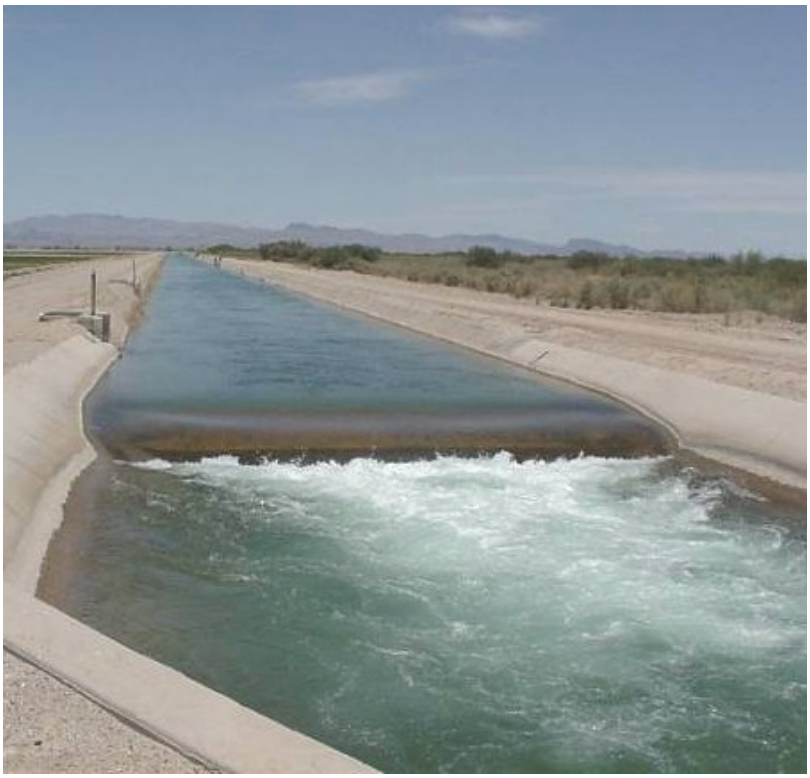

Figure1.4 Hydraulic jump downstream of a weir in an open channel. (http://www.itrc.org/projects/flowmeas.htm, access on september 2, 2016)

The transition of shallow, fast flow to deep, slow flow through a hydraulic jump features extreme chaos, large scale turbulence, surface waves, and spray. Because of the highly turbulent flow condition in hydraulic jumps, air mass immediately above the flow surface will enter the flow. Thus, the flow becomes two phase flow, with water as the liquid phase and air as the gas phase. The exchange of air mass between the atmosphere and water is known as air entrainment (or bubble entrainment or aeration). The presence of air in the flow makes it difficult to determine the exact location of the interface between the flowing fluids and the atmosphere above. Besides, there is a continuous exchange flux of liquid and air between the flow and the atmosphere. The resulting air-water mixture consists of both air pockets within water and water droplets surrounded by air. There are also spray, foam, and complex air water structures. In all situations, the flow is constituted of both air and water.

On the basis of the Reynolds number (Reynolds 1883), fluid flows are distinguished into laminar (or smooth) flow and turbulent (or chaotic) flow. There are significant challenges in

realistically predicting turbulent flows because of their irregular chaotic motions, strong mixing properties, and a broad spectrum of length scales. Knowledge of hydraulic jumps with the above mentioned complexities is far from complete.

In a hydraulic jump, at any point, the fluid velocity changes continuously in both magnitude and direction (Chanson 1996, p. 4). The air–water flow of a hydraulic jump includes three distinct regions:

a) A recirculation layer at the top where recirculating flow and large eddies occur in this layer. This layer is characterised by the development of large-scale vortexes and bubble coalescence with a foam layer at the free surface with large air polyhedral structures;
b) A turbulent shear layer or air diffusion layer with air bubbles of smaller sizes and high air content;
c) An impingement jet region at the bottom of shear layer which has a velocity distribution similar to the upstream flow and less or no air bubble can be seen in this region.

The extremely turbulent flow is associated with large scale vortexes. These vortexes and the non-stable dynamic velocity produce significant pressure pulsation and develop a wavy flow. All these characteristics results in a wild and erosive flow, which can cause erosion on non-protected open channel beds and walls, and transport and can mix a large amount of sediments with the flowing water. The resultant high turbidity will deteriorate water quality. Also, the turbulent and wavy flow produces a clearly detectable sound and converts a relatively large amount of energy into heat.

In water conveyance settings, the study of hydraulic jumps in open channels has many important applications. Examples include:

a) Reduction of excessive energy of flowing water for the safety of hydraulic structures. In certain part of an open channel system with a steep bed slope, the flow gains velocity. At high velocity, the flow becomes erosive or destructive. The use of hydraulic jump in such situation will dissipate the extra amount of flow energy and hence avoid destructive effects;
b) Efficient mixing of chemicals in water treatment plants. The use of hydraulic jump represents a very suitable method for mixing chemical substances required in the process of water treatment. The macro-scale vortexes in the hydraulic jump increase the efficiency of mixing procedures;

c) Discharge measurements. In Parshall flumes (Chow 1959), a hydraulic jump is produced for determining flow discharge by measuring the depth of water at certain locations.

Clearly, there are beneficial applications of hydraulic jump as well as undesirable consequences of their occurrences such as erosion in erodible channels or turbulent disturbances in water conveyance systems. There is a need for improved understanding of various aspects of the hydraulic jump phenomenon.

Classic studies solved the problem of hydraulic jumps as one-dimensional flow using the continuity and momentum principles. The solution approach is overly simplified, without dealing with turbulence. The present knowledge of the turbulent flow field is fairly limited, especially under environmental and geophysical flow conditions (Chanson 2009). After extensive research, the hydraulic jump phenomenon remains a fascinating flow motion, and the present knowledge is insufficient in several aspects, including air entrainment, turbulence, and undular flow.

This present research work focuses on distributions of air entrainment in hydraulic jumps at high Reynolds numbers. The consideration of high Reynolds numbers will better reflect real-world conditions under which hydraulic jumps occur in open channels and water conveyance systems. This represents an extension of the previous studies, most of which used laboratory or numerical models of small length scales. The results from these studies have inevitably suffered from a scale problem. In the laboratory experiments reported in the literature, the Reynolds number was typically much smaller than real-world jumps in irrigation and water conveyance systems. The use of high Reynolds numbers in this study will improve the relevance to reality.

1.2 Specific aims of this research work

The specific objectives of this research work are as follows:

- To produce the hydraulic jump as two-phase flow in a large-scale channel at high Reynolds numbers. This will minimise scale effects.
- To quantify the distributions of air volume fraction in hydraulic jump rollers in a range of Froude numbers. Air volume distributions in the flow give rise to non-hydrostatic pressure. A good understanding of the distributions represents a significant improvement from the traditional simplification of hydrostatic pressure (no air bubbles) field in hydraulic jumps.

- To establish suitable computational procedures for predicting air entrainment in hydraulic jumps. The suitability is to be confirmed by comparing air entrainment between the computer model and existing laboratory experiments.
- To quantify the average percentage of air in hydraulic jumps in a range of Froude numbers.
- To reveal the vertical structures of flow velocity along hydraulic jump rollers in a range of Froude numbers.

1.3 Scope of this research work

To achieve the above-mentioned objectives, the rest of this thesis is organized as follows: Chapter Two will introduce the classical theory and basic characteristics of hydraulic jumps. The chapter will discuss the similitude of models for hydraulic jumps, and will provide highlights of the previous experimental and numerical studies of air entrainment in hydraulic jumps. Outstanding issues will be outlined.

Chapter Three will discuss on modelling methodologies. The chapter will give a description of the model domain and geometric setup. Discussions of the modelling methodologies will cover the volume of fluid method, and the standard k-ε model for turbulence closure. The chapter will provide details of computational mesh configuration for hydraulic jump simulations, treatment of open boundary conditions, and specification of initial conditions.

Chapter Four will present the computational results, along with a comparison with available experimental data. The results will the flow velocity field, distributions of air volume fraction, flow surface profile, and turbulence kinetic energy. The characteristics of the above-mentioned quantities at different Froude numbers will be discussed in details. The comparison will make use of the experimental data from Chachereau & Chanson (2010). Through the comparison, we will investigate the effects of Reynolds number on air entrainment.

In Chapter Five, conclusions will be drawn, and suggestions for future studies of hydraulic jumps as two-phase flow will be outlined.

1.4 Highlights of research contributions

New contributions from this research work are highlighted below:

(1) Reliable predictions of hydraulic jumps as two-phase bubbly flow at high Reynolds numbers, which has not been achieved in previous studies.

(2) Quantitative details of the flow field and air entrainment distributions that are difficult to measure from laboratory experiments.

(3) An improved understanding of the effects of the Reynolds number on air entrainment in oscillating and steady hydraulic jumps. This is of practical importance to the design of appropriate laboratory setup for hydraulic jump experiments.

(4) The establishment of suitable computational procedures for numerical simulations of hydraulic jumps and the determination of time averaged variables related to the jumps.

Chapter 2 Review of the Pertinent Literature

2.1 The classical theory of hydraulic jumps

Open-channel flow can change from a subcritical state to a supercritical state and vice versa, in response to certain changes in channel geometry or flow boundary conditions or both. Changes from a subcritical to supercritical state usually occur rather smoothly via critical depth. However, changes from a supercritical to subcritical state occurs abruptly through a hydraulic jump (Figure 2.1). The depth of flow changes from y_1 to y_2, known as the initial depth of flow before the jump and the sequent depth of flow after the jump.

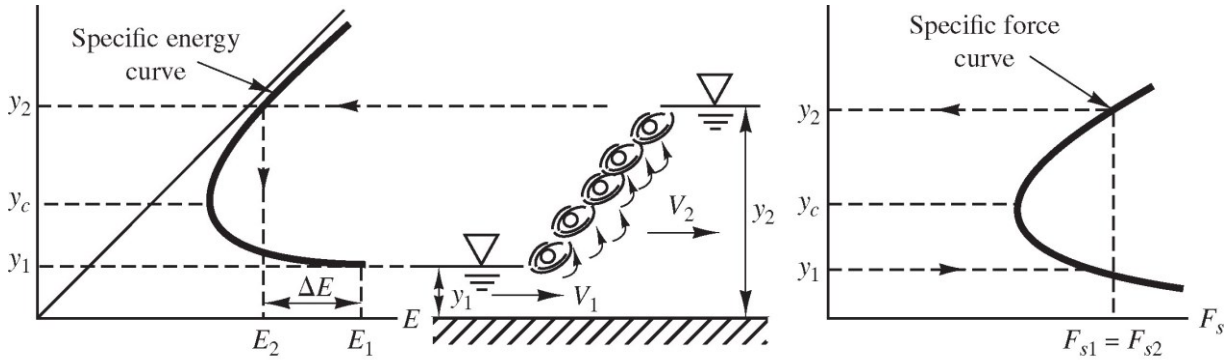

Figure 2.1 Specific energy diagram, hydraulic jump and specific force diagram (adopted from Houghtalen et al. 2017).

Hydraulic jumps are highly turbulent, with complex internal flow patterns, and dissipate considerable flow energy. Thus, we expect the flow energy to be much lower downstream of a jump than upstream, but have no prior knowledge about the actual amount of energy losses in the jump. Thus, it is difficult to solve the problem of hydraulic jumps by directly using the energy principle. The classical theory of hydraulic jump uses the momentum principle, expressed as (Henderson 1966, p. 74):

$$\frac{Q}{gA_1} + z_1 A_1 = \frac{Q}{gA_2} + z_2 A_2 \tag{2.1}$$

where the subscripts 1 and 2 refer to the flow sections before and after the jump, respectively; Q is the discharge; g is the acceleration of gravity; z is the vertical distance from the free surface level

to the centroid of the flow section; and A is the flow area. Gravity is an important parameter for the problem of hydraulic jumps because the flow has a free surface (Figure 2.1).

Equation (2.1) has assumed: a) The frictional forces at the channel bed and on the channel sidewalls are negligible; b) there are no external forces other than pressure forces; c) the channel has a horizontal bed; and d) the flow is incompressible. The sum of the two terms on each side of Equation (2.1) is known as the specific momentum F_s. Thus, the two flow sections before and after the hydraulic jump, respectively, have the same specific momentum:

$$F_{s1} = F_{s2} \tag{2.2}$$

For given hydraulic conditions and channel geometry, Equation (2.2) can be solved analytically to yield the relationship between y_1 and y_2 (Figure 2.1). Then, the energy equation can be used to determine the amount of flow energy losses in the hydraulic jump.

2.2 Hydraulic jump in rectangular channels

For hydraulic jumps in a horizontal, rectangular channel, Equation (2.1) is reduced to:

$$\left(\frac{q^2}{gy_1} + \frac{y_1^2}{2}\right) = \left(\frac{q^2}{gy_2} + \frac{y_2^2}{2}\right) \tag{2.3}$$

where q is the discharge per unit width of channel. Solving Equation (2.3) yields (Henderson 1966, p. 69):

$$y_2 = \frac{y_1}{2}\left(\sqrt{1 + 8Fr_1^{\,2}} - 1\right) \tag{2.4}$$

or

$$y_1 = \frac{y_2}{2}\left(\sqrt{1 + 8Fr_2^{\,2}} - 1\right) \tag{2.5}$$

where Fr_1 is the upstream Froude number; and Fr_2 is the Froude number after the jump. Fr_1 is given by:

$$Fr_1 = \frac{V_1}{\sqrt{gy_1}} \tag{2.6}$$

where V_1 is the depth of flow at upstream, which is related to q and y_1 as $V_1 = q/y_1$. Similarly, Fr2 is given by:

$$Fr_2 = \frac{q}{\sqrt{gy_2^{\,3}}} \tag{2.7}$$

The Froude number is an important parameter for the hydraulic jump phenomenon, and therefor the gravity plays a significant role in studying the hydraulic jump phenomenon.

This well-known dimensionless parameter in free surface flow represents the ratio of the inertial force in the flow to gravity force.

For a given initial depth, y_1, of flow before the jump (Figure 2.1), the sequent depth, y_2, of flow after the jump can be determined from Equation (2.4), and vice versa from Equation (2.5). The amount of energy head losses, h_l, in the hydraulic jump is given by:

$$h_l = \left(\frac{q^2}{2gy_1^2} + y_1\right) - \left(\frac{q^2}{2gy_2^2} + y_2\right) \tag{2.8}$$

or equivalently

$$h_l = \frac{(y_2 - y_1)^3}{4y_1 y_2} \tag{2.9}$$

2.3 Basic characteristics of hydraulic jumps in rectangular channels

Akan (2011, p. 238) provided a description of a series of tests by U.S. Bureau of Reclamation (1987) to study the hydraulic jumps. The results of these tests show that the shape, form and characteristics of hydraulic jumps depend on Fr_1 (Equation 2.6). In Figures 2.2(a)-2.2(d), hydraulic jumps are classified based on Fr_1.

(a) Form A: $1.7 < Fr_1 < 2.5$

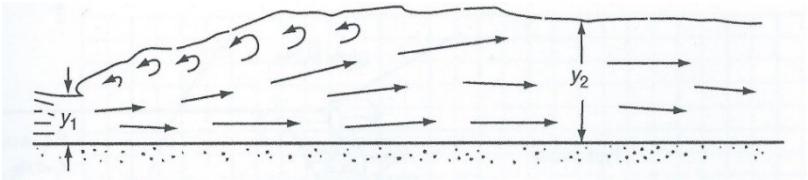

(b) Form B: $2.5 < Fr_1 < 4.5$

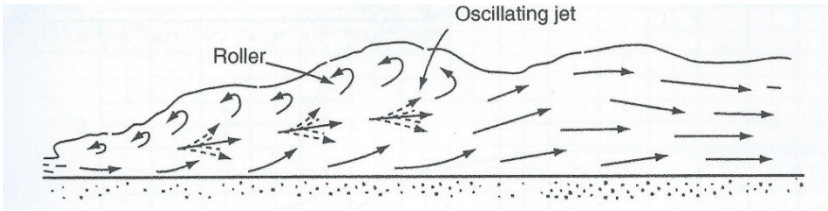

(c) Form C: $4.5 < Fr_1 < 9.0$

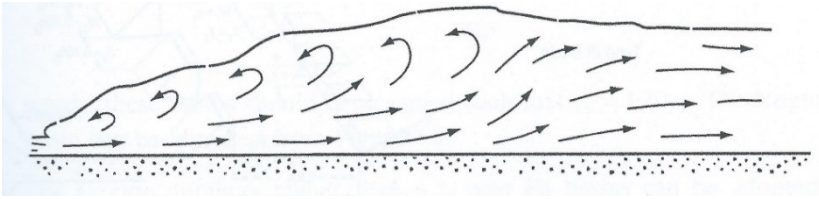

(d) Form D: $Fr_1 > 9.0$

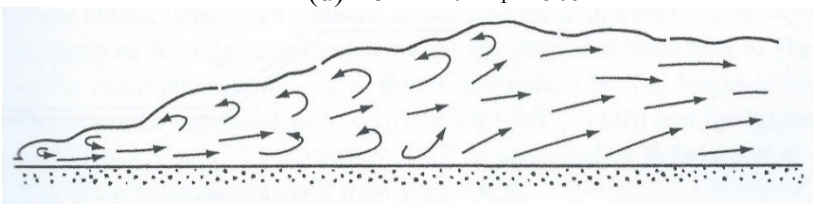

Figure 2.2 Classifications of hydraulic jumps according to the upstream Froude number Fr_1 (adopt from US Bureau of Reclamation 1987).

For $1 < Fr_1 < 1.7$, the approach flow depth is only slightly less than the critical depth. From this transition of a supercritical to subcritical stage, the flow changes gradually with a very slight turbulent water surface. Some small rollers begin to form on the surface as Fr_1 approaches 1.7. The change becomes more intense with increasing upstream Froude number. Except the existence of surface rollers, relatively smooth flows predominate at Froude numbers up to about 2.5. Hydraulic jumps with Froude numbers between 1.7 and 2.5 are characterize as form A [Figure 2.2(a)].

For $2.5 < Fr_1 < 4.5$, the hydraulic jump has the characteristics of oscillating flow. This oscillating flow has undesirable and sometimes significant surface waves that carry far downstream. The hydraulic jumps for this range of upstream Froude numbers are classified as form B [Figure 2.2(b)].

For $4.5 < Fr_1 < 9.0$, the hydraulic jump is well-balanced and stable in place. Turbulence is limited to the main body of the hydraulic jump, and the water surface downstream is relatively smooth. The hydraulic jumps in this range of upstream Froude numbers are considered as form C and are called steady jumps [Figure 2.2(c)].

For $Fr_1 > 9.0$, the turbulence through the hydraulic jump and the surface rollers become significantly active. This causes a jump with a rough water surface and with strong water waves carry downstream from the jump. This kind of hydraulic jump is called strong jump and is classified as form D [Figure 2.2(d)].

2.4 Similitude of models for hydraulic jumps

General discussions about hydraulic similitude can be found in Houghtalen et al. (2017). Hydraulic modelling of a prototype must ensure three types of similarities as listed below: geometric similarity, kinetic similarity, and dynamic similarity. The geometric similarity is the similarity of form. It means that when a prototype size is reduced, the homologous lengths must have a fixed ratio between the hydraulic model and prototype. In this connection, there are three physical factors involved in geometric similarity: length, area, and volume.

The kinematic similarity is the similarity of motion. This similarity will be achieved when the homologous moving particles moving through geometrically similar paths have similar velocity ratios between the hydraulic model and prototype. This type of similarity involves two factors: length and time.

The dynamic similarity is the similarity of forces active in the motion. This similarity will be achieved when homologous forces involved in the motion have a fixed ratio between the hydraulic model and prototype, or:

$$\frac{f_{pr}}{f_m} = f_r \tag{2.10}$$

The study of air entrainment in the hydraulic jump phenomenon involves several kinds of forces in action. The dynamic similarity in hydraulic jump studies requires that the ratio of these forces be kept the same between the model and the prototype. These force ratios are discussed in following sections.

2.4.1 Viscous force – Reynolds number law

Inertial forces are known to always affect water in motion such as in hydraulic jumps (Figure 2.1). Consider that the inertial forces and viscous forces as two kinds of forces act on moving homologous particles in the hydraulic model of hydraulic jumps and prototype hydraulic jumps. The ratio of the two types of forces is defined by Reynolds number law. For applications to hydraulic jumps (Figure 2.1), the Reynolds number base on variables of the approach flow can be expressed as:

$$\mathrm{Re}_1 = \frac{V_1 y_1}{\nu} \tag{2.11}$$

where ν is the kinematic viscosity of water. If the inertial force and the viscous force are the main forces governing the fluid motion, one must keep the same Reynolds number between the model and the prototype (Houghtalen et al. 2017, p. 379).

2.4.2 Gravity force – Froude number law

Gravity is an important parameter for the free surface phenomenon of hydraulic jumps. The ratio of the inertial force to gravity force is defined by the Froude number. The Froude number based on the upstream flow is given in Equation (2.6). To ensure that the behaviour of the model hydraulic jumps reflects that of the prototype jumps, one must retain the same value for the Froude number between a hydraulic model of hydraulic jumps and prototype of hydraulic jumps.

2.4.3 Surface tension – Weber number law

In Houghtalen et al. (2017, p. 383), surface tension is described as a measure of energy level on the surface of a liquid body. Hydraulic jumps are turbulent flow, which entrains air from above the free surface. The entrainment process results in continuous mixing of air and water. This gives rise to surface tension force in hydraulic jumps.

The Weber number defines the ratio of inertial force to surface tension force:

$$Nw = \frac{\rho V L}{\sigma} \tag{2.12}$$

where ρ is the density of the fluid, V is a velocity scale, L is a length scale, and σ is surface tension per unit length. One ought to keep the same value for the Weber number between the hydraulic model and the prototype.

In this research work, the theory for hydraulic jump predictions, to be presented in the next chapter, considers inertial forces, viscous forces, gravity force, and surface tension. All these forces are involved in the governing equations of fluid motions. Thus, to ensure the relevance of predicted hydraulic jump behaviour to a real-world hydraulic jump, it is desirable to use realistic values for the Reynolds number, the Froude number, and the Weber number in the computations.

2.5 Experimental studies of air entrainment in hydraulic jump

Rajaratnam (1962) is probably the first researcher making laboratory measurements of air volume fraction in hydraulic jumps. Resch and Leutheusser (1972) obtained measurements of air entrainment and air volume fraction in the bubbly flow region of a hydraulic jump, using a hot-

film probe. For the first time, they reported the effects of upstream flow conditions on hydraulic jumps. They suggested that the air entrainment process, momentum transfer and energy dissipation are strongly affected by the inflow conditions. In an experimental study, Chanson and Qiao (1994) focused on air-water properties in partially developed hydraulic jumps. Chanson (1995b) reported new experimental data of air bubble diffusion in turbulent shear flows. The author investigated two flow scenarios: a vertical supported jet, and a horizontal hydraulic jump. As an extension of the previous experimental studies, Chanson and Brattberg (2000) investigated air-water flow properties in the shear regions (Figure 2.4) of hydraulic jumps, under the conditions that the upstream Froude number had values of Fr_1 = 6.33 and 8.48. Almost all of the above-mentioned experimental studies used a horizontal, rectangular channel. A definition diagram of hydraulic jump in such a channel is shown in Figure 2.3.

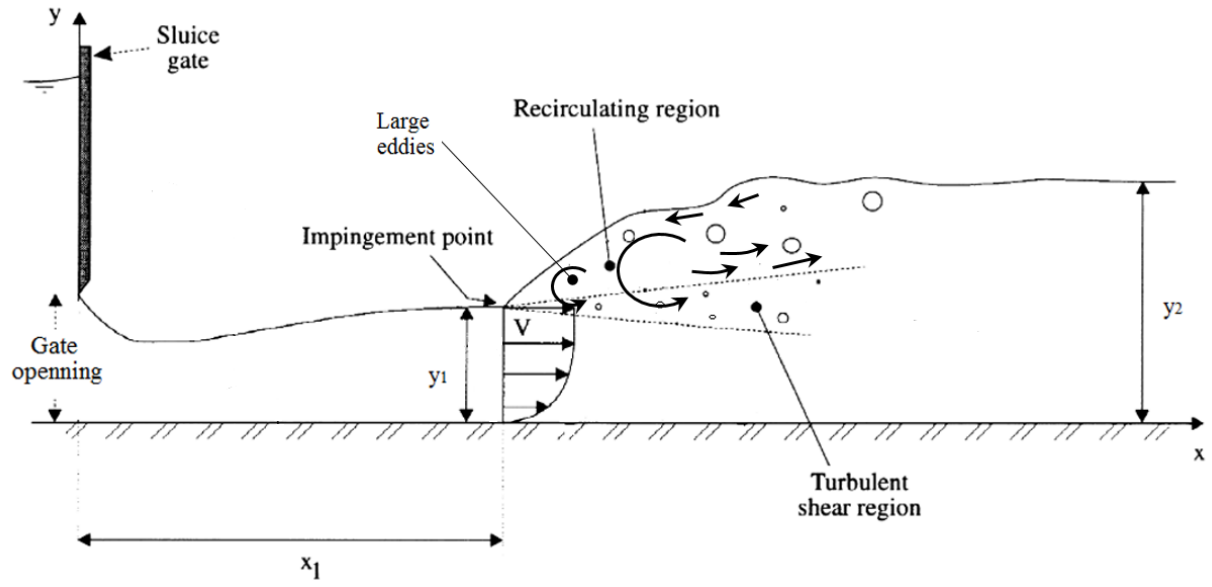

Figure 2.3 Definition diagram of hydraulic jump experiments in a rectangular channel (adopted from Chanson and Brattberg, 2000). Note that *V* represents the flow velocity in the *x*-direction.

Using a dual-tip optical fibre probe, Murzyn *et al.* (2005) obtained measurements of air volume fractions, bubble frequencies and bubble sizes in hydraulic jumps for four different cases of the upstream Froude number Fr_1. The measurements were from a large number of points throughout the jump. The experimental conditions of Murzyn *et al.* (2005) are summarised in

Table 2.1. Note that y_1 and y_2 are the upstream and downstream depths of flow, respectively (Figures 2.1-2.3); V_1 is the upstream flow velocity (Figure 2.1); x_1 is the horizontal distance between the sluice and the toe of the hydraulic jump in question, and x is the horizontal distance measured from the sluice gate (Figure 2.3). Murzyn *et al.* (2005) selected four to five measurement locations along the length of the hydraulic jump, given in terms of $(x - x_1)/y_1$.

Table 2.1 Experimental conditions and measurement locations of Murzyn *et al.* (2005).

Experiment	y_1	y_2	V_1	Fr_1	Re_1	x_1	$(x - x_1)/y_1$
	(m)	(m)	(m/s)	-	-	(m)	-
1	0.059	0.138	1.50	2.0	88500	0.36	0.85, 1.70, 2.54, 4.24
2	0.046	0.137	1.64	2.4	75440	0.28	2.17, 4.35, 6.52, 8.70, 10.90
3	0.032	0.150	2.05	3.7	65600	0.34	4.69, 7.81, 15.60, 20.30, 25.00
4	0.021	0.133	2.19	4.8	45990	0.36	7.14, 11.90, 23.80, 31.00, 38.10

Several studies (Resch and Leutheusser 1972; Chanson 1995a,b) reported that distributions of air concentration C (or equivalently air volume fraction) exhibit a peak in the turbulent shear region, as illustrated in Figure 2.4. Chanson (1995a, 1996) related C to a solution of the diffusion equation, which is given by:

$$C = C_{max} \exp\left[- \frac{V_1 y_1 \left(y / y_1 - Y_{C_{max}} / y_1 \right)^2}{4 D_t \left(x - x_1 \right) / y_1} \right] \qquad \text{for} \qquad y < Y_{shear} \qquad (2.13)$$

where C_{max} is the maximum air content in the turbulent shear layer region measured at a distance Y_{Cmax} from the bottom; V_1 is the free-stream velocity of the inflow; D_t is a turbulent diffusivity; Y_{shear} is the upper limit of the turbulent shear region.

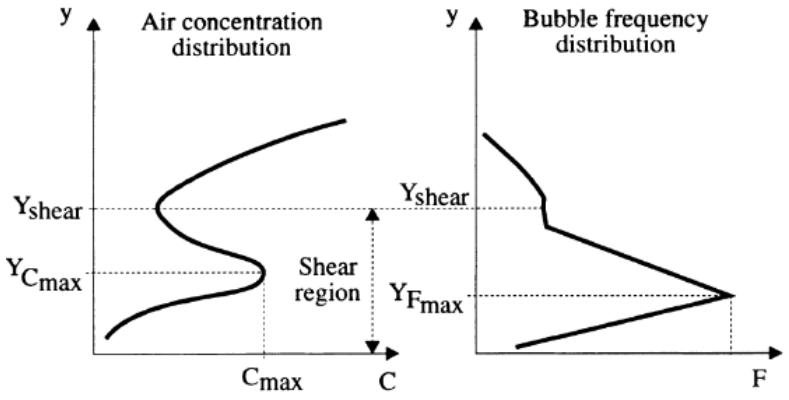

Figure 2.4 Vertical distributions of air concentration (air volume fraction) and bubble frequency in hydraulic jump rollers (from Chanson and Brattberg 2000).

Chanson (2006) experimentally investigated the entrainment of air bubbles in the developing region of a hydraulic jump under partially developed inflow conditions. The experiments were conducted in two flumes of similar geometry but different widths: One was narrow, and the other was wide. The idea was to assess the effects of channel width (scale) on air entrainment. The experimental conditions are given in Table 2.2. An example of results is shown in Figure 2.5, where F is air-bubble count rate (Hz) or bubble frequency (defined as the number of detected air bubbles per unit time). There is a good agreement between the theory (Equation 2.13; Figure 2.5, the solid curve) and experimental data (Figure 2.5, the solid squares) of Chanson (2006).

Table 2.2 Conditions of Chanson's (2006) experiments.

Flume width B	y_1	V_1	Fr_1	Re_1	x_1	Remark
(m)	(m)	(m/s)	-	-	(m)	
0.25	0.0133	1.86	5.1	24738	0.5	Narrow channel
0.25	0.0129	3.00	8.4	38700	0.5	
0.25	0.0290	2.67	5.0	77430	1.0	
0.25	0.0245	3.90	7.9	95550	1.0	
0.50	0.0265	2.60	5.1	68900	1.0	Wide channel
0.50	0.0238	4.14	8.6	98532	1.0	

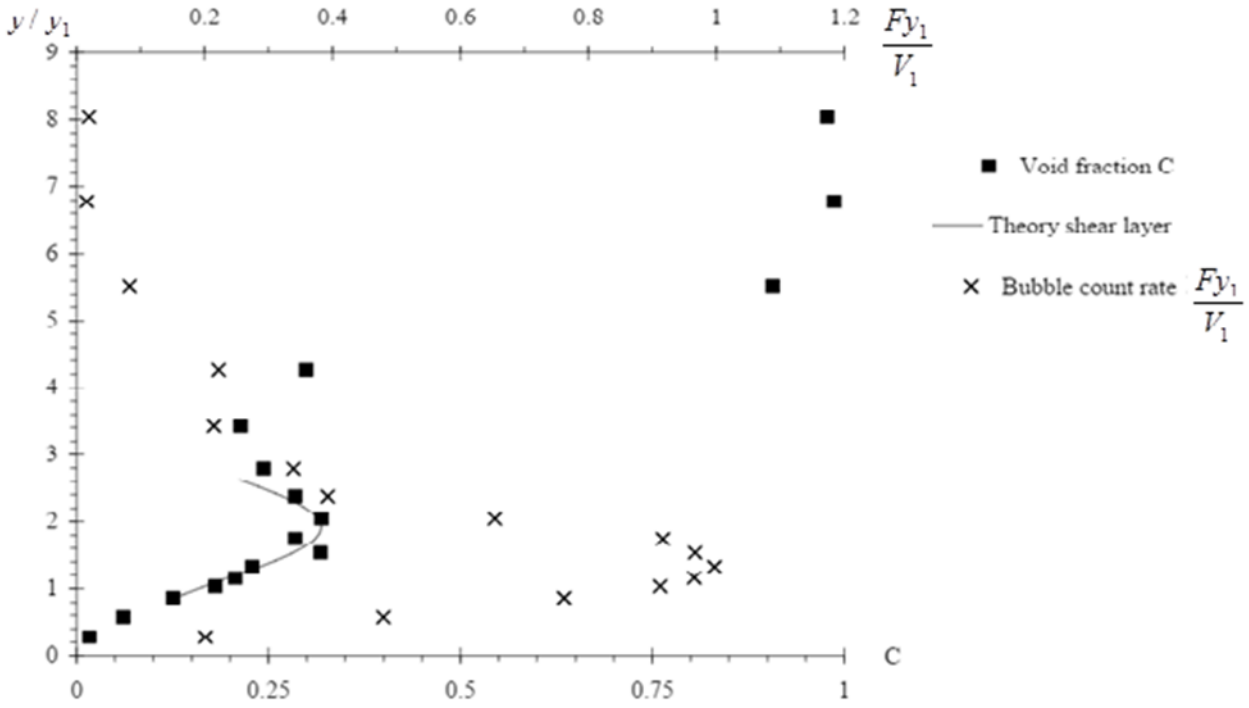

Figure 2.5 Distributions of air volume fraction and bubble count rate, measured at 0.3 m downstream of the jump toe by Chanson (2006). The upstream Froude number was $Fr_1 = 8.6$. The channel was 0.5 m wide (adopted from Chanson 2006).

Using Chanson's (2006) narrow channel (Table 2.2), Gualtieri and Chanson (2007) carried out a further experimental study of the vertical distribution of air volume fraction and bubble count rate in hydraulic jumps. The experiments produced results for the upstream Froude number in the range of $Fr_1 = 5.2$ to 14.3. In Figure 2.6, as an example, the vertical distribution of air volume fraction at $(x - x_1)/y_1 = 11.63$ is plotted. A comparison of the result with those reported in Chanson (1995 a) and in Chanson and Brattherg (2000) leads to the following observations:

- There is a decrease in the maximum air content in the turbulent shear layer with increasing distance from the jump toe. The data points appear to follow closely both power law and exponential decay functions, as suggested by Chanson and Brattberg (2000) and Murzyn et al. (2005).
- There is an exponential decay in the maximum bubble frequency (Figure 2.4) with increasing distance from the impingement point.
- The decay of the maximum air content with increasing distance from the impingement point is lower at higher Fr_1.

- The decay of the maximum number of bubble impacting the probe is lower at higher Fr_1.

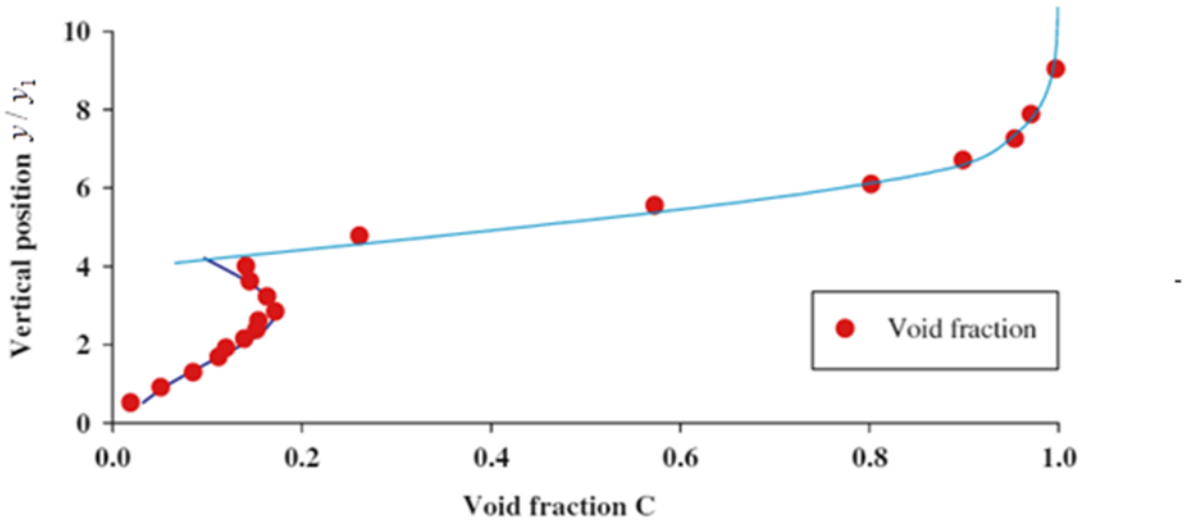

Figure 2.6 Vertical profile of air volume fraction at $(x - x_1)/y_1 = 11.63$. The experimental conditions were $Fr_1 = 8.37$, $Re_1 = 38410$, and $y_1 = 0.0129$ m (adopted from Gualtieri and Chanson 2007).

The measurements of air volume fraction in Chanson (2006) and in Chanson and Murzyn (2008) correspond to similar experimental conditions. The upstream Froude numbers were identical. The Reynolds numbers were between $Re_1 = 24738$ and 98532 (Table 2.2). A comparison of measured air-volume-fraction and bubble-count-rate distributions between the two studies reveals drastic scale effects in relatively small hydraulic jumps. In their comparative analysis, Chanson and Murzyn (2008) demonstrated quantitatively that a dynamic similarity of two-phase flows in hydraulic jumps could not be achieved with a Froude similitude. At Reynolds numbers below 10^5, the experimental data show some viscous scale effects on the rate of air entrainment and air-water interfacial area. In Figure 2.7, a comparison of air volume fraction between Chanson (2006) and Chanson and Murzyn (2008) is shown for $Fr_1 = 5.1$ and $(x - x_1)/y_1 = 8$.

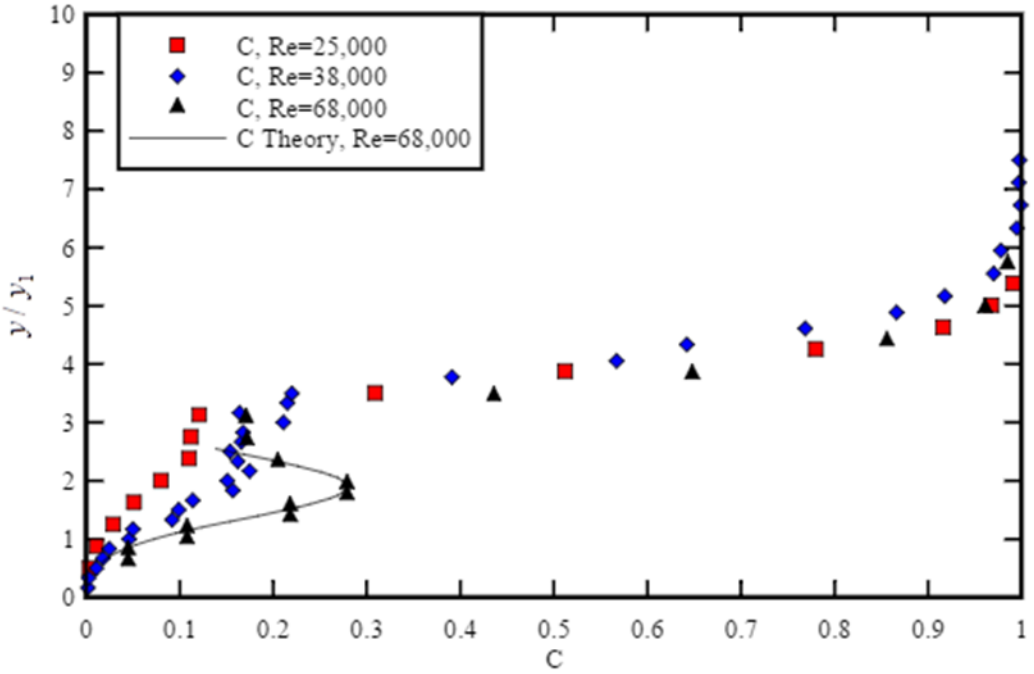

Figure 2.7 Comparison of air volume fraction in hydraulic jumps between Chanson (2006) (with Re_1 = 24738 and 68900) and Chanson and Murzyn (2008) (with Re_1 = 38576). The upstream Froude number is Fr_1 = 5.1. The distance is $(x - x_1)/y_1 = 8$ (adopted from Chanson and Murzyn 2008).

Using Chanson's (2006) wide channel (Table 2.2), Chachereau and Chanson (2010) performed experiments of hydraulic jumps with the inflow Froude number in the range of Fr_1 = 2.4 to 5.1. They investigated fluctuations in the free surface and turbulence, and air-water flow properties. They concluded that vertical profiles of air volume fraction had two characteristic regions: a shear layer region in the lower part of the flow, and an upper free-surface region above.

Chachereau and Chanson (2010) compared their results for Fr_1 = 5.1 with Chanson's (2006) results for the same value of Fr_1 but smaller values of Re_1. In this comparative analysis, the Reynolds number ranges from Re_1 = 24738 (Table 2.2) to 125400. It was shown that the Froude similitude was not satisfied in a hydraulic jump for Fr_1 = 5.1 within the range of Reynolds numbers. The data of air volume fraction obtained with Reynolds numbers below 40000 could not be scaled up to larger Reynolds numbers. The bubble count rate, turbulence properties, and bubble chord exhibited monotonic trends with increasing Reynolds numbers. The implication was that the results could not be extrapolated to large-size prototype structures without significant scale effects.

Using particle image velocimetry (PIV) and bubble image velocimetry (BIV) techniques, Lin et al. (2012) measured the flow structures and turbulence statistics of three steady hydraulic jumps. The upstream Froude number was in the range of Fr_1 = 4.51–5.35. Measurements were made from both the non-aerated and aerated regions of the hydraulic jumps, and were validated using laser Doppler velocimetry (LDV) and tracking bubble trajectories. Lin et al. (2012) also obtained measurements from a weak jump, with a Froude number of Fr_1 = 2.43, aiming to examine the differences between weak and steady hydraulic jumps. The experimental conditions of Lin et al. (2012) are listed in Table 2.3.

Table 2.3 Experimental conditions of weak and steady hydraulic jumps in Lin et al. (2012).

Experiment	y_1	y_2	V_1	Fr_1	Re_1	Remark
	(m)	(m)	(m/s)	-	-	
1	0.0192	0.0570	1.063	2.43	20410	Weak jump
2	0.0195	0.0115	1.973	4.51	38474	Steady jump
3	0.0200	0.0132	2.216	5.00	44320	
4	0.0195	0.0138	2.337	5.35	45572	

To the best of our knowledge, Wang and Chanson (2015) is the most recent experimental study of air entrainment in a hydraulic jump. Their experiments covered a wide range of Froude numbers ($3.8 < Fr_1 < 10.0$) and Reynolds numbers ($35800 < Re_1 < 164000$). The authors investigated non-intrusively fluctuations in the free surface and roller position, using a series of acoustic displacement meters. They reported the characteristic frequencies of the fluctuating motions, some major roller surface deformation patterns, air-water flow properties, air volume fraction and bubble count rate in the rollers, and interfacial velocity distributions. Wang and Chanson (2015) used Chanson's (2006) wide channel (Table 2.2). An example of vertical distributions of air volume fraction is shown in Figure 2.8.

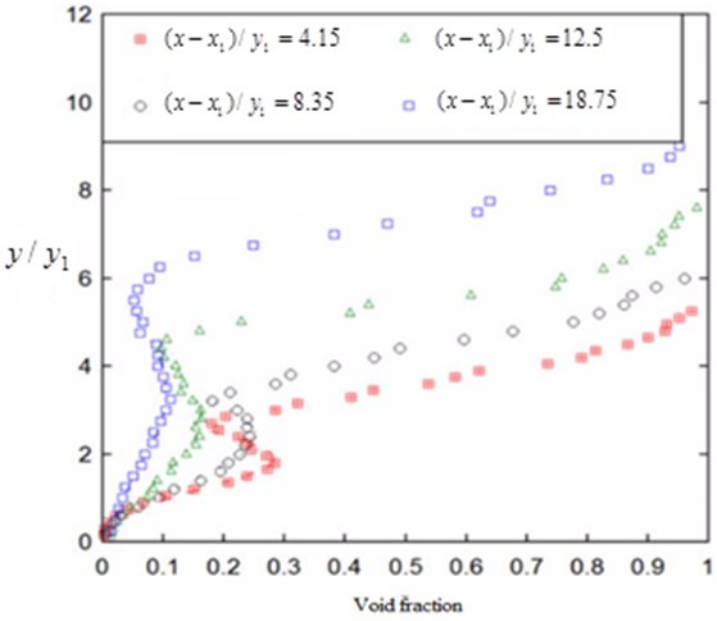

Figure 2.8 Vertical distributions of air volume fraction at a series of positions along the length of the hydraulic jump. The flow conditions were: Q = 0.0347 m^3/s, y_1 = 0.0206 m, x_1 = 0.83m, Fr_1 = 7.5, and Re_1 = 68000 (adopted from Wang and Chanson 2015).

2.6 Numerical studies of air entrainment in hydraulic jumps

A review of the literature shows a very limited number of numerical studies of hydraulic jumps as two-phase open-channel flow. This section discusses the previous numerical studies dealing with air entrainment and air volume fraction distributions in hydraulic jumps.

Ma et al. (2011) simulated hydraulic jumps using a subgrid air entrainment model in conjunction with 3D two-fluid models of bubbly flow (Reynolds-averaged equation model and Detached Eddy Simulation model). The upstream Froude number was Fr_1 = 1.98 and the Reynolds number was Re_1 = 88500. They predicted air volume fraction distributions at a number of locations downstream of the jump toe and compared the results with the measurements of Murzyn et al. (2005). In Figure 2.9, simulated and measured air volume fraction profiles are plotted as a function of the normalised vertical coordinate, where y/y_1=0 denotes the bottom of the channel.

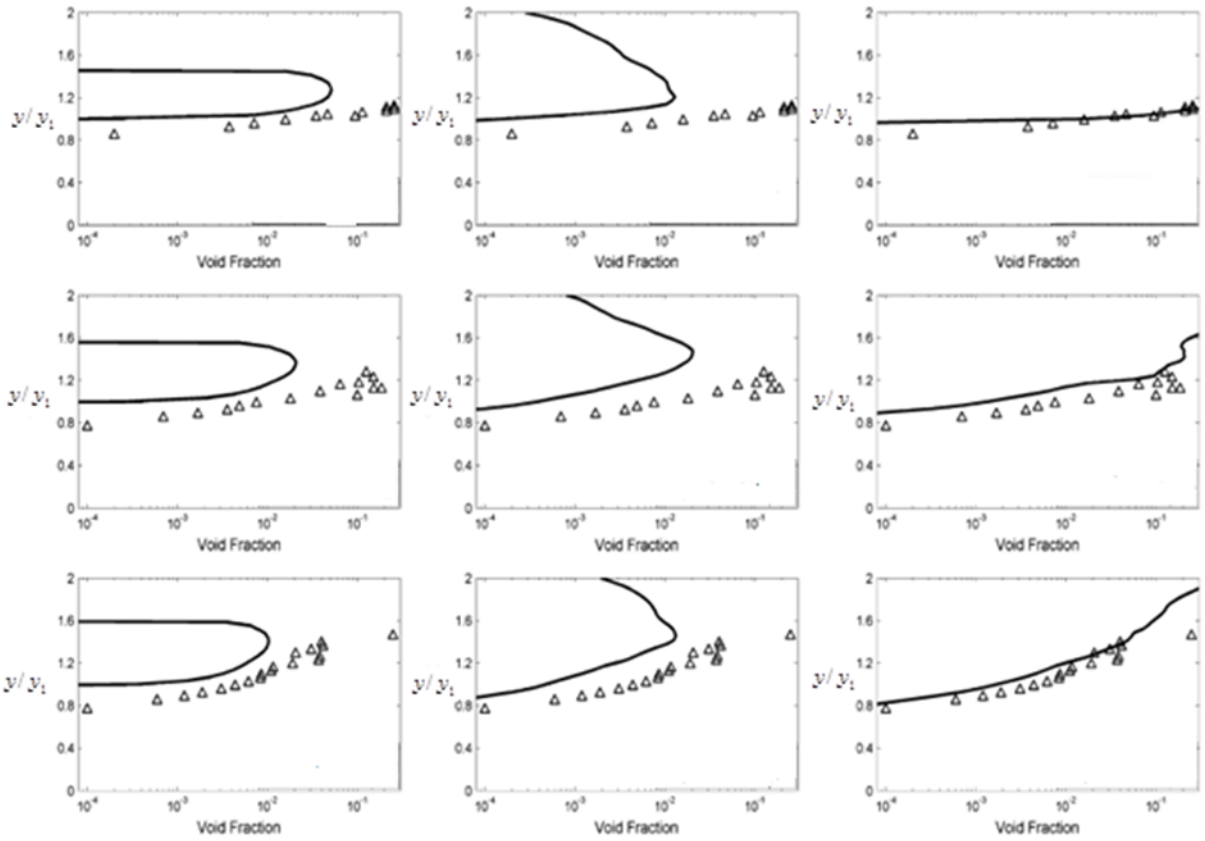

Figure 2.9 Distributions of air volume fraction predicted with the Reynolds-averaged equation model (left) and Detached Eddy Simulation model (right) at Fr_1 = 1.98 at $(x - x_1)/y_1$ = 0.85, 1.7 and 2.54 (from top to bottom), in comparison with the measurements of Murzyn et al. (2005). The middle column presents DES results accounting for contributions from bubbles, while excluding those from the wavy interface (adopted from Ma et al. 2011).

Regarding the Reynolds-averaged equation model, Ma et al. (2011) noted that the lower half of the air volume fraction profiles, corresponding to the shear layer region, matched the experimental data quite well, but the upper half of the profiles, correspond to the roller region (Figure 2.1), did not. They suggested that the Detached Eddy Simulation results matched the measurements well both in the lower shear layer and in the upper roller region (Figure 2.9).

Recently, Xiang et al. (2014) presented an Eulerian multi-fluid model for investigating flow structures of hydraulic jumps. They obtained explicit solutions to the phasic distribution of fluids through interfacial momentum transfer models. Air ingestion at the jump toe was handled by a sub-grid air entrainment model. The location of the free surface was captured using a compressive

VOF model. Xiang et al. (2014) considered mechanistic coalescence and breakage kernels in the calculations. Their idea was to better represent the evolution of air bubble size in the subcritical flow region. The control parameters of their model simulations are listed in Table 2.4. Xiang et al. (2014) compared their numerical results to experimental data in Chachereau and Chanson (2010) and Lin et al. (2012).

Table 2.4 Physical parameters of three selected flow cases in Xiang et al. (2014).

Case	Fr_1	y_1	y_2	Q	Re_1	Remark
	-	(m)	(m)	(m^3/s)	-	
1	3.1	0.0440	0.174	0.0446	89000	Chachereau and Chanson's (2010) experiment
2	5.1	0.0395	0.254	0.0627	130000	
3	4.5	0.0195	0.115	0.0192	38400	Lin et al.'s (2012) experiment

Xiang et al. (2014) assumed two-dimensional steady state flows in all simulations. Their computational domain consisted of 28,000 non-uniform cells (Figure 2.10). The simulations used ANSYS CFX12. Air entrainment and complete merging model were implemented using CFX Expression Language (CEL). The associated source term for the multiple-size-group model was incorporated into the simulations. CEL allows users to define inputs as variables, capture outputs as variables, and perform operations on those variables.

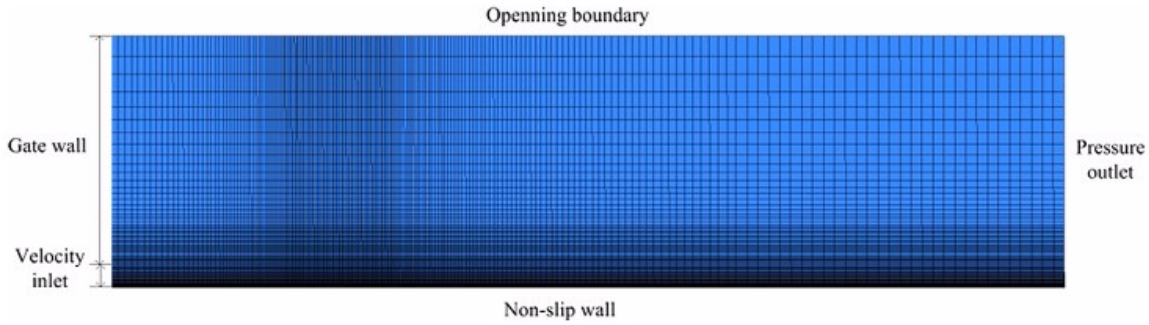

Figure 2.10 Model domain, mesh and boundary conditions in Xiang et al. (2014).

Xiang et al. (2014) predicted distributions of water superficial velocity vectors for Case 3 (Figure 2.11), air volume fractions in hydraulic jump rollers for Cases 1 and 2 (Figure 2.12), and air volume fractions at 3 different locations downstream of the jump toe for Case 1 (Figure 2.13).

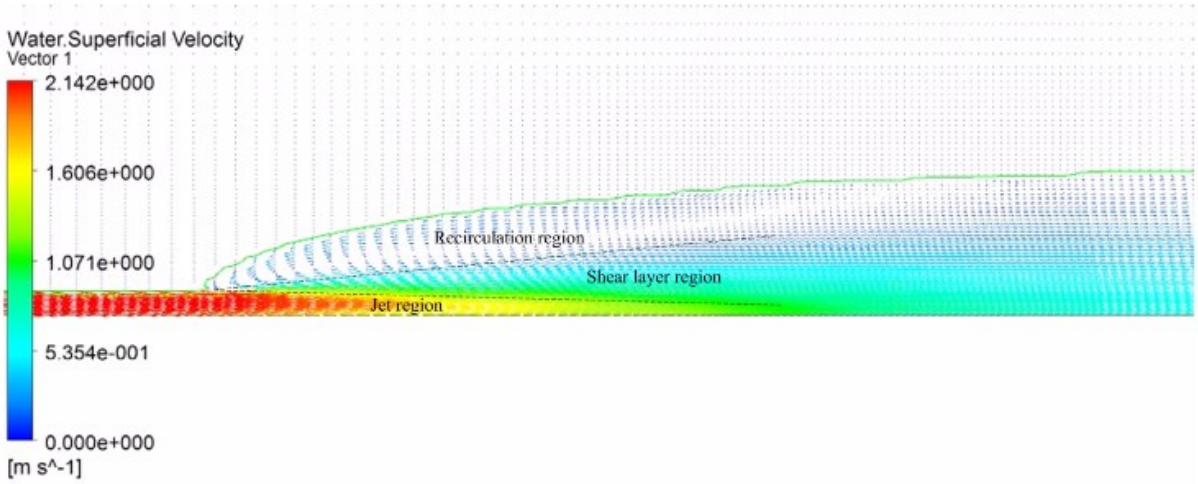

Figure 2.11 Predicted water velocity vectors for Case 3 (Table 2.4) in Xiang et al. (2014).

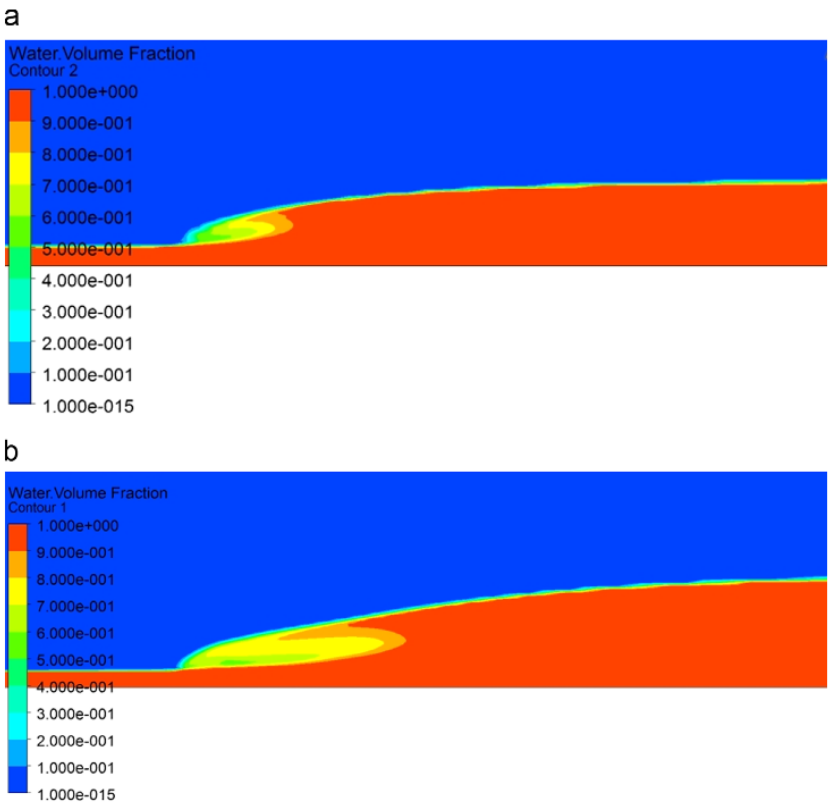

Figure 2.12 Contours of water and air volume fraction for: (a) Case 1, and (b) Case 2 in Xiang et al. (2014).

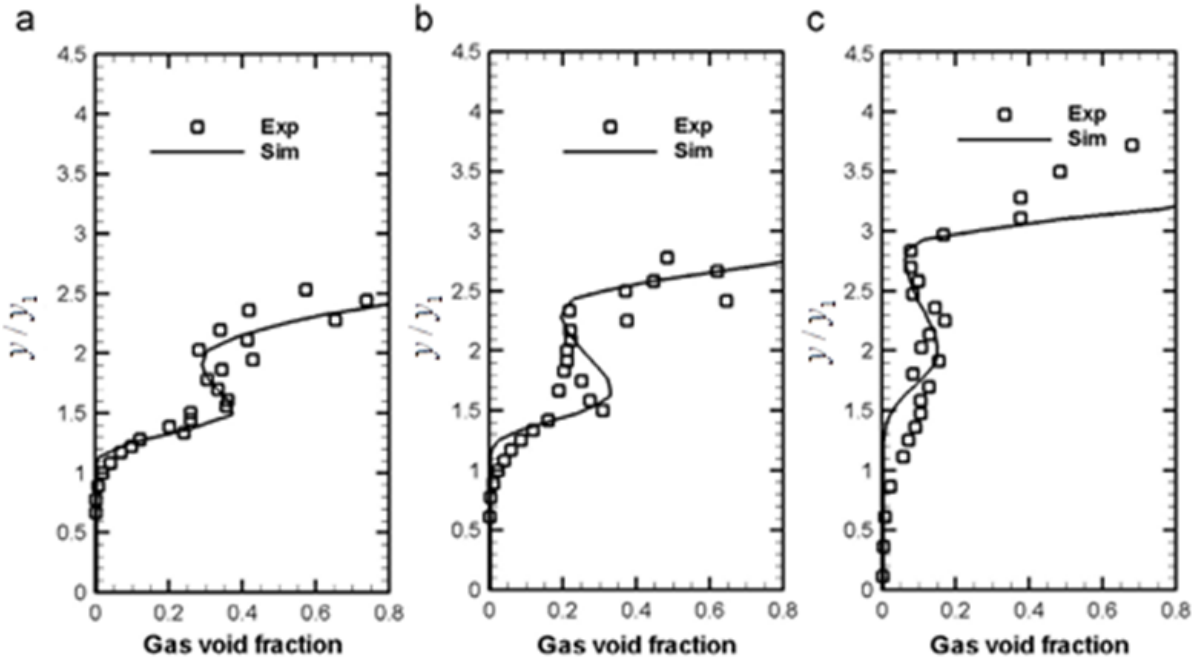

Figure 2.13 Distributions of air volume fraction for Case 1 at axial sections $(x - x_1)/y_1 = 0.91$ m (panel a), 1.7 (panel b), and 3.41 (panel c). Note that *y* is the vertical position (adopted from Xiang et al. 2014).

Witt et al. (2015) numerically simulated air–water flow characteristics in hydraulic jumps in an open channel, using setup corresponding to the laboratory experiments of Murzyn et al. (2005), which was discussed in the previous section. Witt et al.'s (2015) simulations used OpenFOAM (Jasak 2009), and produced unsteady flow field in two and three dimensions. They solved the evolving free surface using InterFoam (a VOF solver), and located the free surface using air volume fraction of 0.5 as a threshold. Witt et al. (2015) obtained time average results. In this connection, a comparison of relative errors between sampling times of 1, 5, 10, 15 and 20 seconds shows that a sampling time of 15 seconds gave the lowest relative error. Witt et al. (2015) reported distributions of time averaged volume fraction (Figure 2.14) and vertical profiles of average air volume fraction (Figure 2.15), with a comparison to the experimental data of Murzyn et al. (2005).

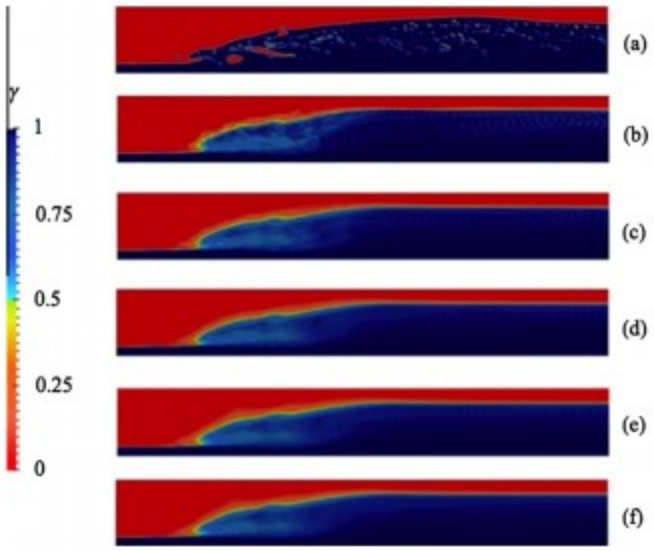

Figure 2.14 Distributions of predicted volume fraction for a 2-D simulation with the upstream Froude number Fr_1 = 4.82. Panel (a) shows an instantaneous distribution. Panels (b), (c), (d), (e), and (f) show the time-averaged distributions over the durations of 1, 5, 10, 15, and 20 s, respectively (adopted from Witt et al. 2015).

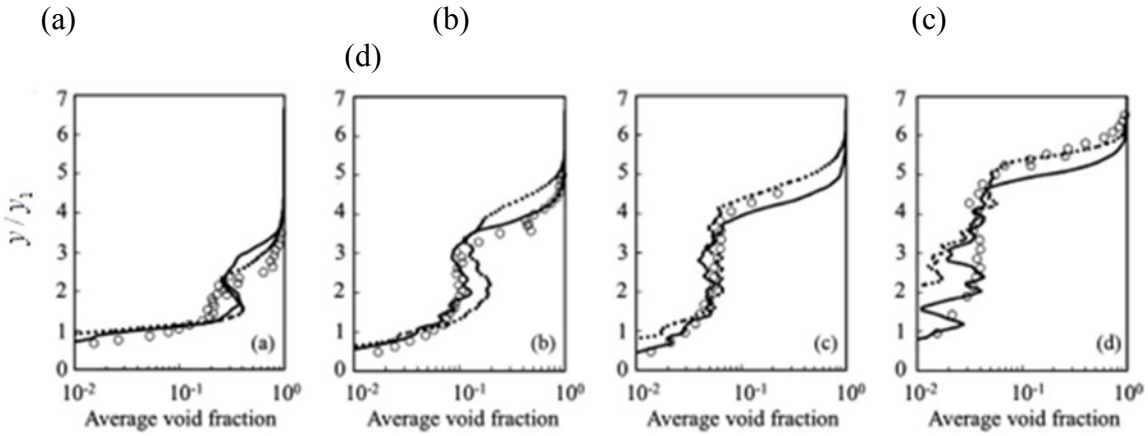

Figure 2.15 Vertical profiles of time-averaged air volume fraction for Fr_1 = 4.82 at four positions along the length of the hydraulic jump: (a) x = 7.14 y_1 y_1; (b) x = 11.9 y_1; (c) x = 16.67 y_1; and x = 23.8 y_1. The open circle symbols are Murzyn et al.'s (2005) measurements of average void fraction. The dotted and solid curves are Witt et al.'s (2015) 2- and 3-D predictions, respectively (adopted from Witt et al. 2015).

.

2.7 Summary

Ideally, laboratory and computer modelling of hydraulic jumps should keep the same values of the Reynolds number, the Froude number, and Weber number as the prototype. In most of cases, laboratory modelling studies satisfied geometrical similarity, but not simultaneously Froude number, Reynolds number and Weber number similarities. With the same fluids (air and water) in model and prototype, the process of air entrainment is adversely affected by significant scale effects in small size models (Chanson 2006).

The use of small length scales is a common limitation of previous experimental and numerical studies of air entrainment in hydraulic jumps. There is a need for further studies using relatively large and more practical dimensions so as to satisfy the Froude number, Reynolds number and Weber number similarities at the same time.

Previous studies have been limited to hydraulic jumps of small dimensions. The behaviour may not reflect truly the behaviour of hydraulic jumps in real-world open channels and water conveyance systems. The largest upstream Reynolds number (Equation 2.11) was perhaps 125400 reported in Xiang et al. (2014) who simulated hydraulic jumps and 164000 reported in Wang and Chanson (2015) who made laboratory measurements. Xiang *et al.*'s (2014) simulations were limited to steady state flow conditions, as opposed to transient conditions.

In summary, the previous studies of hydraulic jumps have rarely reached flow conditions with upstream Reynolds numbers exceeding 10^6. A knowledge gap exists with regard to distributions of air entrainment in hydraulic jumps of large and practical dimensions. This corresponds to large Reynolds numbers. The need for simulations of hydraulic jumps under conditions of transient motions and large Reynolds numbers have motivated this research work.

Chapter 3 Modelling Methodology

The aim of this study is to simulate four different hydraulic jumps in an open channel with four different upstream Froude numbers under transient condition and to predict air entrainment in these hydraulic jumps. The results will be compared with those of Chachereau and Chanson (2010) who used a physical model to study air entrainment in four different hydraulic jumps at (smaller dimensions and smaller Reynolds numbers). These computational simulations use ANSYS 17.1 (Fluent). In this chapter, a description of the simulation domain will be presented. The governing model equations used for the simulations, boundary conditions and initial conditions will be presented.

3.1 Model domain and geometry

In this section, the geometry and general shape of the model domain used in all the simulations in this study will be presented. The model domain consists of a channel with a length of 6 m and a height of 2.2 m. The channel is horizontal and has two inlets and one outlet: one water inlet, one air inlet at the top, and one outlet to allow water and air to leave the domain during the simulations. All the simulations are two dimensional (Figure 3.1).

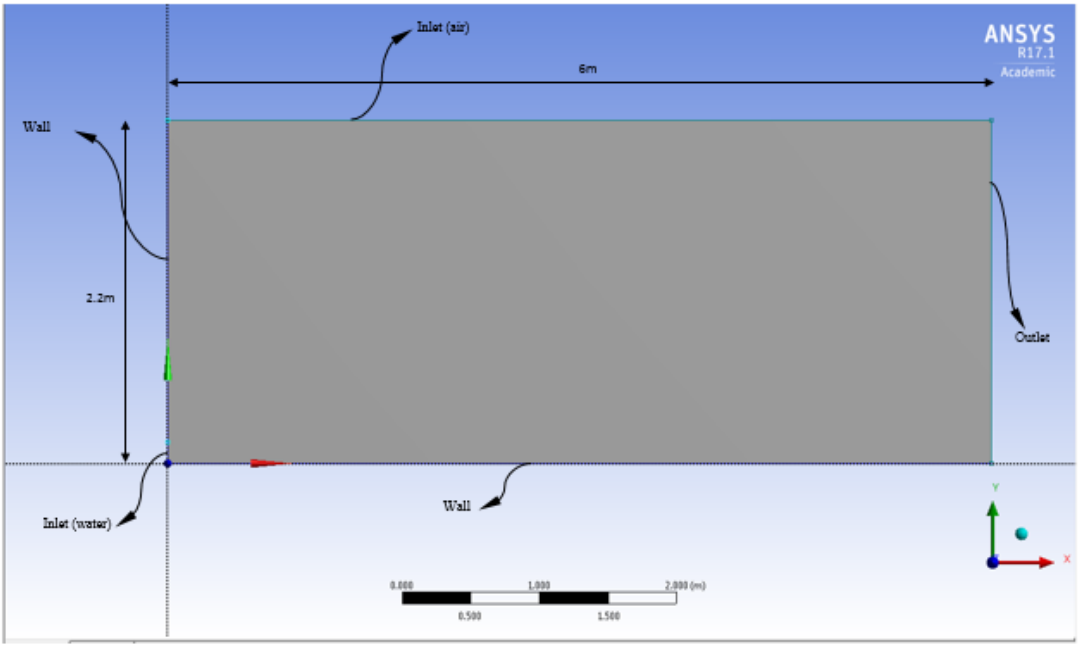

Figure 3.1 Dimensions of the computational model domain.

3.2 Volume of fluid (VOF) model theory

The VOF model (Hirt and Nichols 1981) can model two or more fluids which are not mixable by solving momentum equation, energy equation and tracking the volume fraction of each fluid throughout the domain. Modelling of open channel flow is a typical application of this method.

3.2.1 Steady – state and transient VOF calculations

The model in ANSYS Fluent is generally used to compute a time-dependent or transient solution, but in some cases that involve steady state flow, it is possible to perform steady-state calculations.

The VOF model relies on the fact that two or more fluids (or phases) are not interpenetrating. For each phase in the calculations, a variable is introduced to represent the volume fraction of the phase in each computational cell. The sum of all volume fractions of all phases is one in each computational cell. The fields for all variables and properties are shared by the phases. In other words, all the fluid properties are represented in form of volume-averaged values, as long as the volume fraction of each of the phases is known at each location. Thus, the variables and properties in any cell in computational domain are either completely representative of one of the phases, or representative of a mixture of the two phases (air and water in this study) or more, depending upon the volume fraction values. In other words, if the q^{th} fluid's volume fraction in the cell is denoted as α_q, then the following three conditions are possible:

(a) $\alpha_q = 0$: The cell is empty of the q^{th} fluid

(b) $\alpha_q = 1$: The cell is full of the q^{th} fluid

(c) $0 < \alpha_q < 1$: a certain fraction of cell (α_q) is filled with q^{th} fluid.

Based on the local value of α_q, the appropriate properties and variables will be assigned to each control volume within the domain (Hirt and Nichols 1981) (Fluent 2013).

3.2.2 Volume fraction equation

The tracking of the interface(s) between the phases is accomplished by solving the continuity equation for the volume fraction of one (or more) of the phases. For the q^{th} phase (air in this study), this equation has the following form (Walters and Wolgemuth 2009) (Fluent 2013):

$$\frac{1}{\rho_q}\left[\frac{\partial}{\partial t}(\alpha_q \rho_q) + \nabla.(\alpha_q \rho_q \vec{v}_q) = s_{\alpha_q} + \sum_{p=1}^{n}(\dot{m}_{pq} - \dot{m}_{qp})\right] \tag{3.1}$$

where $\dot{m}_{qp}$ is the mass transfer from phase q (air) to p (water) and $\dot{m}_{pq}$ is the mass transfer from phase p (water) to phase q (air). The s_{α_q} is the source term and is the mass of phase q which is added to the continuous phase (if there is any) from the dispersed other phases (for example, due to vaporization of liquid phase) and any user defined sources. This source term is zero by default. ρ_q is the density of the q^{th} phase. In this study, there are only two phases in all the simulations and it can be assumed that there will not be any mass transfer between the phases during the simulations. In other words, the right hand side of the equation (3.1) is equal to zero for the simulations of this study.

The volume fraction equation will not be solved in the model for the primary phase (water in this study). The primary phase volume fraction will be computed based on the following equation:

$$\alpha_{air} + \alpha_{water} = 1 \tag{3.2}$$

There are two methods to solve volume fraction equation (equation 3.1): the implicit method and the explicit method. These methods will be discussed in Sections 3.4.1 and 3.4.2.

3.2.2.1 The implicit scheme

When the implicit scheme is used for time discretization, ANSYS Fluent's standard finite-difference interpolation schemes are used to obtain the face fluxes for all cells, including those near the interface. More information about these interpolation schemes are in Fluent (2013).

$$\frac{\alpha_q^{n+1}\rho_q^{n+1} - \alpha_q^n \rho_q^n}{\Delta t} Vol + \sum_f (\rho_q^{n+1} U_f^{n+1} \alpha_{q,f}^{n+1}) = \left[s_{\alpha_q} + \sum_{p=1}^{n} (\dot{m}_{pq} - \dot{m}_{qp}) \right] Vol \tag{3.3}$$

Fluent (2013) states "Since this equation requires the volume fraction values at the current time step (rather than at the previous step, as for the explicit scheme), a standard scalar transport equation is solved iteratively for each of the secondary-phase volume fractions at each time step".

In the current study, the implicit scheme was used in the simulations.

3.2.2.2 The explicit scheme

"In the explicit approach, ANSYS Fluent's standard finite-difference interpolation schemes are applied to the volume fraction values that were computed at the previous time step.

$$\frac{\alpha_q^{n+1}\rho_q^{n+1}-\alpha_q^n\rho_q^n}{\Delta t}Vol+\sum_f(\rho_q^n U_f^n\alpha_{q,f}^n)=\left[s_{\alpha_q}+\sum_{p=1}^{n}(\dot{m}_{pq}-\dot{m}_{qp})\right]Vol \tag{3.4}$$

where $n+1$ is the index for new (current) time step; n is the index for previous time step; $\alpha_{q,f}$ is face value of the q[th] phase volume fraction; Vol is volume of the cell; U_f is the volume flux through the face, based on normal velocity.

This formulation does not require iterative solution of the transport equation during each time step, as is needed for the implicit scheme" (Fluent 2013).

3.2.3 Material properties

The properties appearing in the volume of fluid transport equations are determined by the presence of the component phases in each computational cell of the domain. For example, in a two-phase system, if subscripts a and b represent phase a (water) and phase b (air) respectively, and if the volume fraction of the second phase is being tracked, the density in each cell is given by:

$$\rho=\alpha_b\rho_b+(1-\alpha_b)\rho_a \tag{3.5}$$

In general, for an n phase system, the volume-fraction-averaged density is:

$$\rho=\sum_{q=1}^{n}\alpha_q\rho_q \tag{3.6}$$

All other fluid properties (for example, viscosity) are computed in the same manner.

3.3 Reynolds averaged Continuity and Momentum equation

Continuity and momentum equations will be solved throughout the domain, and the resulting velocity field is shared among the phases. The properties ρ and μ in the momentum equation, is volume-fraction-averaged of all phases (Wilcox 2006):

$$\frac{\partial V_i}{\partial x_i}=0 \tag{3.7}$$

$$\rho\frac{\partial V_i}{\partial t}+\rho V_j\frac{\partial V_i}{\partial x_j}=-\frac{\partial p}{\partial x_i}+\frac{\partial}{\partial x_j}(2\mu S_{ji}-\rho\overline{u'_j u'}_i) \tag{3.8}$$

In equations (3.8) $-\overline{u'_j u'}_i$ is the specific Reynolds stress tensor and is shown by

$$\tau_{ij} = -\overline{u_i' u_j'} \tag{3.9}$$

also we have

$$\tau_{ij} = 2\nu_T S_{ij} - \frac{2}{3} k \delta_{ij} \tag{3.10}$$

3.4 Energy equation

The energy equation shown below is also shared among the phases (Fluent 2013):

$$\frac{\partial}{\partial t}(\rho e) + \nabla.(\vec{v}(\rho e + p)) = \nabla.(k_{eff} \nabla T) \tag{3.11}$$

The volume of fluid model considers energy, e and temperature, T , as mass-averaged variables:

$$e = \frac{\sum_{q=1}^{n} \alpha_q \rho_q e_q}{\sum_{q=1}^{n} \alpha_q \rho_q} \tag{3.12}$$

The properties ρ and k_{eff} (effective thermal conductivity) are also shared between the existing phases.

In this study, the energy equation was not used in the computation.

3.5 Surface tension

Surface tension is the result of attractive forces between molecules in a fluid. For example, in an air bubble surrounding with water, inside the bubble, far from the surface, the net force on an air molecule due to its neighbouring molecules is zero. At the interface, however, the net force on the surface air molecules is radially inward. This radially inward force makes the entire spherical surface contract. As a result, the pressure on the concave side of the surface will increase. The surface tension is a force, acting only at the surface in order to maintain equilibrium in such instances. It acts to balance the radially inward intermolecular attractive force with the radially outward pressure gradient force across the surface (Chanson 1996).

In this research work, the volume of fluid (VOF) model for tracking of the free surface, considers the effects of surface tension at the air-water interface on mixture motion, when air and water are present in a cell. The consideration involves a volume force, which is formulated based on a continuum method. Details about this method have been described in Brackbill et al. (1992). We set the surface tension coefficient at the interface of air and water phases in all the simulations to a constant value equal to σ = 0.072 N/m [Equation (2.12)].

3.6 Standard *k*-ε turbulent model

In this study, the standard k-ε method was used for modelling the turbulent flow in all simulations.

Standard k-ε method is one kind of the two-equation turbulence models. Two-equation turbulence models not only determines the transport equation for the turbulence kinetic energy (k) but also determine turbulent length and time scale.

In the standard k-ε method, the transport equation for kinetic energy has been derived from the exact mathematical equation. The transport equation for kinetic energy dissipation rate, ε, has however been derived using physical reasoning rather than the exact mathematical equation (Launder and Spalding 1974).

3.6.1 Transport equations for the standard *k*-ε model

The turbulence kinetic energy, k and its dissipation rate, ε, are obtained from the following transport equations (Launder and Sharma 1974) (Wilcox 2006): Turbulence Kinetic Energy is governed by:

$$\frac{\partial k}{\partial t} + V_j \frac{\partial k}{\partial x_j} = \tau_{ij} \frac{\partial V_i}{\partial x_j} - \varepsilon + \frac{\partial}{\partial x_j}\left[(\nu + \nu_T / \sigma_k) \frac{\partial k}{\partial x_j} \right] \tag{3.13}$$

Dissipation Rate is governed by:

$$\frac{\partial \varepsilon}{\partial t} + V_j \frac{\partial \varepsilon}{\partial x_j} = C_{\varepsilon 1} \frac{\varepsilon}{k} \tau_{ij} \frac{\partial V_i}{\partial x_i} - C_{\varepsilon 2} \frac{\varepsilon^2}{k} + \frac{\partial}{\partial x_j}\left[(\nu + \nu_T / \sigma_\varepsilon) \frac{\partial \varepsilon}{\partial x_j} \right] \tag{3.14}$$

$\overline{u_i' u_j'}$ in this equation is the temporal average of the fluctuating velocities. ν_T is the kinematic eddy viscosity and,

$$\nu_T = C_\mu k^2 / \varepsilon \tag{3.15}$$

where k is the kinetic energy of turbulent fluctuations per unit mass, ε is the dissipation per unit mass, U is the mean velocity component and the other constants are as follows (Wilcox 2006):

$C_{\varepsilon 1}$=1.44, $C_{\varepsilon 2}$=1.92, C_μ=0.09, σ_k=0.72, σ_ε=1.3

3.7 Finite volume mesh

The ANSYS fluent software needs a finite volume mesh throughout the computational domain for calculations. It is necessary to consider two important points about creating the mesh in computational domain. First, the created mesh should be fine enough to let the model calculate the rapid spatial variations of velocity or, depending on the case, other important flow characteristics like temperature. This is important especially near the walls or solid structures in flow path and where the flow condition is turbulent and the probability of having large changes of flow characteristics in small distances is high. This study focuses on simulating the hydraulic jump phenomenon, and due to the turbulent nature of hydraulic jump, the mesh must be chosen to be fine enough in order to have precise and reliable simulation results.

Second, although a fine mesh is required to have reliable calculations and results, the number of cells should not be excessively large. A very large number of cells in a simulation will result in higher and sometimes unnecessary computational costs and time. Also, it must be noted that the larger the number of cells, the more difficult the post processing of the results.

In this study, test simulations of hydraulic jumps were used to check the suitability of mesh sizes. It is important to achieve high computational accuracy. Accordingly, the iteration residuals were set to 10^{-6}. The use of coarse mesh will result in divergence of the calculations and the model will not be able to continue stable computation. In this study, we started the simulations using a large mesh size (equal to 1 cm), which resulted in divergent calculations. Subsequently, we reduced the mesh size gradually, and finally determine the optimum cell size. At the end the proper mesh size for this research was chosen through these test simulations and was used in all the simulations. Since the hydraulic jump phenomenon is associated with strong turbulence, a relatively fine mesh had to be chosen in order to have precise and stable calculations. Also, since the length and location of the jump change and the hydraulic jump have frequent fluctuations back and forth, a uniform mesh size was chosen for the entire domain. As a result, it was not necessary to refine the mesh size near the walls.

The computational domain in all the simulations of this study, (Figure 3.2), consists of 2131200 cells. The mesh structure is nearly uniform all over the domain and the cells have 2.5×2.5 mm square shapes.

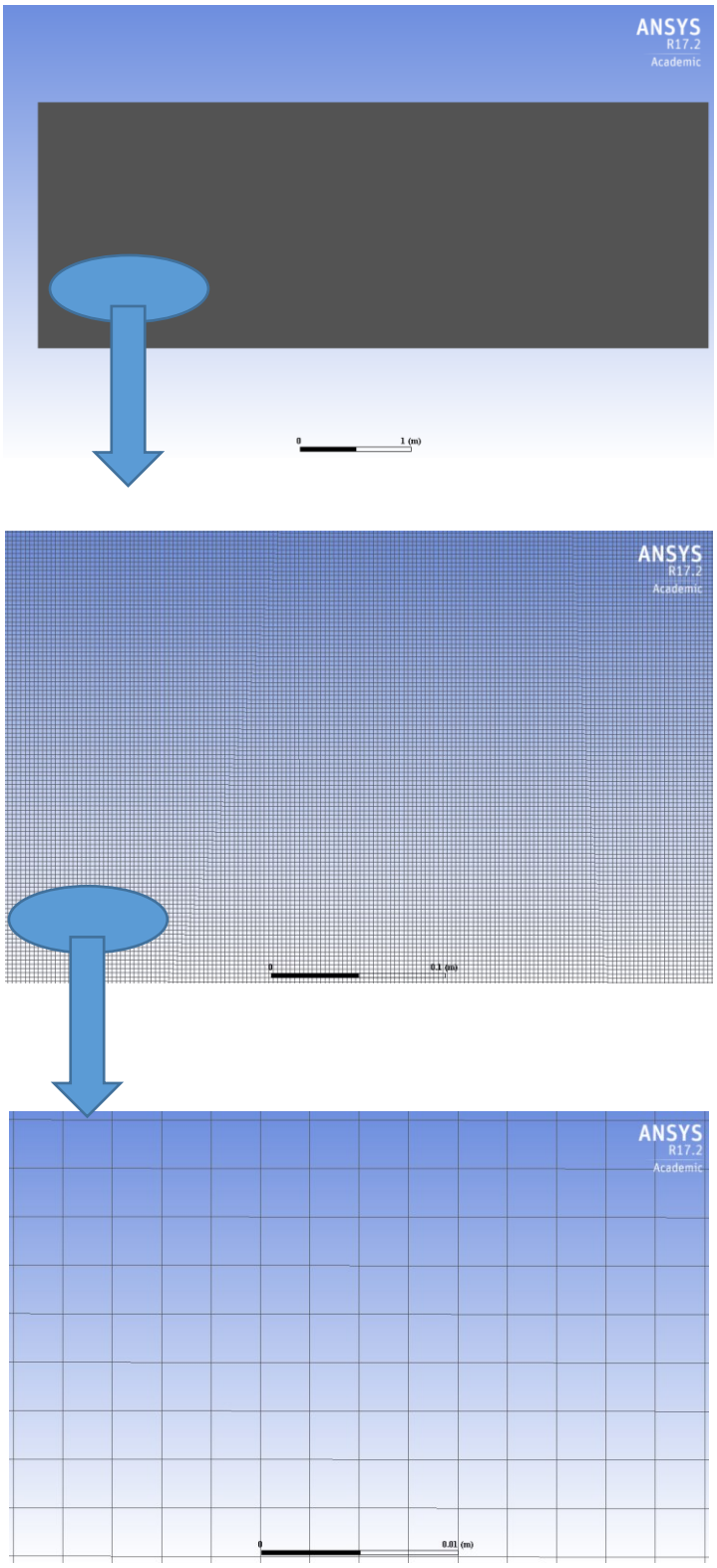

Figure 3.2 The finite volume mesh of the computational domain.

3.8 Boundary conditions

This section introduces the boundary condition types used in the simulations. Also, the key points for setting up the model in order to simulate the desired hydraulic jump are discussed.

One of the challenging issues that was encountered during this research was choosing the best boundary condition to have a well-balanced hydraulic jump which stays in its place without moving gradually toward up stream or downstream of the domain. Even in physical simulations, balancing the forces at upstream and downstream of the hydraulic jump is a relatively delicate and time consuming procedure. Furthermore, in physical simulations, usually a tail gate is used to maintain subcritical condition downstream of the hydraulic jump and by adjusting the tailgate height in a trial and error manner, a balanced hydraulic jump can eventually be created. In mathematical simulation, adjusting a tail gate in real time while the simulation is running is not possible. As a result, choosing a proper setting for the downstream boundary condition was critical in order to maintain the desired subcritical downstream depth and create a stationary hydraulic jump.

Also, in order to choose a suitable boundary condition for the upper boundary of the domain (which is actually the atmosphere), three different types of boundary conditions: wall, pressure outlet, and pressure inlet, were verified and the pressure inlet showed the best compatibility with the simulation condition and setting.

3.8.1 Pressure inlet

Pressure inlet boundary conditions are used when the pressure and other scalar properties of the flow where it enters the domain are known. In this type of boundary, the user should define the total gauge pressure:

$$p_0 = p_s + \frac{1}{2}\rho v^2 \tag{3.16}$$

where p_0 is the total gauge pressure, p_s is the hydrostatic pressure with respect to the operating pressure, which is defined in the "Operating condition" part of the model, and v is the fluid velocity at the inlet.

In Figure 3.1, the upper boundary of the domain is pressure inlet. Since the upper boundary represents the atmosphere in an open channel, the pressure can be defined and it is equal to atmospheric pressure ($p_s = 0$). We can assume that the air velocity is zero at the upper boundary

of the domain ($v = 0$). As a result, the total pressure or p_0 at the upper boundary of the domain, which is pressure inlet, is zero in all the simulations.

3.8.2 Wall

The wall boundary condition is used for regions that we want to bound the fluid and the solid surfaces. When there is wall boundary condition in the simulation, the model will use a certain type of wall treatment in the computations for the neighbouring cells. A wall treatment is the set of near-wall modelling assumptions for each turbulence model. Three types of wall treatment are provided in Fluent, each of which follows certain wall functions to solve the flow condition inside the cells adjacent to the wall boundary. Wall functions are used to bridge the viscosity-affected region between the wall and the fully-turbulent region.

This study used "Standard wall function" as the near wall treatment. In the standard wall function, the user has the possibility to set any desired value for the shear stress and to choose if the wall should have roughness. In all the simulations in this study, the "No slip" type of wall function has been used. The "Standard wall function" with "No slip" type of wall boundary condition is based on the work of Launder and Spalding (1974). The law-of-the-wall for mean velocity yields:

$$U^* = \frac{1}{\kappa} \ln(E^* y^*) \tag{3.17}$$

where U^* is the dimensionless velocity and y^* is the dimensionless distance from the wall:

$$U^* = \frac{U_{ac} C_{\mu w}^{1/4} k_{ac}^{1/2}}{\tau_w / \rho} \tag{3.18}$$

and

$$y^* = \frac{\rho C_{\mu w}^{1/4} k_{ac}^{1/2} y_{ac}}{\mu} \tag{3.19}$$

where

$$\tau_w = \frac{\mu U_{ac}}{\bar{y}_{ac}} \tag{3.20}$$

and κ is von Kármán constant equal to 0.4187, E^* is an empirical constant equal to 9.793, U_{ac} is the mean velocity of fluid at the wall adjacent cell centroid, k_{ac} is the turbulent kinetic energy at

the wall adjacent cell centroid, y_{ac} is the distance from the centroid of the wall, adjacent cell to the wall, $\overline{y}_{ac}$ is the mean of y_{ac} s of all the cells adjacent to the wall, and μ is the dynamic viscosity of the fluid.

The above law [Equation (3.15)] is employed when y^* is larger than 11.225. When the mesh is such that y^* is less than 11.225, the mean velocity profile is linear and follows the following equation:

$$U^* = y^* \tag{3.21}$$

In this study, as it is shown in Figure 3.1, we set the bottom boundary and the vertical boundary located at top of the water entrance (Section 3.10.3) as Wall boundary condition. Both of the Wall boundary conditions that we have in the domain were set as "no slip" with zero roughness.

3.8.3 Velocity inlet

The velocity inlet boundary condition is used to set the flow velocity at the inlet. The scalar properties of the flow are not fixed during a simulation and they change so as to provide the imposed velocity distribution.

When we use Velocity inlet as the boundary condition, the model will use the velocity components and the value of other scalar properties that we used for the boundary condition to calculate the mass flow rate, momentum fluxes, and fluxes of energy.

The mass flow rate entering a cell with velocity inlet boundary condition is computed as:

$$\dot{m} = \int \rho \vec{v}.d\vec{A} \tag{3.22}$$

As shown in Figure 3.1, we used the Velocity inlet boundary condition for the inlet of the water through the domain. In hydraulic jump, the depth and velocity and the corresponding Froude number at upstream will define the type of the jump. This research's main goal was to produce different types of the hydraulic jump by mathematical simulations, to analyse the air entrainment in the jump, and to compare the results with available laboratory experiments. We set the height of the water entrance equal to desired hydraulic jump upstream depth, and we chose the Velocity inlet for the entrance of the water to be able to set a fixed velocity for water to enter the domain. This imposes the desired velocity and depth at the same time.

An important point that we must consider in setting the velocity at the inlet is that, we must set the entrance velocity 5 to 10% larger than the desired upstream velocity because as the flow enters the domain and advances from the inlet, the average velocity will be decreased due to zero bed slope and the effects of zero velocity, at the bottom boundary. As a result, we must set a larger inlet velocity to compensate the reduction of the water velocity after entering the domain.

3.8.4 Pressure outlet

This kind of boundary condition is used when the static (gage) pressure at the outlet boundary is known. This kind of boundary condition is adjustable when we are dealing with open channel flow. We can specify the water free surface level at the outlet. The hydrostatic pressure distribution can be modelled at the outlet boundary.

In a hydraulic jump simulation, due to a transition of supercritical to subcritical flow, if we run the simulation in a transient state and just impose the water free surface level at the outlet boundary, the simulation will change the outlet boundary condition gradually from subcritical to supercritical (because the inlet flow velocity is high and the condition at the inlet is supercritical). In other words, the hydraulic jump will be washed away from the domain before taking place.

According to (Te Chow 1959) "a hydraulic jump will form in the channel if the Fr_1 of the flow, the flow depth y_1, and a downstream depth y_2 satisfy the equation 2.4. In order to form a balanced and static (in terms of location) hydraulic jump, we must impose a fixed hydrostatic pressure distribution at the outlet boundary during a simulation. To achieve a fixed pressure distribution at the outlet, firstly, we must set up the model such that it performs computations at the outlet boundary cells according to the imposed free surface level. It means that the model must perform calculations in a way that there is a certain depth of water at the outlet boundary. We should set the "Density interpolation method" at the pressure outlet boundary to "From free surface level". By this way, the model will assume that the outlet is full of water up to a certain depth and the density of fluid for those corresponding cells is the density of the water.

Secondly, since open channel boundary conditions in ANSYS fluent (by default) are controlled by the Froude number, in order to maintain stable calculations, it is better to change the solver setting in a way that the boundary conditions do not depend on the Froude number. This is possible by changing the setting in "Open channel controls". In this study, we considered the above

mentioned points in all the simulations and used the desired free surface level at the outlet, depending on the type of hydraulic jump being set.

3.9 Initial condition

Before running any simulation in ANSYS fluent, the initial condition (the condition at time equal to zero) of the entire computational domain must be set. Setting the initial condition properly is extremely critical and important for the stability of calculations and the reduction of computing time.

In Figure 3.3, the computational domain length was divided into two parts (each has a length of 3 m). The initial setting for the upstream part was supercritical. The depth and the velocity of water were equal to what we had at the pressure Inlet boundary condition. For the downstream section, the initial condition was subcritical and the velocity and depth were set equal to the desired hydraulic jump downstream. The velocity of air above the water surface was set at zero all over the domain.

Figure 3.3 shows the initial condition for one of the simulations in this study. Figure 3.3(a) shows the initial water depth, and Figure 3.3(b) demonstrates the initial velocity all over the channel.

Computations in this thesis make use of equations 3.1, 3.7, 3.8, 3.13 and 3.14.

(a)

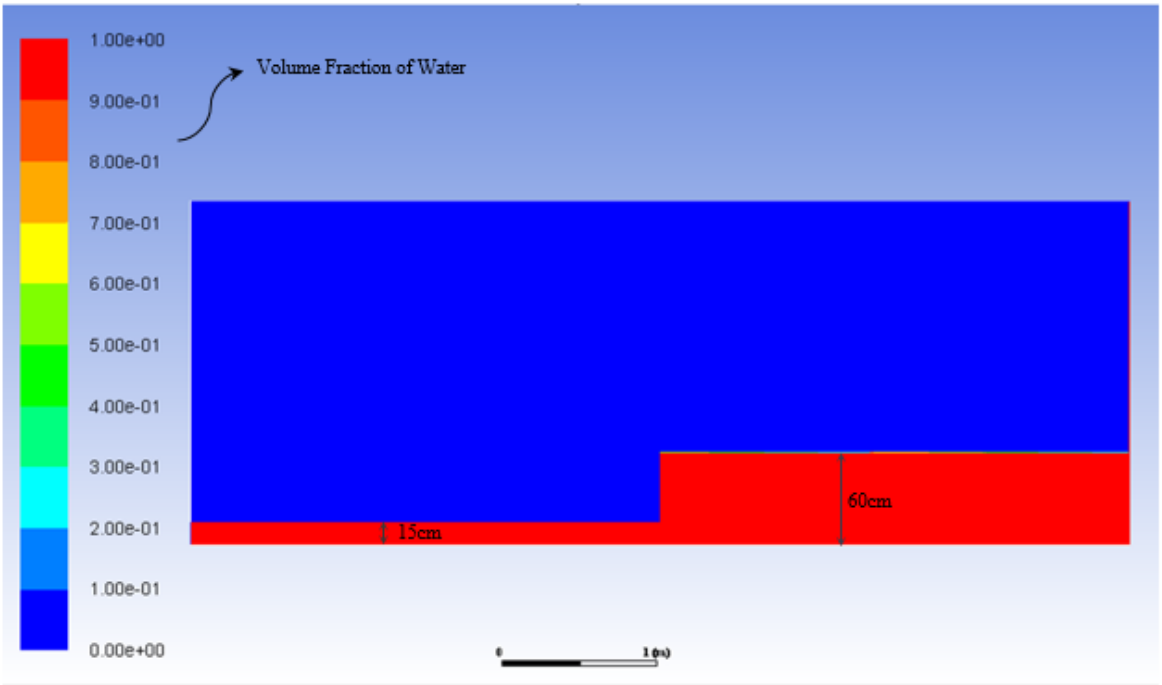
1.00e+00
9.00e-01
8.00e-01
7.00e-01
6.00e-01
5.00e-01
4.00e-01
3.00e-01
2.00e-01
1.00e-01
0.00e+00
Volume Fraction of Water
60cm
15cm

(b)

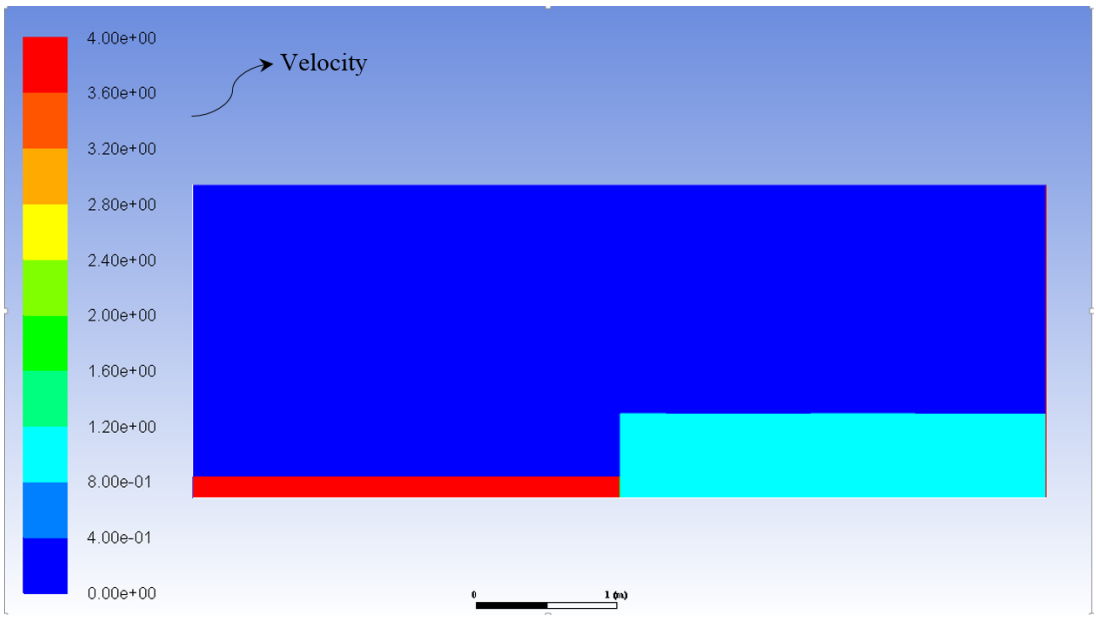
4.00e+00
3.60e+00
3.20e+00
2.80e+00
2.40e+00
2.00e+00
1.60e+00
1.20e+00
8.00e-01
4.00e-01
0.00e+00
Velocity

Figure 3.3 Initial conditions for computations: (a) the initial condition of the water surface for one of the simulation cases, and (b) the initial condition of the velocity for one of the simulation cases.

Chapter 4 Results and Discussions

4.1 Introduction

We predicted hydraulic jumps at four different values of the Froude number Fr_1 [Equation (2.6)], matching the experimental conditions of Chachereau and Chanson (2010), and compared the predicted air entrainment with their experimental data. In this chapter, we will describe some basic patterns of air entrainment in hydraulic jumps, as observed in the experiments of Chachereau and Chanson (2010), and will discuss the corresponding setup of CFD simulation cases in this research in order to facilitate a comparison between CFD and experimental results.

4.2 Air-water flow structure in hydraulic jumps

The hydraulic jump is the result of a rapid transformation from supercritical flow with high velocity to subcritical flow with low velocity and hence large depth. The sudden transition gives rise to turbulence, wavy free surface, water spray, energy dissipation, and air entrainment.

4.2.1 Inflow condition

According to Chanson (1995a, b), the flow characteristics of hydraulic jump depend on not only the upstream Froude number but also the distribution of inflow velocity. In a horizontal rectangular channel, inflow conditions for the occurrences of hydraulic jumps can be classified into three different types:

(1) A partially developed supercritical flow, meaning that the boundary layer is partially developed.

(2) A fully developed supercritical flow, meaning that the boundary layer is fully developed and the thickness of boundary layer is nearly equal to the upstream flow depth.

(3) A pre-entrained upstream flow, in which air entrainment has begun before the jump toe.

The boundary layer upstream of the jump toe (Figure 4.1) is a thin layer of fluid in the neighbourhood of the bottom surface of the channel (δ), where friction plays a significant role in the shape of vertical distribution of flow velocity. Across the boundary layer, the flow velocity increases from zero at the boundary (or the channel bottom) to the free-stream velocity at the outer edge of the boundary layer (Resch and Leutheusser, 1972).

In the experimental study of Chachereau and Chanson (2010), the inflow condition was partially developed. In this CFD research, hydraulic jumps occurs in a relatively short horizontal distance from the inlet of the computational channel (Figure 4.4). We expect the inflow to be partially developed, as will be confirmed later in this chapter.

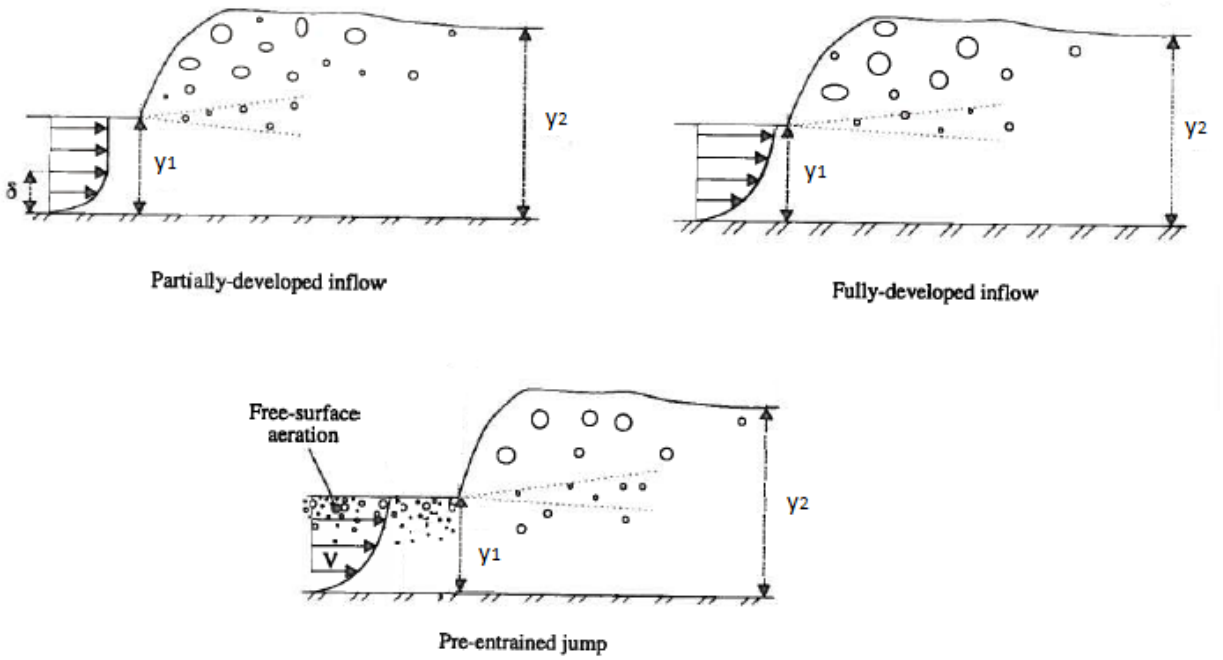

Figure 4.1 Sketch of hydraulic jumps under various inflow conditions (adopted from Chanson 1996, p. 76), where y_1 and y_2 are the upstream and downstream depths, respectively; δ is the boundary layer thickness; and v is the flow velocity.

4.2.2 Air entrainment and flow pattern

The general patterns of two-dimensional air-water flow in hydraulic jump in a rectangular channel are illustrated in Figure 4.2.

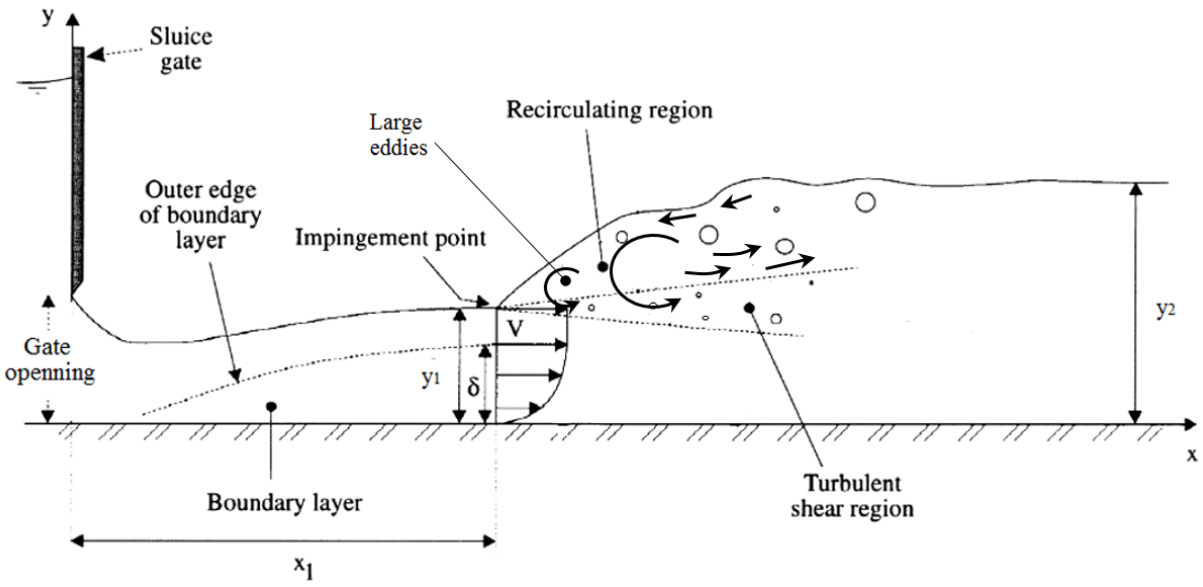

Figure 4.2 Patterns of two-dimensional air-water flow in hydraulic jump in a rectangular open channel (adopted from Chanson and Brattberg 2000).

Air mass is entrained into the rollers of the hydraulic jump by various mechanisms. If the upstream flow condition is pre-entrained, air bubbles that exist in the upstream flow will enter the jump rollers. Air mass near the free surface of the upstream flow is set into motion due to the friction force between water and air particles and the air mass in motion will enter the rollers at the impingement point (Chachereau and Chanson 2010). Another mechanism is the aspiration on the trumpet shape air streams formed at the jump toe at the intersection of the water jet with the rollers (Chanson and Brattberg 1998).

In Figure 4.2, the jump rollers consist of three virtual layers. The recirculation layer at the top is a strong unsteady flow with large bubbles. A recirculating flow and large eddies occur in this layer. At the bottom of the recirculating region, there is a shear region that contains an oscillating type of flow and smaller bubbles. The small bubbles can attach together and form larger bubbles as they travel downstream from the jump toe. These larger bubbles move toward the free surface and eventually form a foam layer at the top of jump rollers. In this region, the flow may contain large eddies from the recirculating layer. At the bottom of the shear region, there is an impingement jet region which has velocity patterns similar to the upstream flow. There are less or no air bubbles in this region.

4.2.3 Air volume fraction profile

Several studies (e.g. Resch and Leutheusser 1972; Chanson 1995a,b; Chanson 2006; Chachereau and Chanson 2010) showed that for hydraulic jumps with partially developed inflow condition the maximum air volume fraction in vertical air concentration distribution profile will happen in the shear region of the jump roller [Figure 4.3(a)]. Also these studies showed that this maximum will decreased as we go further from the jump toe toward downstream. Figure 4.3(b) show the general velocity distribution profile at the roller.

In Figures 4.3(a) and 4.3(b), C is the air volume fraction, C_{max} the maximum air volume fraction measured at the distance of Y_{Cmax} from the bottom, Y_{shear} is the distance of shear region boundary from the bottom, V is the velocity in the flow direction, V_{max} is the maximum velocity measured at the distance Y_{Vmax} from the bottom, and $Y_{0.5}$ is the vertical location where $V_x = 0.5V_{max}$.

From the results of our CFD test cases, we determine double average air volume fraction C_{mean} or average over depth and over time. This double average air volume fraction describes the rate of air entrainment in the hydraulic jump along each virtual vertical line after the jump toe. C_{mean} is given by

$$C_{mean} = \frac{1}{y_{90}} \int_0^{y_{90}} C dy \tag{4.1}$$

where C is the time averaged air volume fraction at a given depth, and y_{90} is the distance from the bottom of the cell in which the time averaged air volume fraction is 90%.

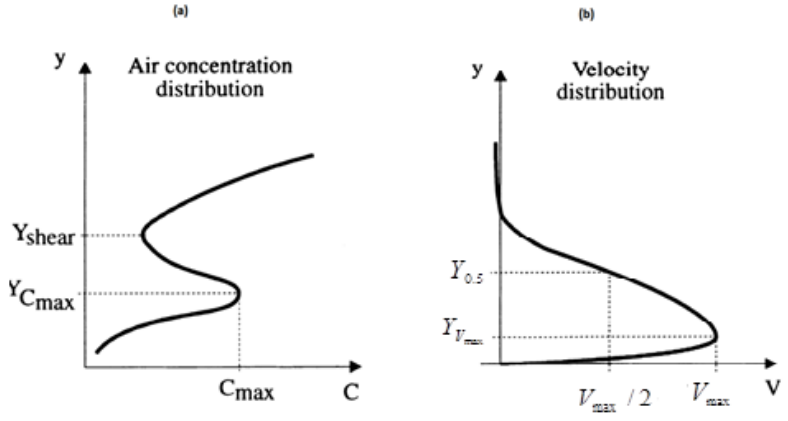

Figure 4.3 Vertical profiles in jump rollers of: (a) air concentration and (b) velocity (Adopted from Chanson and Brattberg 2000).

4.3 CFD simulation cases

The conditions of four simulation cases investigated in this CFD research are given in Table 4.2. To allow a comparison of results between CFD simulations and the experiments of Chachereau and Chanson (2010), what is important is to ensure a match in terms of the Froude number. Indeed, this is the case, as shown in the table. Note that our CFD simulations use a larger flow depth than the experiments, and hence are less problematic with respect to scale effects.

Table 4.1 Conditions of CFD simulations, in comparison with the experimental conditions of Chachereau and Chanson (2010).

Simulation case		Fr_1	y_1 (m)	y_2 (m)	V_1 (m/s)	V_2 (m/s)	Q (m^3/s)	Re_1
Case 1	CFD	3.1	0.1524	0.5963	3.7904	0.9688	0.0578	577662
	Experiment		0.0440	0.1721	2.0273	0.5182	0.0446	89000
Case 2	CFD	3.8	0.1524	0.7463	4.6463	0.9488	0.0708	708102
	Experiment		0.0405	0.1983	2.4198	0.4941	0.049	98000
Case 3	CFD	4.4	0.1524	0.8752	5.3800	0.9369	0.0820	819907
	Experiment		0.0395	0.2268	2.7595	0.4805	0.0545	110000
Case 4	CFD	5.1	0.1524	1.026	6.2359	0.9266	0.0950	950347
	Experiment		0.0395	0.2658	3.1747	0.4717	0.0627	130000

Note that the hydraulic jump phenomenon is typically unsteady, and variables such as voice fraction and velocity fluctuate continuously. Thus, it is appropriate to analyse air entrainment and velocity distributions using time average. This entails sampling flow properties with a certain frequency and for a certain period of time, and processing CFD output data for final analysis. In Chachereau and Chanson (2010), the frequency of sampling at each point was 20 Hz and the sampling period was 45 s. Our CFD simulations commenced from initial conditions (see Section 3.10.5), produced stable and balanced hydraulic jumps after 12 s of model time, and continued for another 12 s. The CFD outputs of dependent variables were sampled at a frequency of 20 Hz over the time period of 12 to 24 s for determining time averaged values.

Each of the CFD simulations produced y_1 and y_2 (Figure 2.1) values. The amount of energy loss in the hydraulic jump can be calculated using Equation (2.9).

For each of the four simulation cases, we examined the vertical distributions of air volume fraction at up to four selected longitudinal locations (Table 4.2) downstream of the jump toe. Air volume fraction and velocity profiles are extracted from the CDF outputs for these locations after the impingement point. The selected locations correspond to those reported in Chachereau and Chanson (2010). In Table 4.2, x is the longitudinal distance of the locations from the inlet of the model channel, x_1 is the longitudinal distance of the jump toe from the inlet, and y_1 is the depth of flow upstream of the jump toe (Figure 4.1). For all the cases, the normal distance $(x - x_1)/y_1$ is the same between Chachereau and Chanson (2010) and this study.

Table 4.2 Four selected longitudinal locations for examinations of air volume fraction and vertical velocity distributions.

Simulation case	Fr_1	$(x - x_1)/y_1$			
1	3.1	0.91	1.7	3.41	6.82
2	3.8	1.18	3.61	7.23	10.8
3	4.4		3.8	7.59	11.4
4	5.1	3.8	7.59	11.4	15.2

4.4 Predicted flow field and air volume distribution

This section presents predictions of time-averaged water surface profiles, the flow field, and air volume fraction distributions for each of the four simulation cases, and compare the predicted air volume fraction distributions with the experimental data of Chachereau and Chanson (2010). Note that locating the jump toe is critical. In the hydraulic jump phenomenon, the location of the jump toe fluctuates back and forth constantly. Laboratory experiments usually applies time averaging to determine the distance x_1 of the jump toe from the inlet from the visual observations of instantaneous locations of the moving jump toe. In this study, we have the time averaged value of air volume fraction for each cell of the model channel. At the jump toe, the flow consists of a mixture of the two phases (air and water). In this study, it is assumed that the existence of this mixture would begin when a layer of fluid with a more than 50 percent as water volume fraction would start to rise from the water free surface. In Figure 4.4 and 4.5 this layer is coloured with light green according to water volume fraction legend on the left hand side of the Figure. In this study, the start of formation of this layer is considered as the jump toe location.

4.4.1 Simulation case 1

For simulation case 1, the upstream Froude number is $Fr_1 = 3.1$. The hydraulic jump is classified as form B, as discussed in Section 2.3. In Figure 4.4, contours of time averaged water volume fraction are shown. The location of the jump toe is $x_1 = 2.43$ m downstream of the inlet.

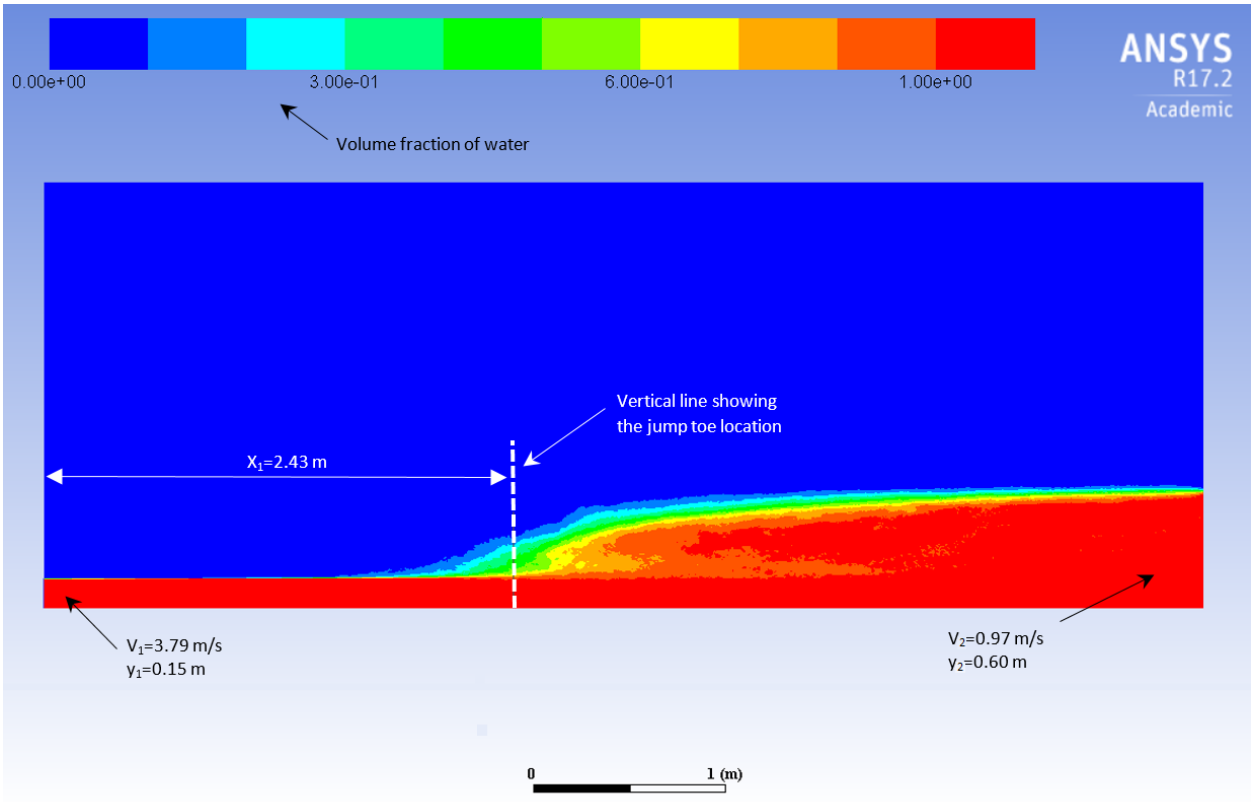

Figure 4.4 Time averaged distribution of water volume fraction for simulation case 1, in which the upstream Froude number is $Fr_1 = 3.1$.

In Figure 4.5, the distribution of flow velocity vectors, along with contours of time-averaged water volume fraction, at the last time step of the simulation, is plotted. The magnitudes of the vectors are shown by the lengths of the vectors. The colour scale for the vectors shows time-averaged water volume fraction. The water surface profile after the jump toe clearly defines a hydraulic jump.

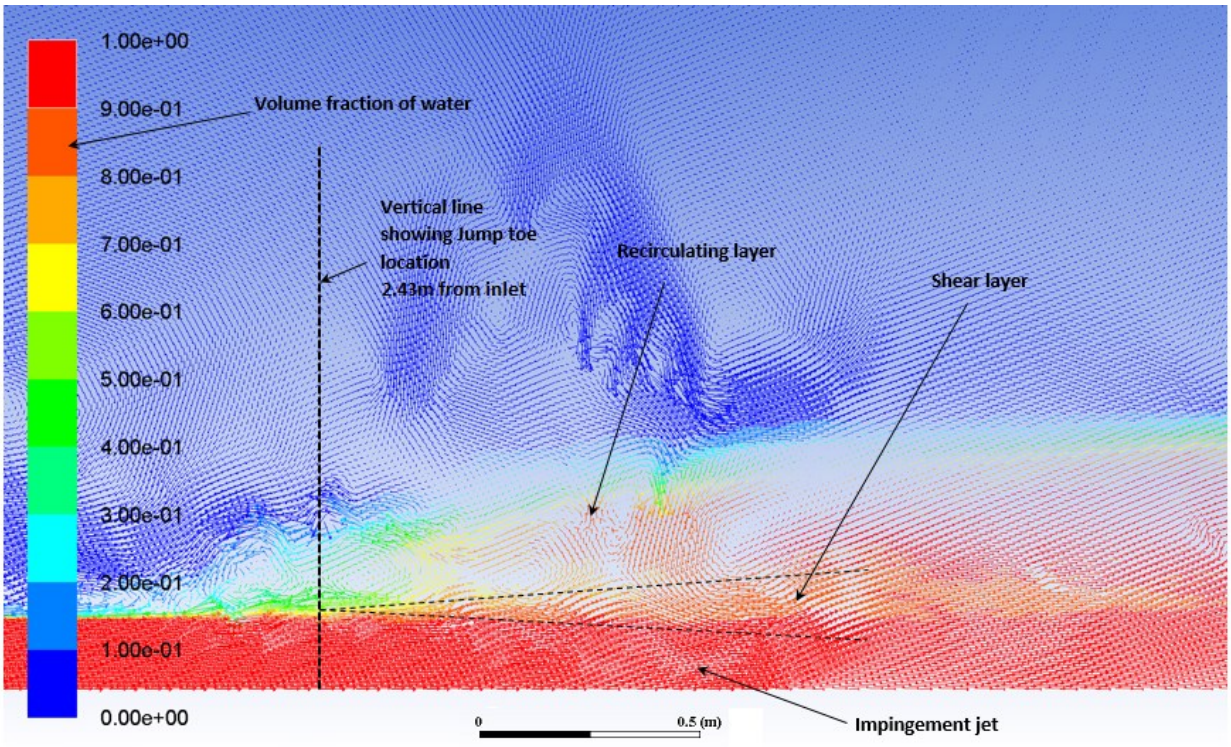

Figure 4.5 Distributions of flow velocity vectors and time-averaged water volume fraction in the hydraulic jump for simulation case 1. The upstream Froude number is $Fr_1 = 3.1$ (Table 4.1 and Table 4.2)

In Figures 4.6 to 4.9, we plotted vertical profiles of predicted time-averaged air volume fraction at four selected locations (Table 4.3) along the length of the model channel downstream of the jump toe. The experimental data of Chachereau and Chanson (2010) are shown as solid circles in the Figures for comparison purposes. Note that the predictions and experimental data match in location in terms of $(x - x_1)/y_1$. In Figure 4.6, the predicted maximum air volume fraction occurs in the shear region (Figure 4.5), whose upper boundary is located at $y = 0.26$ m above the channel bottom. The maximum air volume fraction is equal to 0.48, and occurs at $y = 0.23$ m. The predicted profile (Figure 4.7) gives a depth-averaged air volume fraction of $C_{mean} = 0.36$ at $(x - x_1)/y_1 = 0.91$. C_{mean} is defined in Equation (4.1).

Table 4.3 Selected longitudinal locations for the examination of air entrainment and flow velocity pattern sampling lines for simulation case 1 (Tables 4.1 and 4.2). The distance of the jump toe from the inlet is 2.43 m.

Selected location	1	2	3	4
Distance from the inlet (m)	2.569	2.689	2.950	3.469

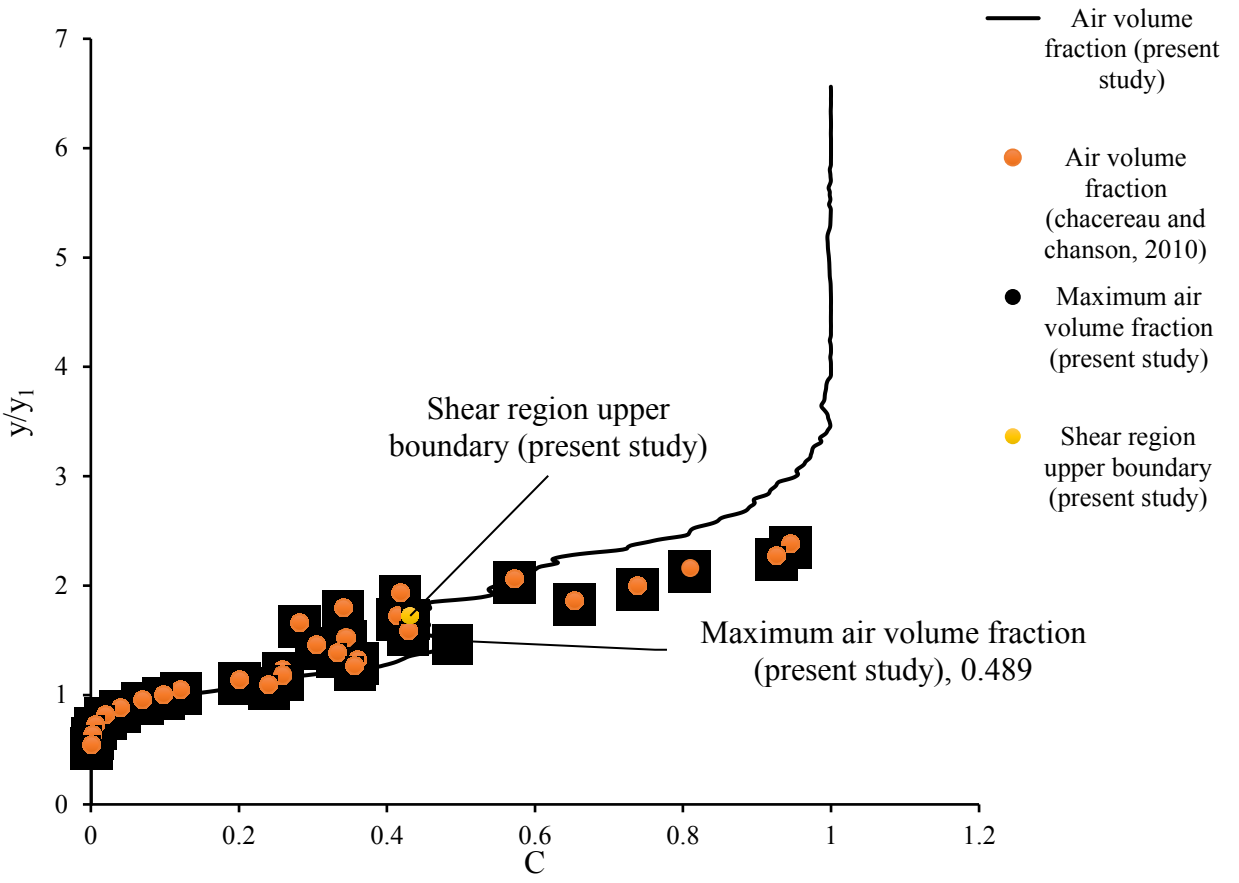

Figure 4.6 Vertical profile of time-averaged air volume fraction at $(x - x_1)/y_1 = 0.91$ for simulation case 1 with $Fr_1 = 3.1$.

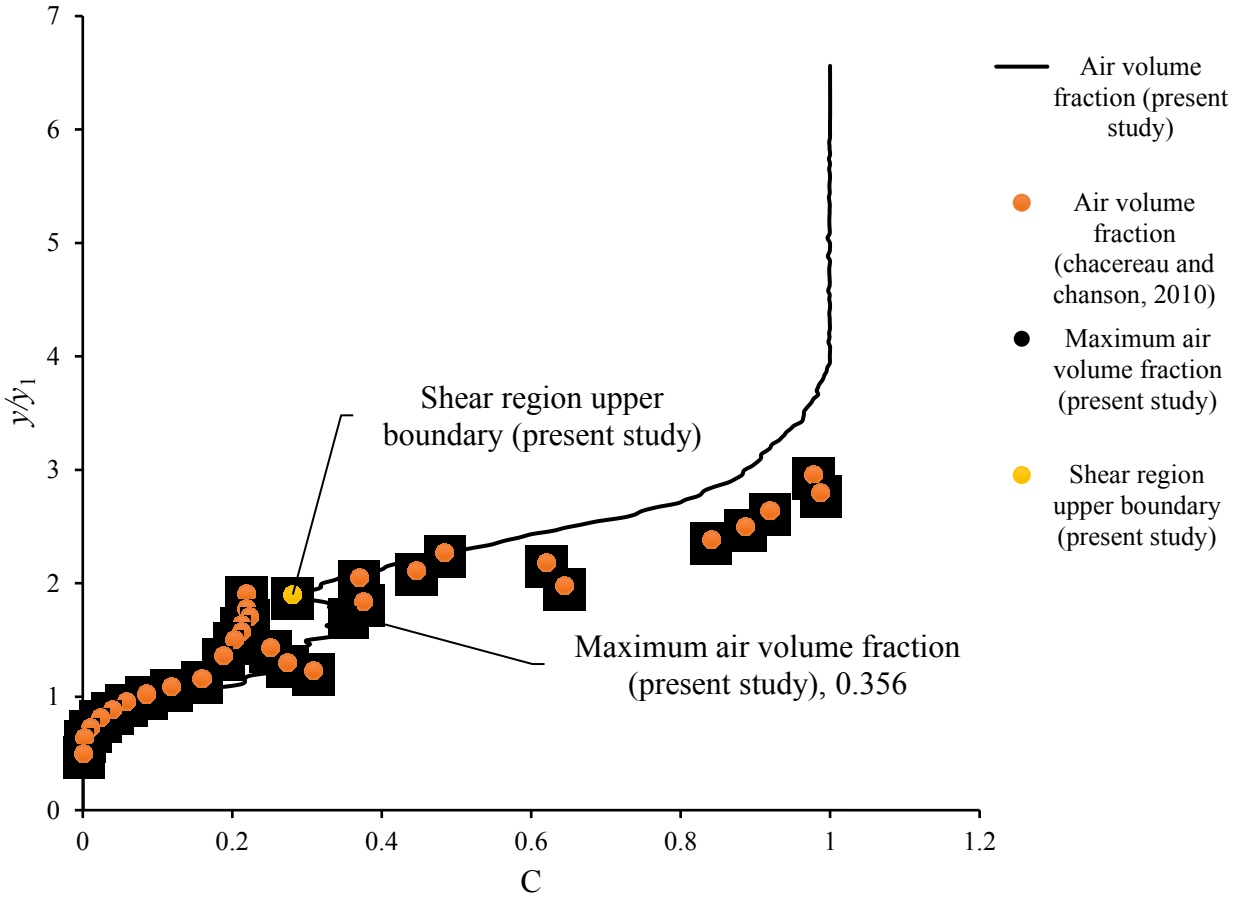

Figure 4.7 Vertical profile of time-averaged air volume fraction at $(x - x_1)/y_1 = 1.7$ for simulation case 1 with $Fr_1 = 3.1$.

In Figure 4.7, the predicted maximum air volume fraction is 0.36, occurring at y = 0.26 m in the shear region (Figure 4.5). The upper boundary of the shear region is located at 0.28 m above the channel bottom. Below the water surface, the predicted profile (Figure 4.7) gives a depth-averaged air volume fraction of $C_{mean} = 0.32$ at $(x - x_1)/y_1 = 1.7$.

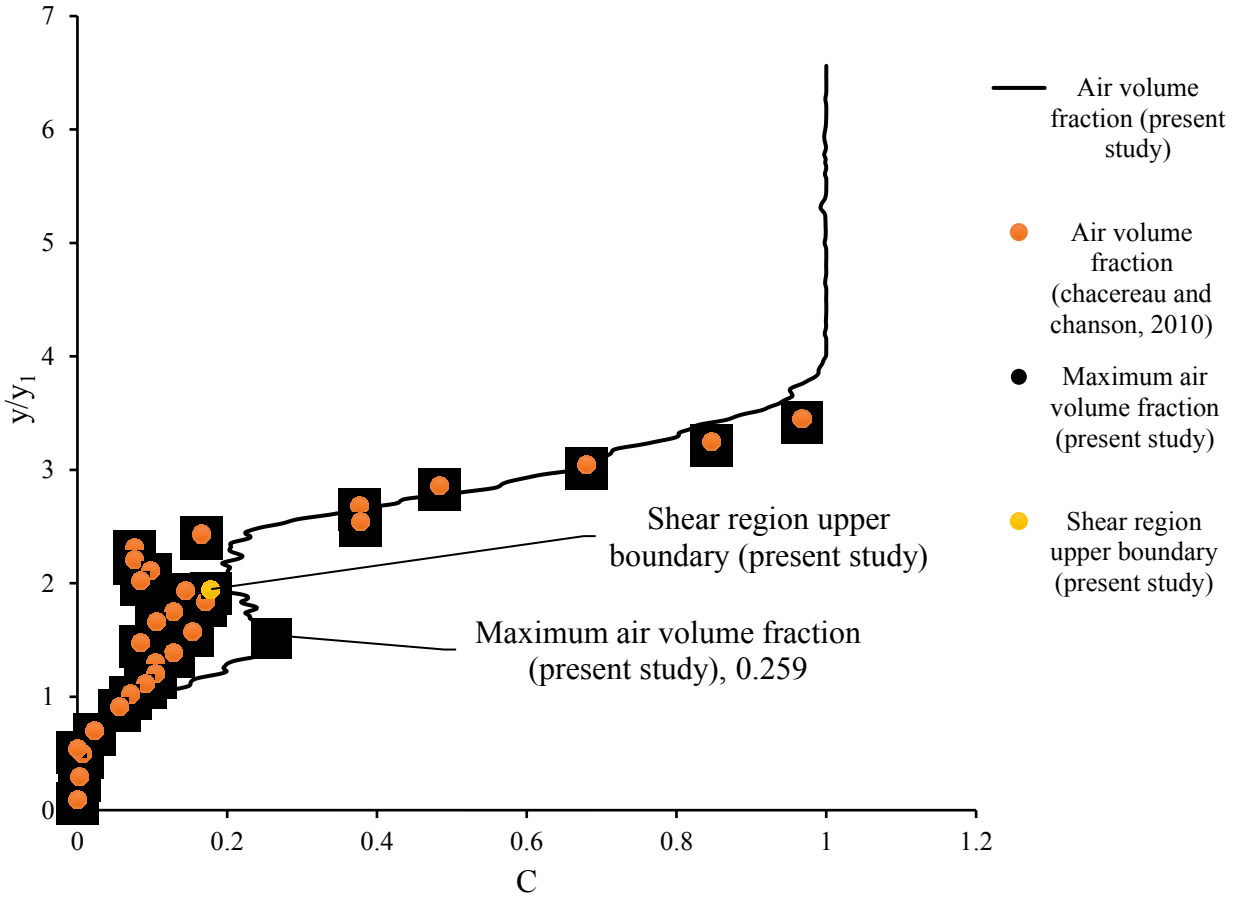

Figure 4.8 Vertical profile of time-averaged air volume fraction at $(x - x_1)/y_1 = 3.41$ for simulation case 1 with $Fr_1 = 3.1$.

In Figure 4.8, the predicted maximum air volume fraction is 0.26, occurring at y = 0.24 m in the shear region (Figure 4.5). The upper boundary of the shear region is located at 0.30 m above the bottom. Below the water surface, the predicted profile (Figure 4.8) gives a depth-averaged air volume fraction of $C_{mean} = 0.27$ at $(x - x_1)/y_1 = 3.41$.

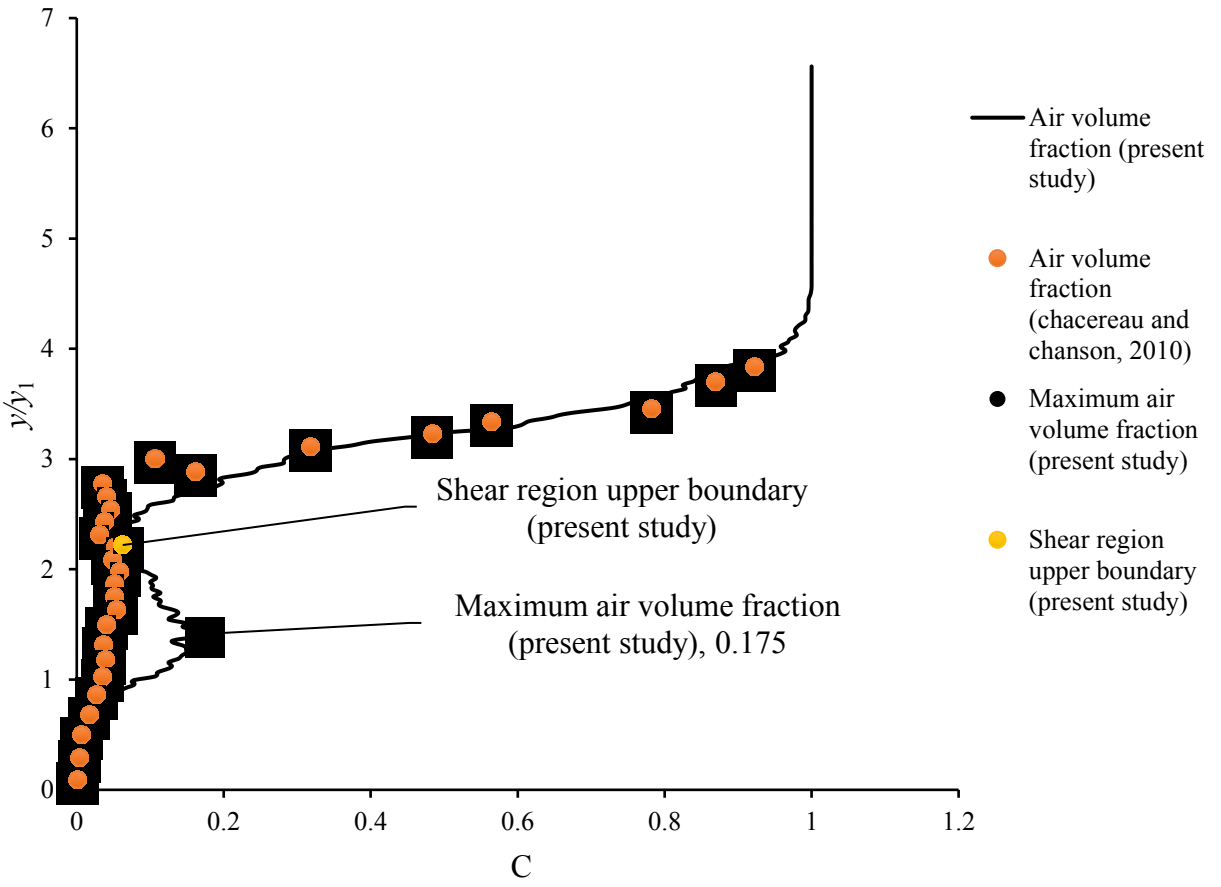

Figure 4.9 Vertical profile of time-averaged air volume fraction at $(x - x_1)/y_1 = 6.82$ for simulation case 1 with $Fr_1 = 3.1$.

In Figure 4.9, the predicted maximum air volume fraction is 0.17, occurring at y = 0.22 m in the shear region. The upper boundary of shear region from the channel bottom is located at 0.34 m. Below the water surface, the predicted profile (Figure 4.9) gives a depth-averaged air volume fraction of $C_{mean} = 0.21$ at $(x - x_1)/y_1 = 6.82$.

The predicted vertical profiles of air volume fraction (Figures 4.6 – 4.9) appear to plot through the experimental data points. There are discrepancies between the predictions and the measurements in some portion of the shear region, where the CFD model has over-predicted air volume fraction. The CFD predictions of air volume fraction being higher than the experimental values are possibly due to the scale effect. The experiments of Chachereau & Chanson (2010) were limited to the use of experimental setup of smaller dimensions, compared to the model channel (Figure 3.1) used in this CFD work.

The vertical profiles (Figures 4.6 – 4.9) show variations in air volume fraction with depth below the water surface. For the analysis of hydraulic jumps, depth-averaged air volume fraction, C_{mean}, given in Equation (4.1), between the water surface and the channel bottom is a useful parameter. In Figure 4.10, we compare the predicted distribution of C_{mean} along the length of the model channel with Chachereau and Chanson's (2010) experimental data. The predictions appear to give overestimates of C_{mean} values.

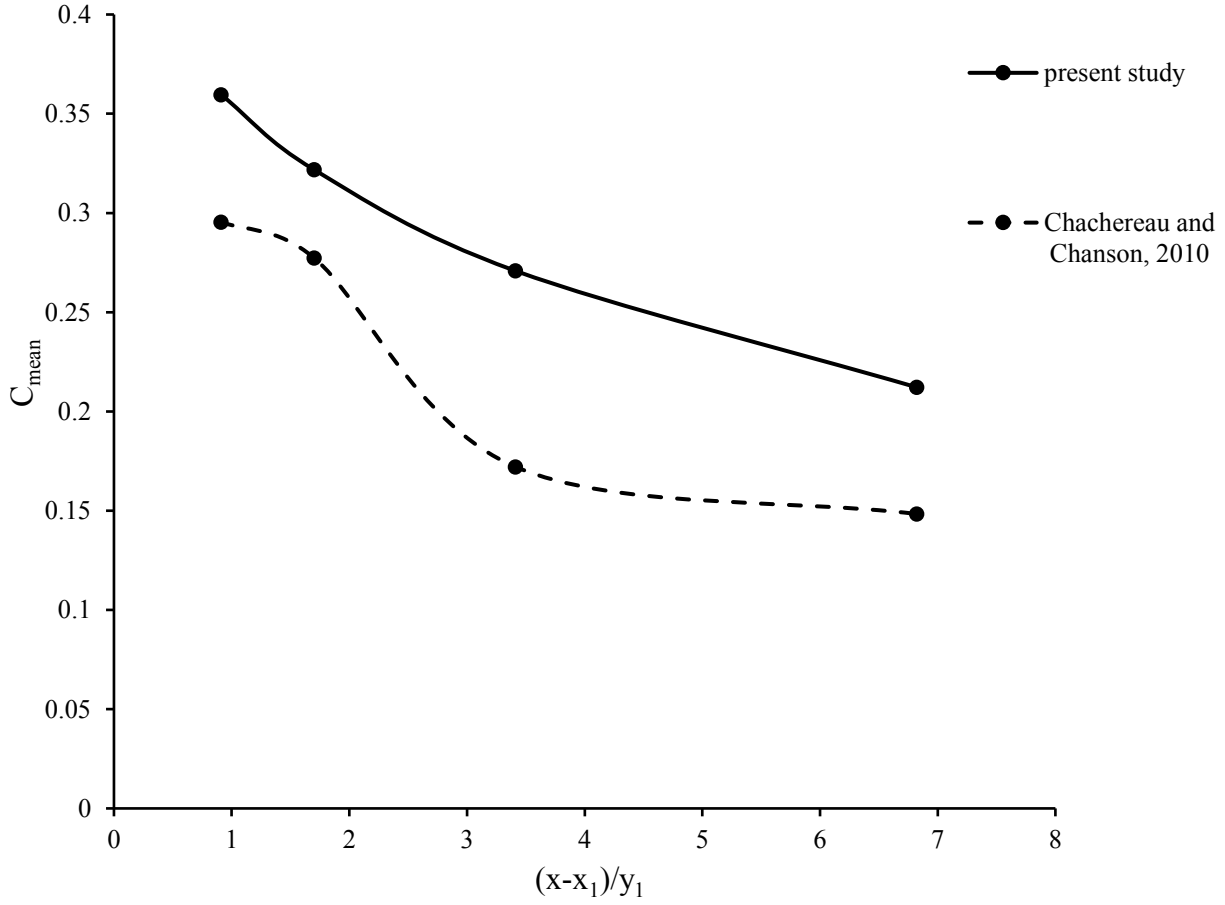

Figure 4.10 Distributions of predicted and measured depth-averaged air volume fraction for simulation case 1. The upstream Froude number is $Fr_1 = 3.1$.

The CFD model produced distributions of the longitudinal velocity component, V_x, at different depth between the channel bottom and the free surface, which are difficult to measure from laboratory experiments. In Figure 4.11(a)-4.11(d), we show the vertical distributions of V_x

between the channel bottom and the height, at which the air volume fraction is C ≥ 0.5, at four selected longitudinal locations. At each of the location, the maximum value of V_x and the vertical distance above the channel bottom where the maximum value occurs are indicated. In Figure 4.11(a)–4.11(c), V_x has negative values in the top portion of the profiles. These negative values mean reverse flow in the recirculation region immediately below the free water surface.

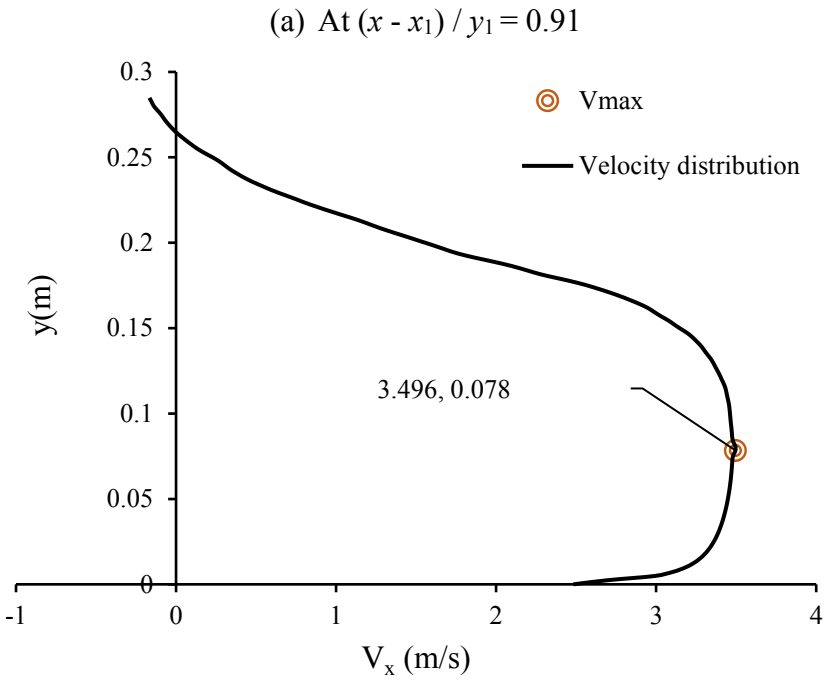

(b) At $(x - x_1) / y_1 = 1.71$

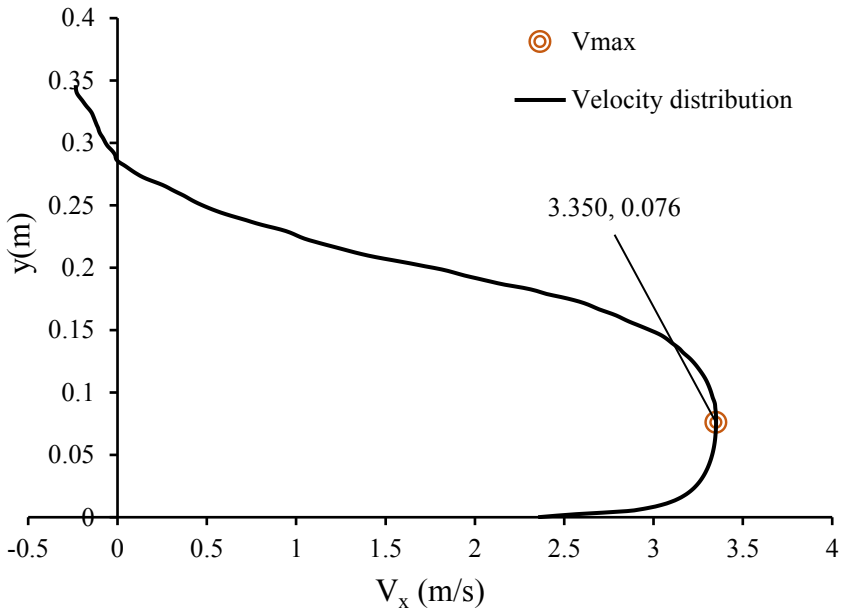

(c) At $(x - x_1) / y_1 = 3.41$

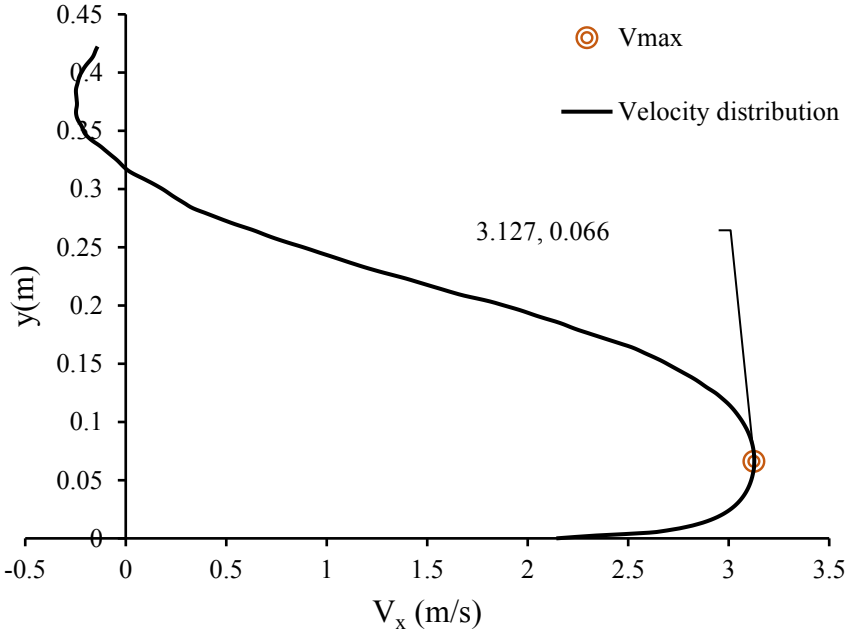

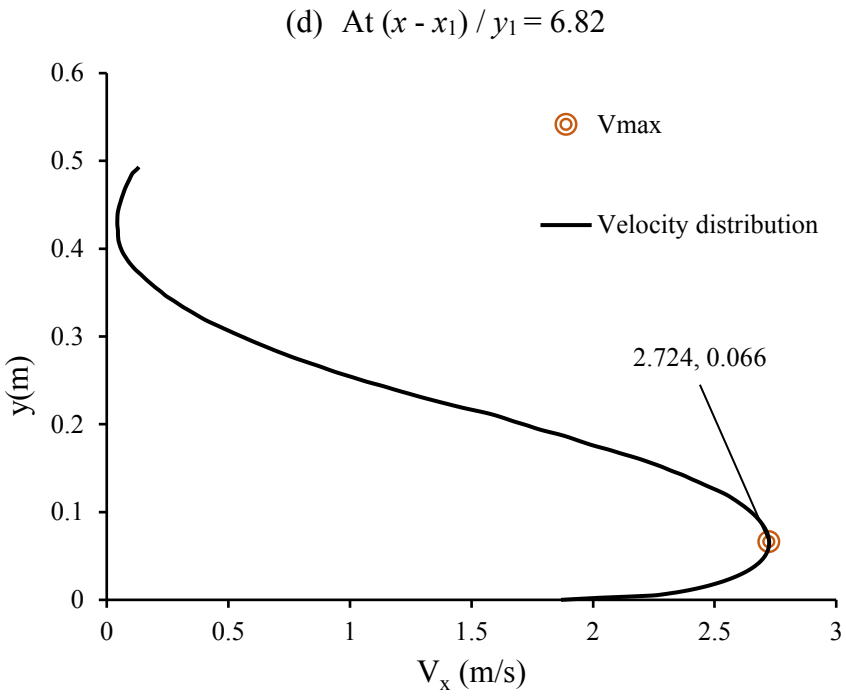

Figure 4.11 Vertical profiles of the time - averaged longitudinal velocity component below the free surface for simulation case 1, with $Fr_1 = 3.1$.

4.4.2 Simulation case 2

For simulation case 2, the upstream Froude number is $Fr_1 = 3.8$. The hydraulic jump is classified as form B, as discussed in Section 2.3. In Figure 4.12, contours of time averaged water volume fraction are shown. The location of the jump toe is $x_1 = 2.06$ m downstream of the inlet.

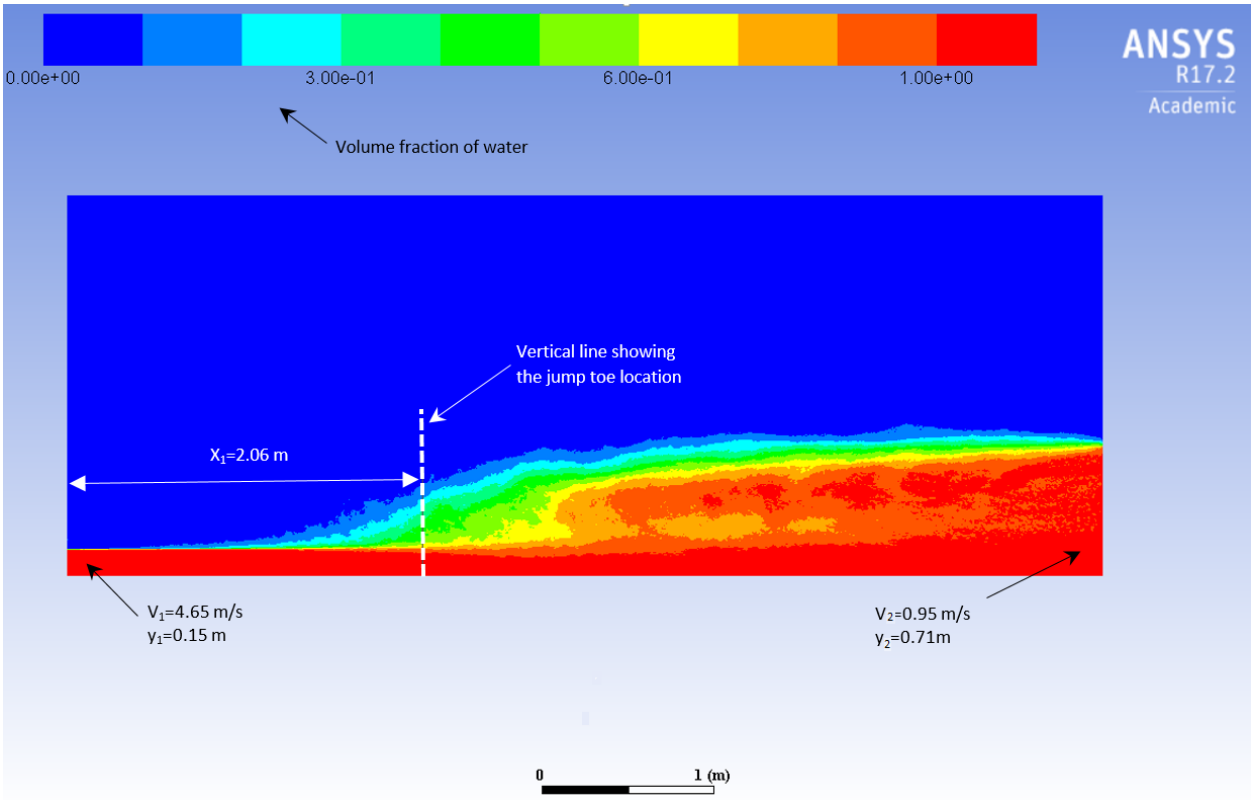

Figure 4.12 Time averaged distribution of water volume fraction for simulation case 2, in which the upstream Froude number is $Fr_1 = 3.8$.

In Figure 4.13, the distribution of flow velocity vectors, along with contours of time-averaged water volume fraction, at the last time step of the simulation, is plotted. The magnitudes of the vectors are shown by the lengths of the vectors. The colour scale for the vectors shows time-averaged water volume fraction. The water surface profile after the jump toe clearly defines a hydraulic jump.

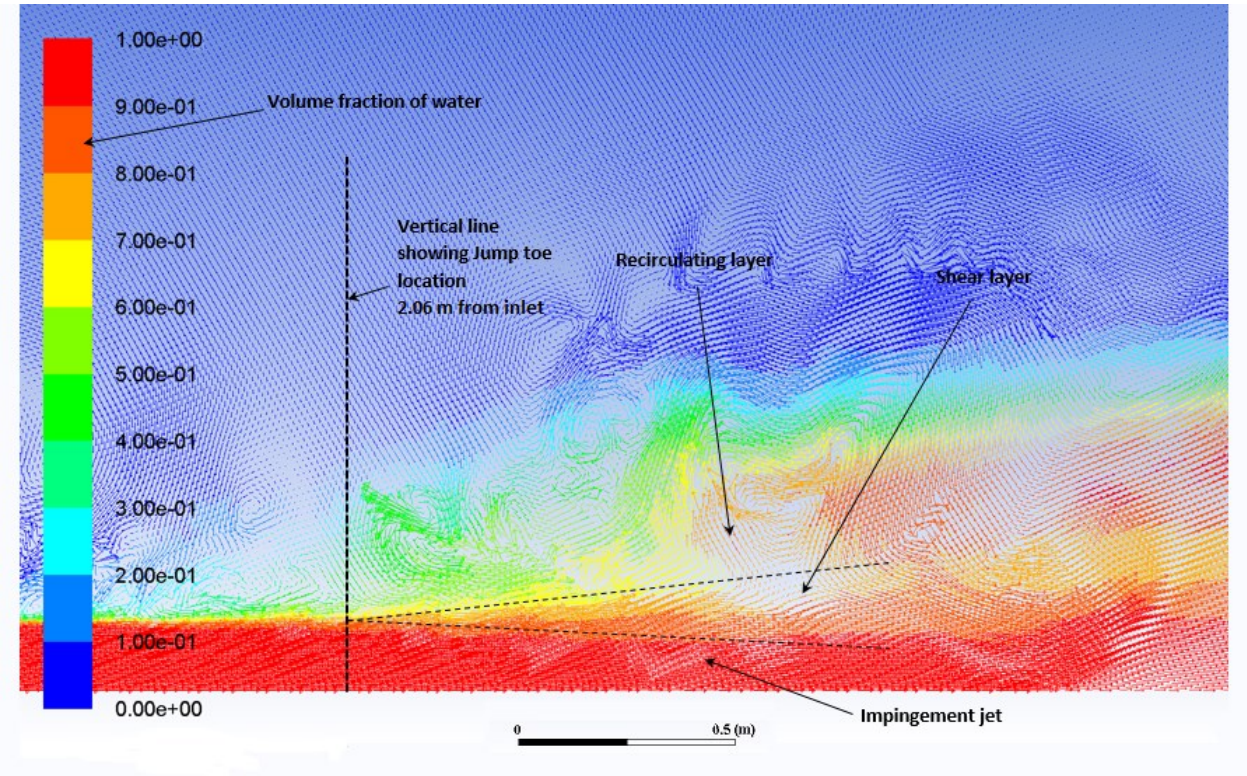

Figure 4.13 Distributions of flow velocity vectors and time-averaged water volume fraction in the hydraulic jump for simulation case 2. The upstream Froude number is $Fr_1 = 3.8$ (Table 4.1 and Table 4.2)

In Figures 4.14 to 4.17, we plotted vertical profiles of predicted time-averaged air volume fraction at four selected locations (Table 4.4) along the length of the model channel downstream of the jump toe. The experimental data of Chachereau and Chanson (2010) are shown as solid circles in the Figures for comparison purposes. Note that the predictions and experimental data match in location in terms of $(x - x_1)/y_1$. In Figure 4.14, the predicted maximum air volume fraction occurs in the shear region (Figure 4.13), whose upper boundary is located at $y = 0.32$ m above the channel bottom. The maximum air volume fraction is equal to 0.46, and occurs at $y = 0.26$ m. The predicted profile (Figure 4.14) gives a depth-averaged air volume fraction of $C_{mean} = 0.45$ at $(x - x_1)/y_1 = 1.81$. C_{mean} is defined in Equation (4.1).

Table 4.4 Selected longitudinal locations for the examination of air entrainment and flow velocity pattern sampling lines for simulation case 2 (Tables 4.1 and 4.2). The distance of the jump toe from the inlet is 2.06 m.

Selected location	1	2	3	4
Distance from the inlet (m)	2.369	2.489	2.75	3.269

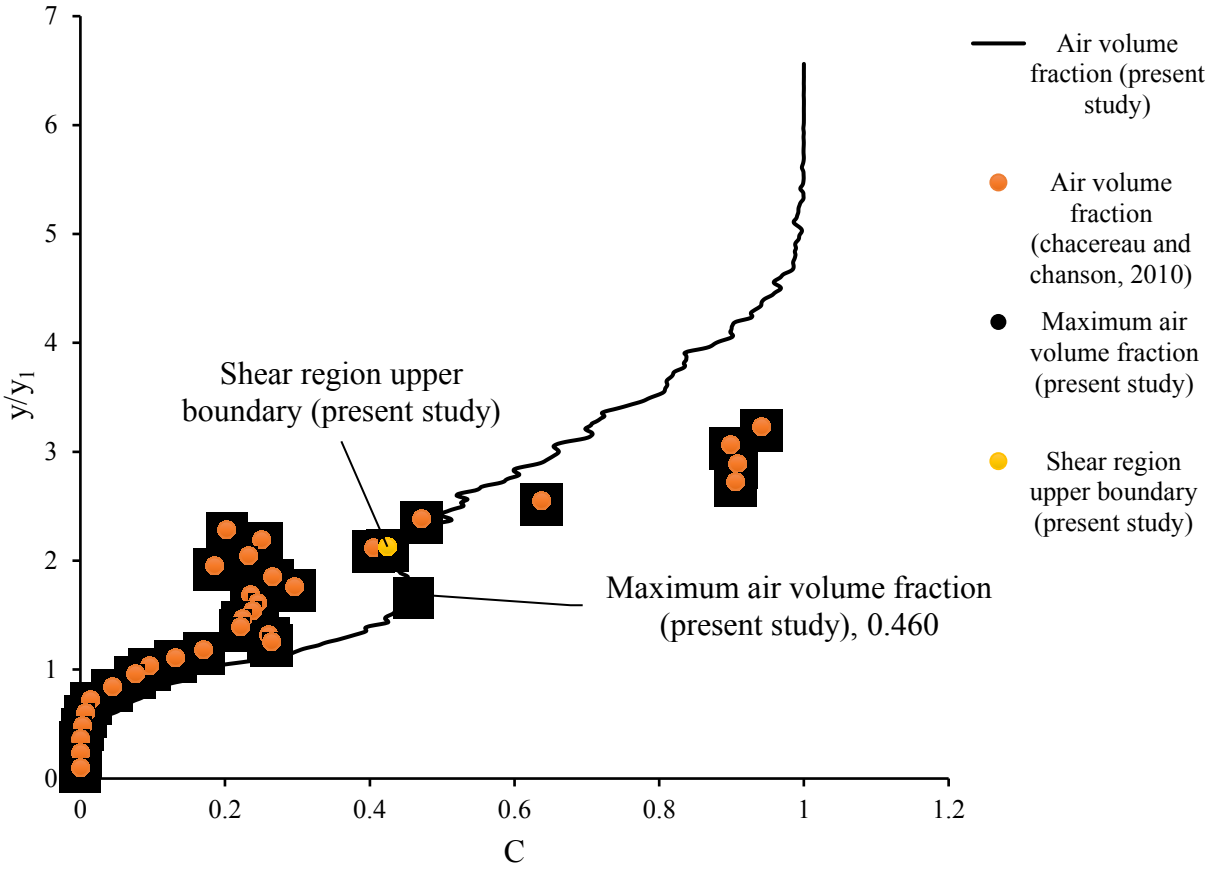

Figure 4.14 Vertical profile of time-averaged air volume fraction at $(x - x_1)/y_1 = 1.81$ for simulation case 2 with $Fr_1 = 3.8$.

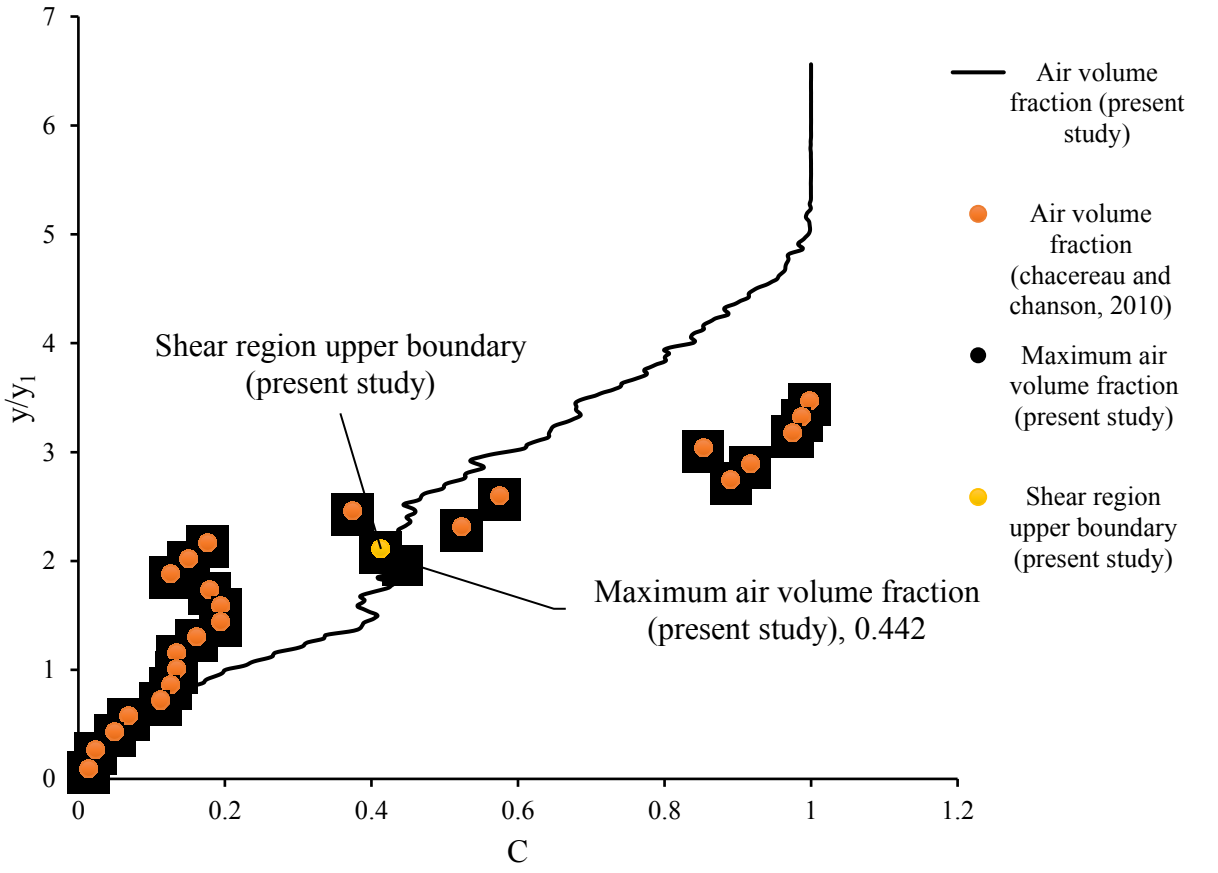

Figure 4.15 Vertical profile of time-averaged air volume fraction at $(x - x_1)/y_1 = 3.81$ for simulation case 2 with $Fr_1 = 3.8$.

In Figure 4.15, the predicted maximum air volume fraction is 0.44, occurring at y = 0.30 m in the shear region (Figure 4.13). The upper boundary of the shear region is located at 0.32 m above the channel bottom. The predicted profile (Figure 4.15) gives a depth-averaged air volume fraction of $C_{mean} = 0.44$ at $(x - x_1)/y_1 = 3.81$.

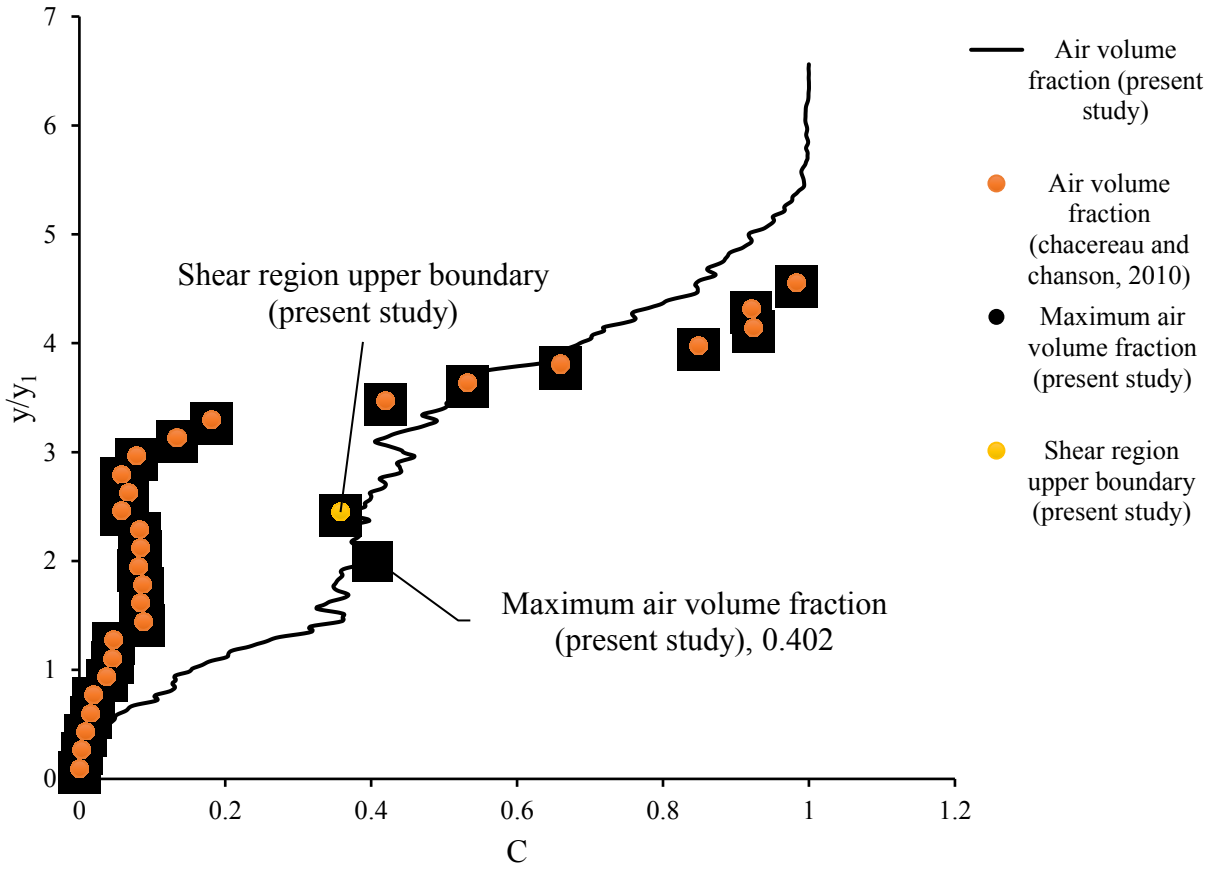

Figure 4.16 Vertical profile of time-averaged air volume fraction at $(x - x_1)/y_1 = 7.23$ for simulation case 2 with $Fr_1 = 3.8$.

In Figure 4.16, the predicted maximum air volume fraction is 0.40, occurring at y = 0.31 m in the shear region (Figure 4.13). The upper boundary of the shear region is located at 0.37 m above the bottom. The predicted profile (Figure 4.16) gives a depth-averaged air volume fraction of $C_{mean} = 0.41$ at $(x - x_1)/y_1 = 7.23$.

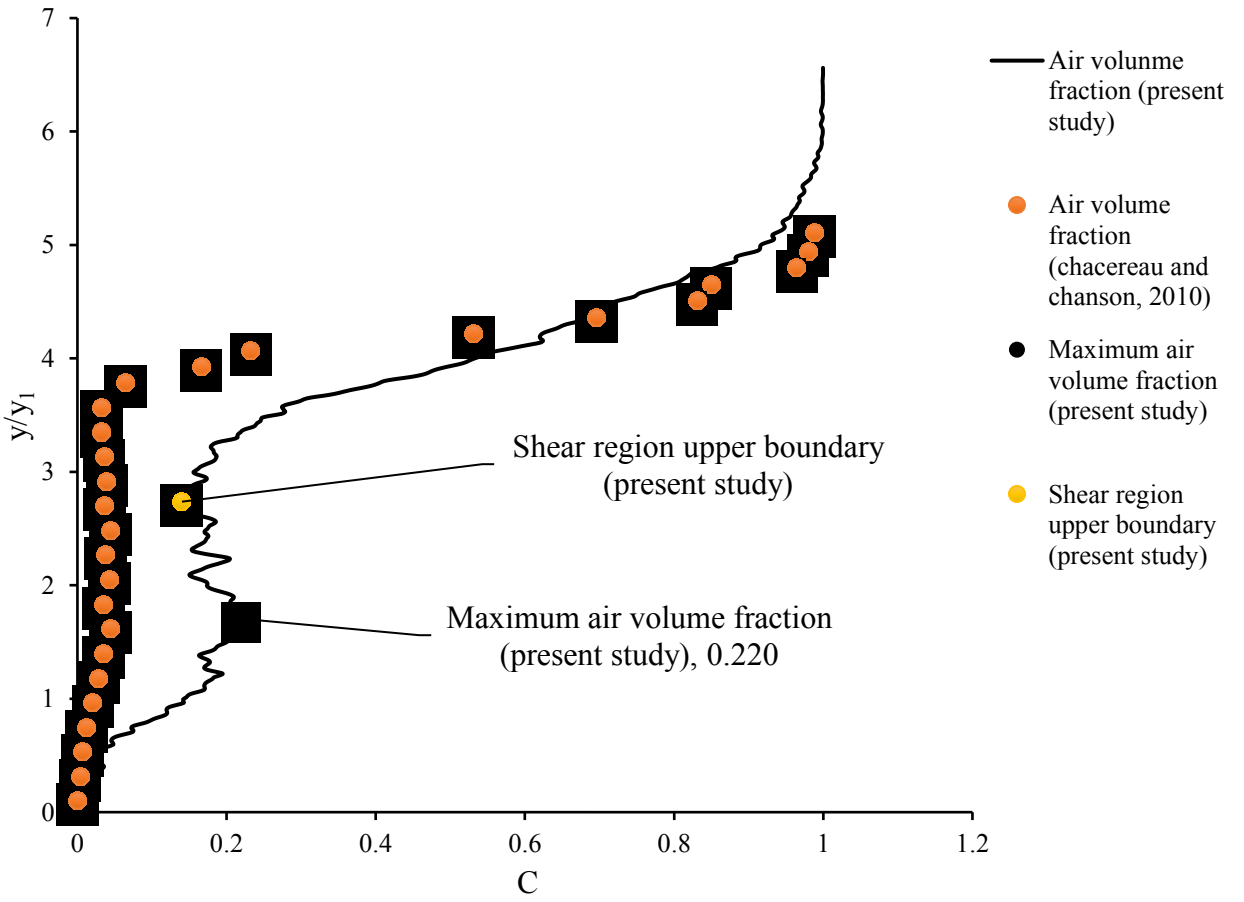

Figure 4.17 Vertical profile of time-averaged air volume fraction at $(x - x_1)/y_1 = 10.8$ for simulation case 2 with $Fr_1 = 3.8$.

In Figure 4.17, the predicted maximum air volume fraction is 0.22, occurring at y = 0.26 m in the shear region. The upper boundary of shear region from the channel bottom is located at 0.42 m. The predicted profile (Figure 4.17) gives a depth-averaged air volume fraction of $C_{mean} = 0.28$ at $(x - x_1)/y_1 = 10.8$.

As shown in Figures 4.14–4.17, there are some discrepancies between the CFD results and Chachereau and Chanson's (2010) measurements, especially in the shear region. The discrepancies may result from a number of factors:

(1) The measurements were made using a double-tip conductivity probe that detected the instantaneous presence of air or water at discrete time steps with a sampling frequency of 20 Hz. The detection was based on the difference in electrical resistance between air and water. At each sampling time, the probe recorded the presence of either water (C = 0) or

air (C = 1). These presence and absence records were used to obtain average values. Our CFD results give continuous values (between 0 and 100%) of air volume fraction in each cell of the model domain at every sampling step. These continuous records would produce more accurate time averages of air volume fraction air volume fraction.

(2) In simulation case 2, at the upstream Froude number of $Fr_1 = 3.8$, the hydraulic jump belongs to group B (see Section 2.3). Group B jumps have an oscillating nature. They are the most unsteady hydraulic jump, with their toes moving back and forth in the longitudinal direction. Because of such movement, there are uncertainties in the longitudinal coordinates (relative to the jump toe) of sampling cross sections, as determined both in the laboratory channel and in the CFD channel. It is difficult to match exactly the toe positon between experiments and simulations. This can cause discrepancies between the measurements and predictions at cross sections downstream of the jump toe. In fact, for highly oscillating types of jumps, it is problematic to locate the jump toe by visual observations in experiments. It is less problematic in CFD simulations, because we used time averaged air volume fraction in all the cells to location the jump toe.

(3) Scale effect is another possible factor, as explained earlier.

The vertical profiles (Figures 4.14 – 4.17) show variations in air volume fraction with depth below the water surface. For the analysis of hydraulic jumps, depth-averaged air volume fraction, C_{mean}, given in Equation (4.1), between the water surface and the channel bottom is a useful parameter. In Figure 4.18, we compare the predicted distribution of C_{mean} along the length of the model channel with Chachereau and Chanson's (2010) experimental data. The predictions appear to give overestimates of C_{mean} values.

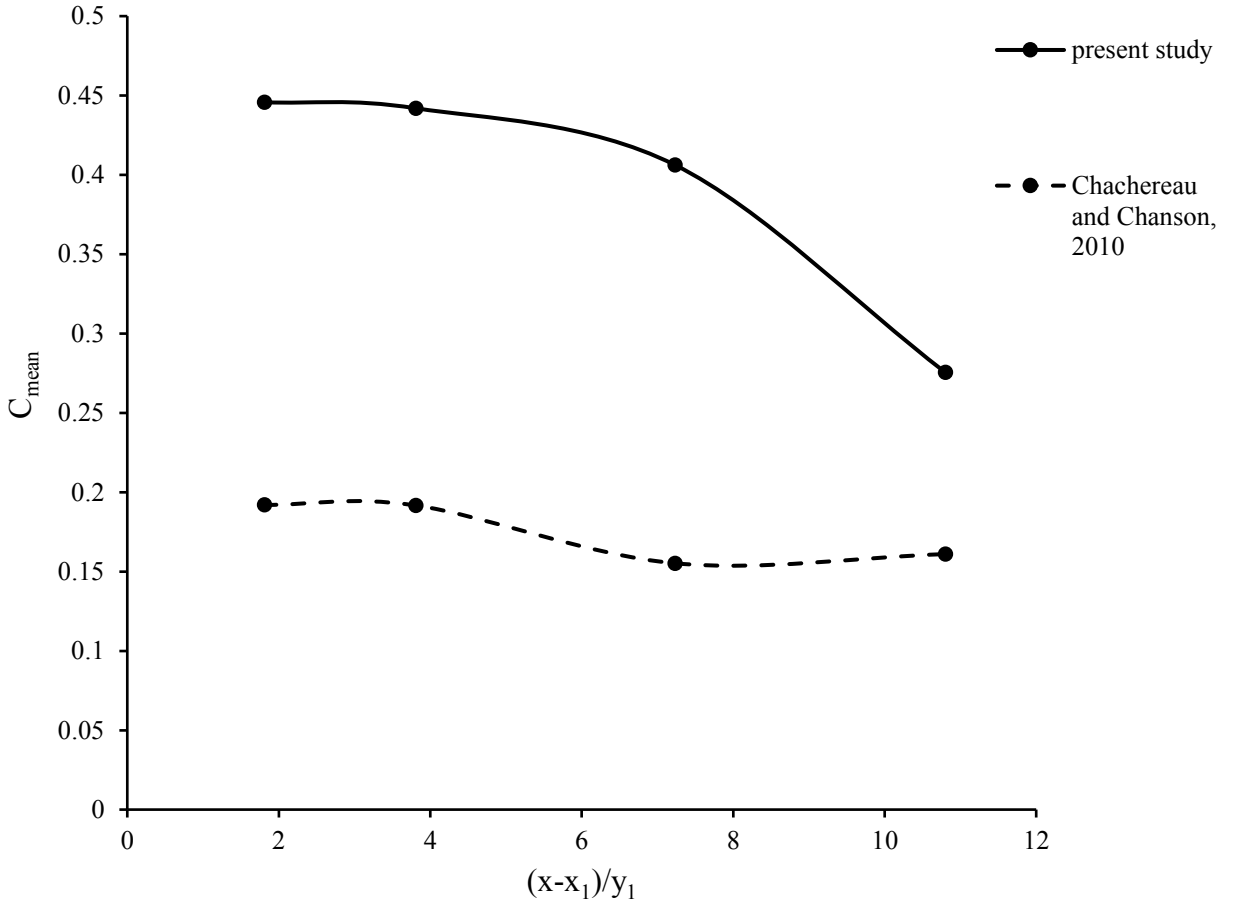

Figure 4.18 Distributions of predicted and measured depth-averaged air volume fraction for simulation case 2. The upstream Froude number is $Fr_1 = 3.8$.

From simulation case 2 with $Fr_1 = 3.8$, the CFD model predicted a decrease in the depth-averaged, time-averaged air volume fraction, C_{mean}, monotonically with longitudinal distance from the jump toe (Figure 4.18), whereas the experimental data (Chachereau and Chanson, 2010) showed a decreases in C_{mean} with longitudinal distance up to $(x - x_1)y_1 \approx 7$, followed by a slight increase. The predicted values of C_{mean} are higher than the measured values. We interpret that a larger amount of air being entrained into the hydraulic jump in the simulation is due to the effect of the Reynolds number (Equation 2.10), which is larger in the simulation than in the experiments.

The CFD model produced distributions of the longitudinal velocity component, V_x, at different depth between the channel bottom and the free surface, which are difficult to measure from laboratory experiments. In Figure 4.19(a)-4.19(d), we show the time- averaged vertical distributions of V_x between the channel bottom and the height, at which the air volume fraction is

C ≥ 0.5, at four selected longitudinal locations. At each of the location, the maximum value of time - averaged V_x and the vertical distance above the channel bottom where the maximum value occurs are indicated. In Figure 4.19(b) and 4.19(c), V_x has negative values in the top portion of the profiles. These negative values mean reverse flow in the recirculation region immediately below the free water surface.

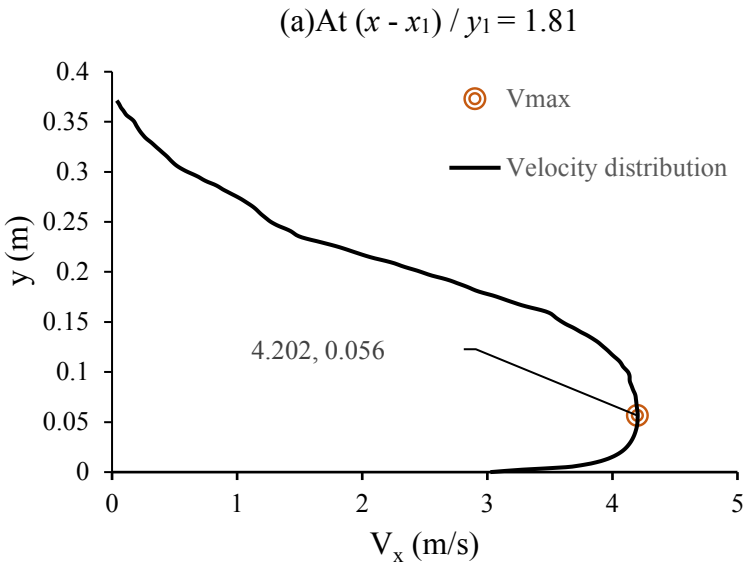

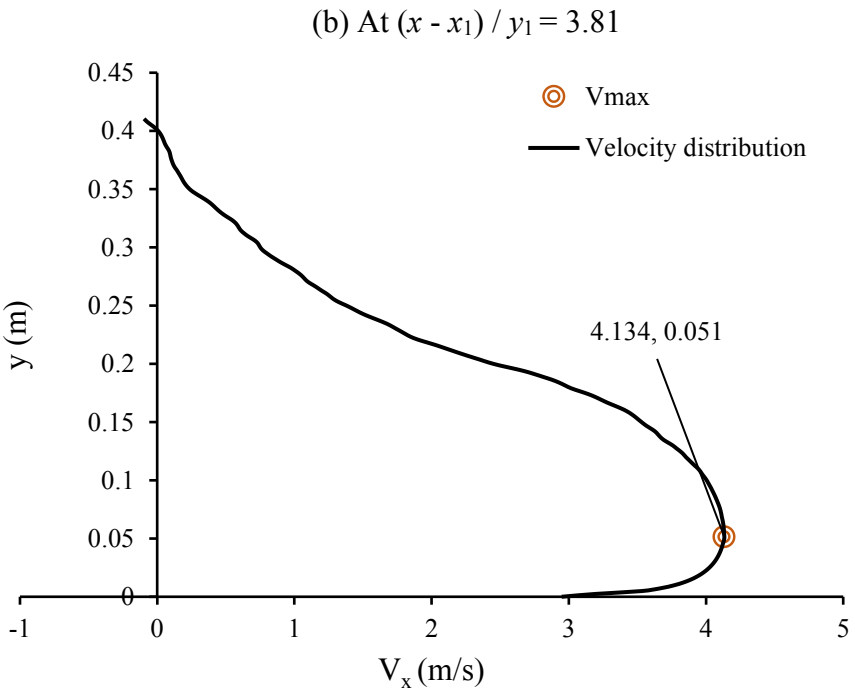

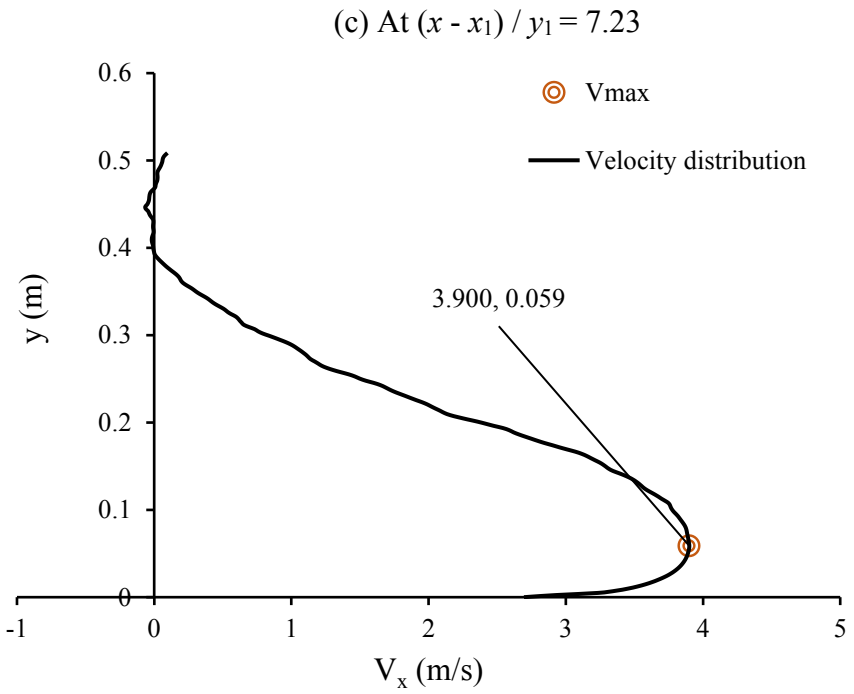

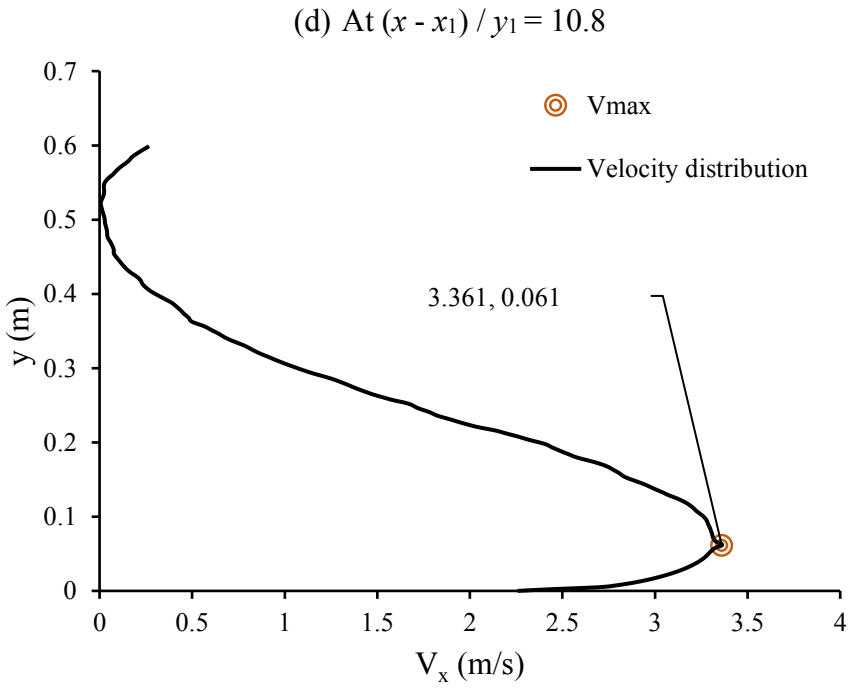

Figure 4.19 Vertical profiles of the time - averaged longitudinal velocity component below the free surface for simulation case 2, with $Fr_1 = 3.8$.

4.4.3 Simulation case 3

For simulation case 3, the upstream Froude number is $Fr_1 = 4.4$. The hydraulic jump is classified as form B, as discussed in Section 2.3. In Figure 4.20, contours of time averaged water volume fraction are shown. The location of the jump toe is $x_1 = 1.16$ m downstream of the inlet.

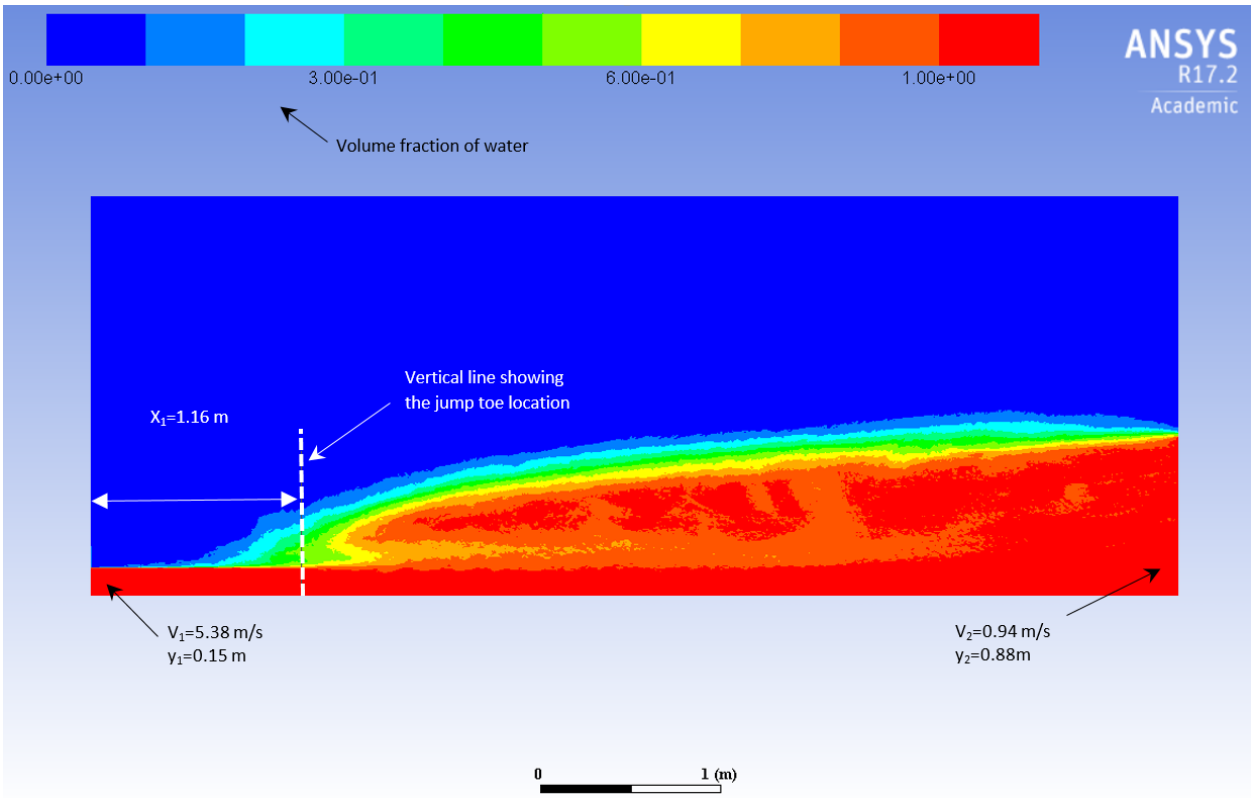

Figure 4.20 Time averaged distribution of water volume fraction for simulation case 3, in which the upstream Froude number is $Fr_1 = 4.4$.

In Figure 4.21, the distribution of flow velocity vectors, along with contours of time-averaged water volume fraction, at the last time step of the simulation, is plotted. The magnitudes of the vectors are shown by the lengths of the vectors. The colour scale for the vectors shows time-averaged water volume fraction. The water surface profile after the jump toe clearly defines a hydraulic jump.

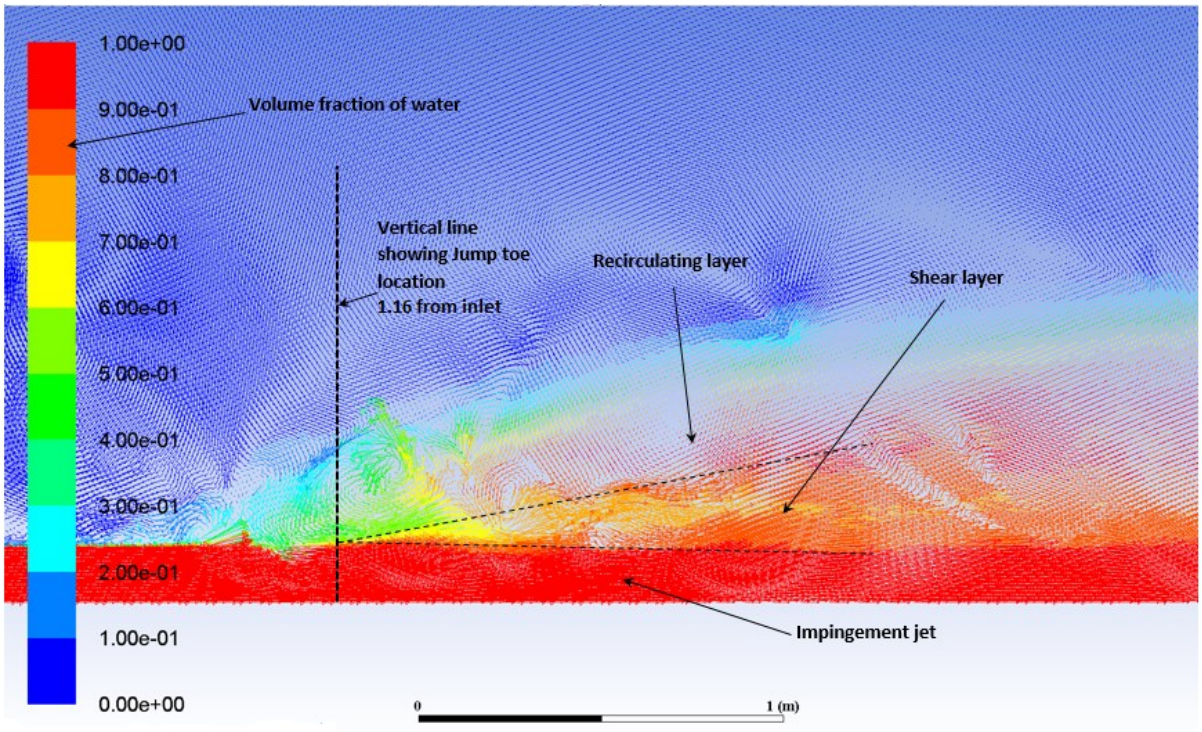

Figure 4.21 Distributions of flow velocity vectors and time-averaged water volume fraction in the hydraulic jump for simulation case 3. The upstream Froude number is $Fr_1 = 4.4$ (Table 4.1 and Table 4.2)

In Figures 4.22 to 4.24, we plotted vertical profiles of predicted time-averaged air volume fraction at three selected locations (Table 4.5) along the length of the model channel downstream of the jump toe. The experimental data of Chachereau and Chanson (2010) are shown as solid circles in the Figures for comparison purposes. Note that the predictions and experimental data match in location in terms of $(x - x_1)/y_1$. In Figure 4.22, the predicted maximum air volume fraction occurs in the shear region (Figure 4.21), whose upper boundary is located at $y = 0.35$ m above the channel bottom. The maximum air volume fraction is equal to 0.26, and occurs at $y = 0.26$ m. The predicted profile (Figure 4.22) gives a depth-averaged air volume fraction of $C_{mean} = 0.29$ at $(x - x_1)/y_1 = 3.8$. C_{mean} is defined in Equation (4.1).

Table 4.5 Selected longitudinal locations for the examination of air entrainment and flow velocity pattern sampling lines for simulation case 3 (Tables 4.1 and 4.2). The distance of the jump toe from the inlet is 1.16 m.

Selected location	1	2	3
Distance from the inlet (m)	1.739	2.317	2.897

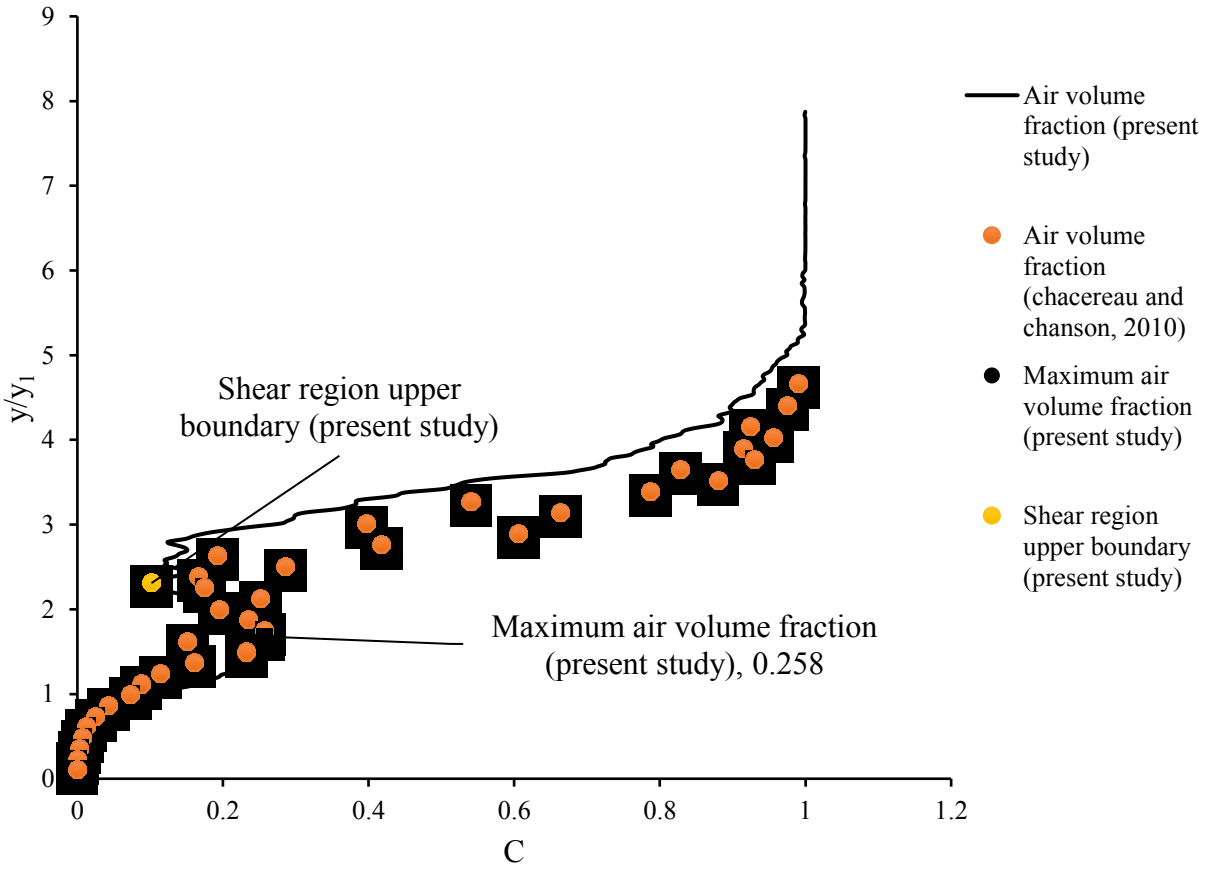

Figure 4.22 Vertical profile of time-averaged air volume fraction at $(x - x_1)/y_1 = 3.8$ for simulation case 3 with $Fr_1 = 4.4$.

In Figure 4.22, there is a good agreement between the CFD predictions and Chachereau and Chanson's (2010) measurements between the channel bottom and the upper boundary of the shear

region. Above the shear region, there are small discrepancies; at the same height (y/y_1), the CFD results give lower air volume fraction.

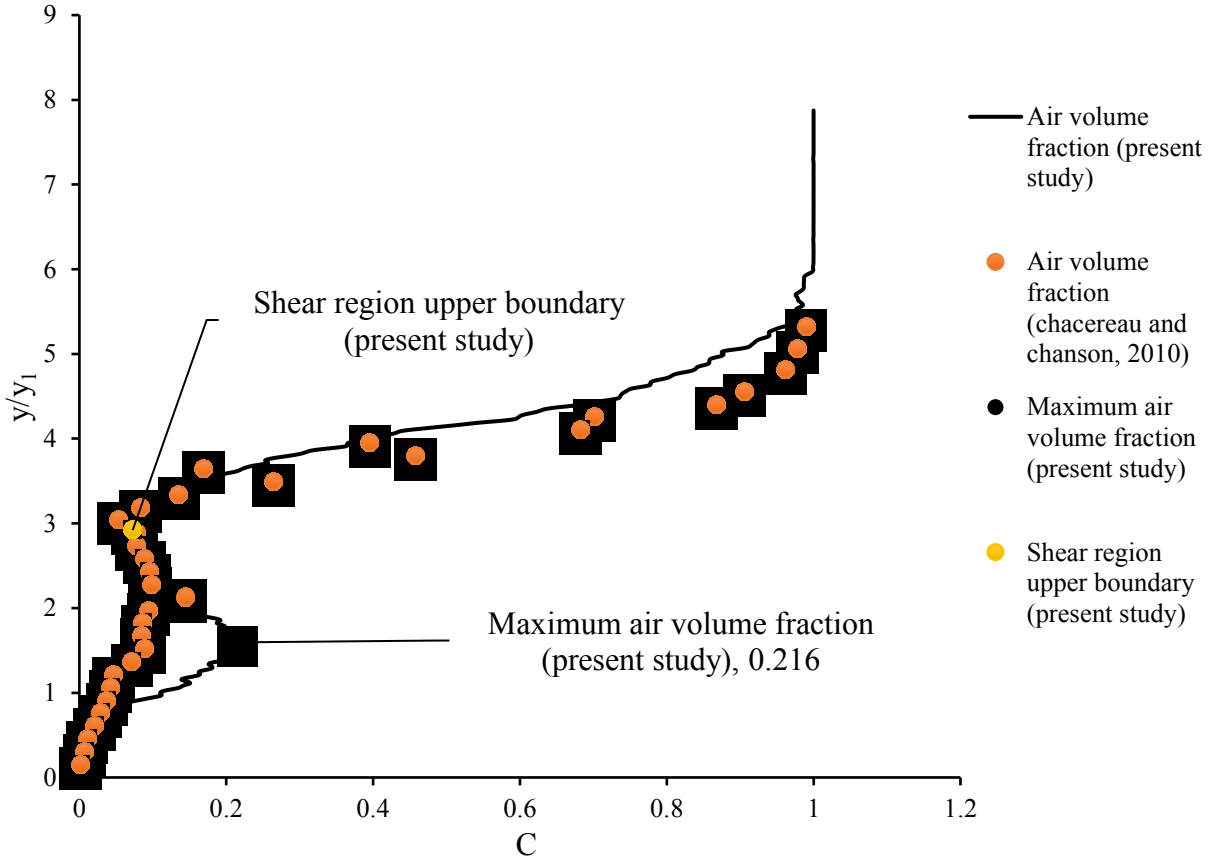

Figure 4.23 Vertical profile of time-averaged air volume fraction at $(x - x_1)/y_1 = 7.59$ for simulation case 3 with $Fr_1 = 4.4$.

In Figure 4.23, the predicted maximum air volume fraction is 0.22, occurring at y = 0.24 m in the shear region (Figure 4.21). The upper boundary of the shear region is located at 0.45 m above the channel bottom. The predicted profile (Figure 4.23) gives a depth-averaged air volume fraction of $C_{mean} = 0.25$ at $(x - x_1)/y_1 = 7.59$. There is a good agreement between the CFD results and the measurements except for the lower part of the shear region.

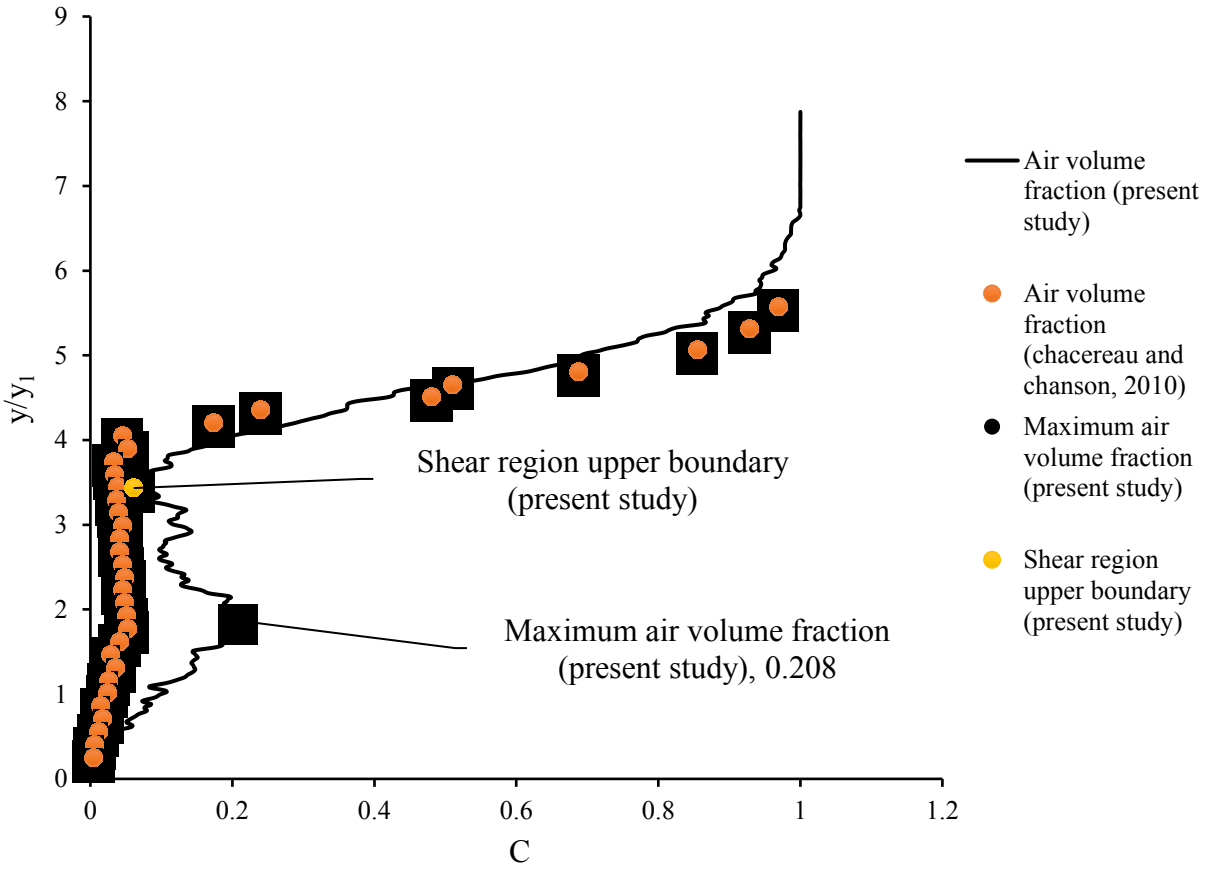

Figure 4.24 Vertical profile of time-averaged air volume fraction at $(x - x_1)/y_1 = 11.4$ for simulation case 3 with $Fr_1 = 4.4$.

In Figure 4.24, the predicted maximum air volume fraction is 0.21, occurring at y = 0.28 m in the shear region (Figure 4.21). The upper boundary of the shear region is located at 0.52 m above the bottom. The predicted profile (Figure 4.24) gives a depth-averaged air volume fraction of $C_{mean} = 0.24$ at $(x - x_1)/y_1 = 11.4$. There is a good agreement between the CFD results and the measurements above the shear region. In the shear region and below, the CFD simulation produced higher air volume fraction.

The vertical profiles (Figures 4.22 – 4.24) show variations in air volume fraction with depth below the water surface. For the analysis of hydraulic jumps, depth-averaged air volume fraction, C_{mean}, given in Equation (4.1), between the water surface and the channel bottom is a useful parameter. In Figure 4.25, we compare the predicted distribution of C_{mean} along the length of the

model channel with Chachereau and Chanson's (2010) experimental data. The predictions appear to give overestimates of C_{mean} values.

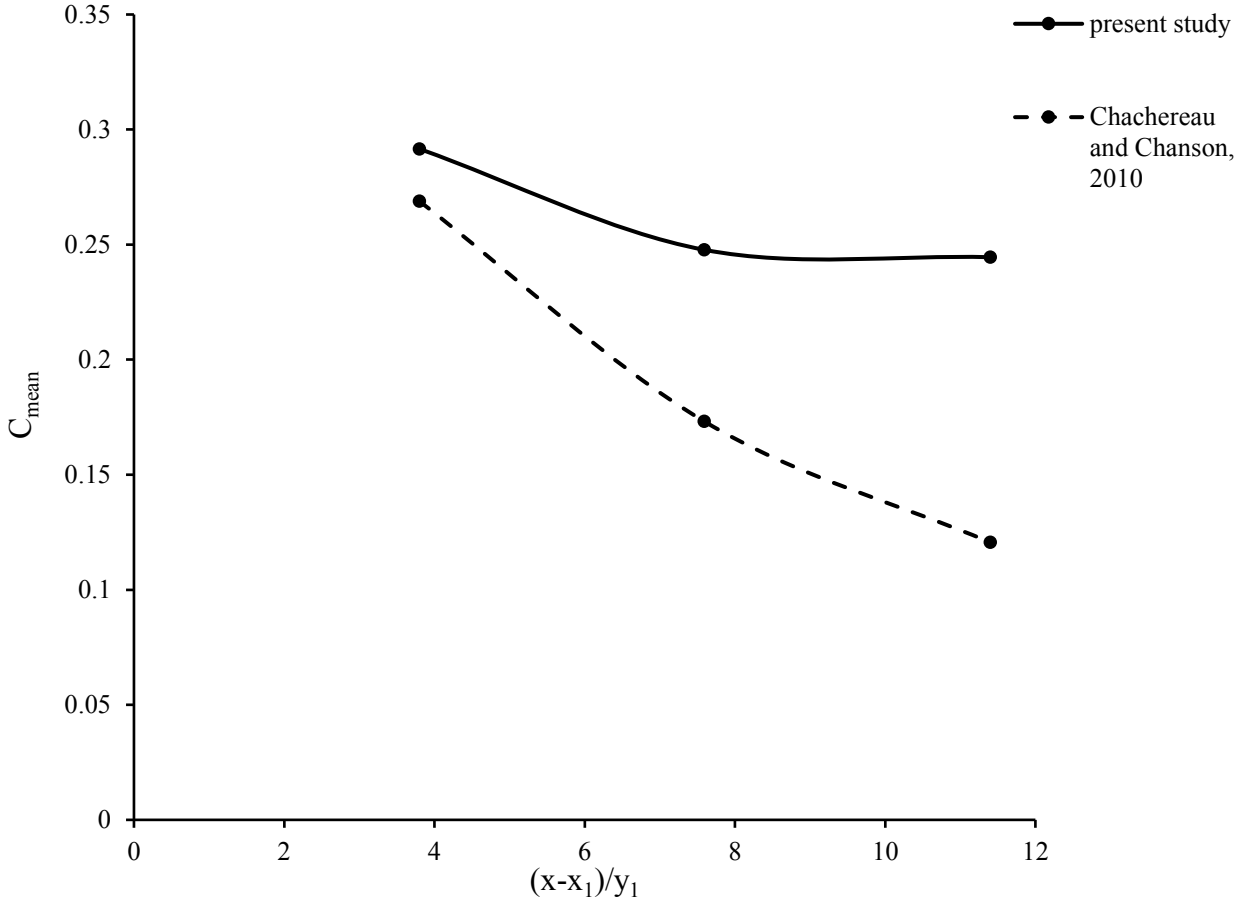

Figure 4.25 Distributions of predicted and measured depth-averaged air volume fraction for simulation case 3. The upstream Froude number is $Fr_1 = 4.4$

In Figure 4.25, for $Fr_1 = 4.4$, both the CFD predictions and measurements show a decrease in the double averaged C_{mean} with longitudinal distance from the jump toe. The predicted values of C_{mean} are higher than the measured values. These differences can be attributed to the different Reynolds number between the simulation and the experiments.

The CFD model produced distributions of the longitudinal velocity component, V_x, at different depth between the channel bottom and the free surface, which are difficult to measure from laboratory experiments. In Figure 4.26(a)-4.26(c), we show the time- averaged vertical distributions of V_x between the channel bottom and the height, at which the air volume fraction is $C \geq 0.5$, at three selected longitudinal locations. At each of the location, the maximum value of

time - averaged V_x and the vertical distance above the channel bottom where the maximum value occurs are indicated. In Figure 4.19(a) - 4.19(c), V_x has negative values in the top portion of the profiles. These negative values mean reverse flow in the recirculation region immediately below the free water surface.

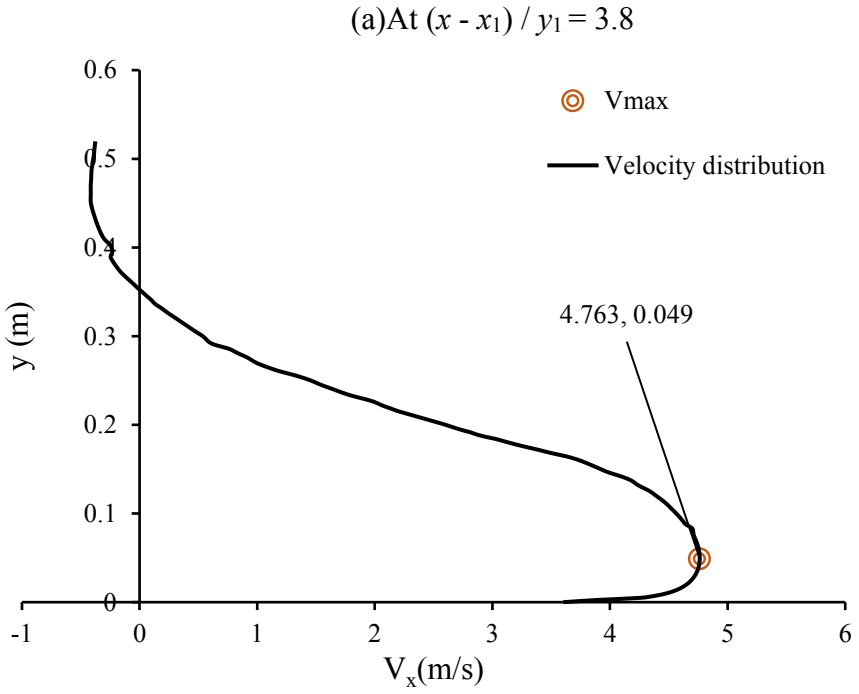

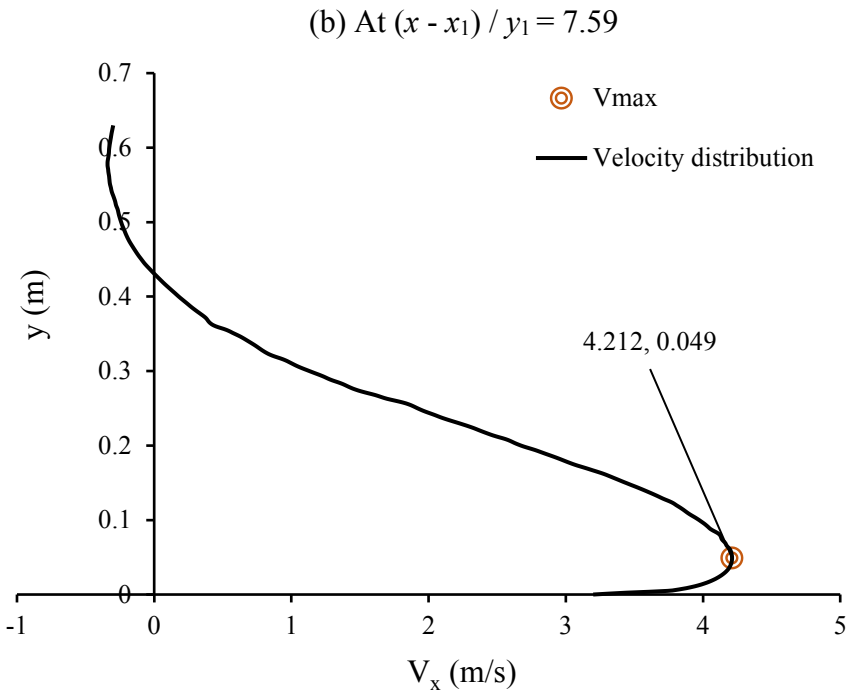

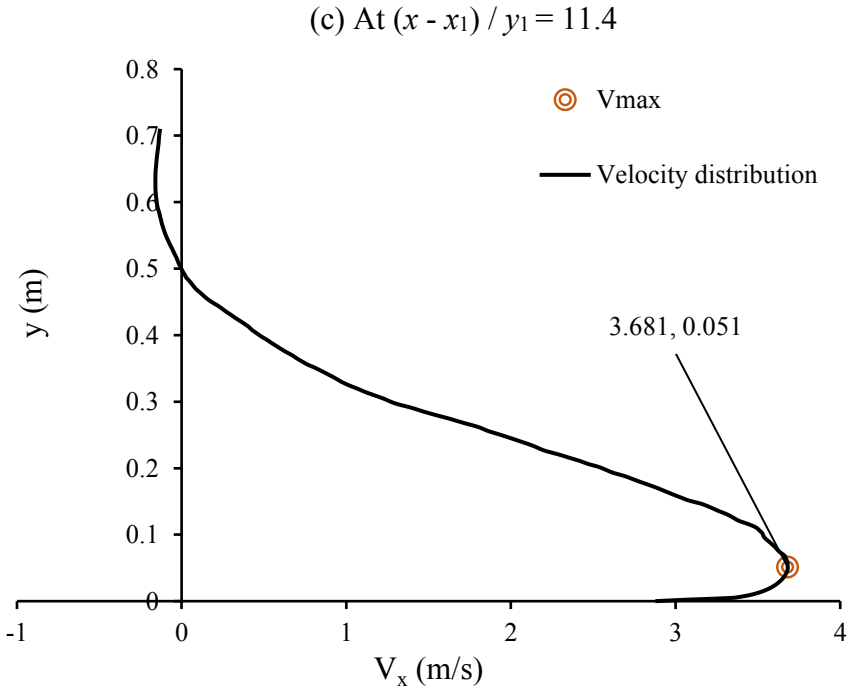

Figure 4.26 Vertical profiles of the time - averaged longitudinal velocity component below the free surface for simulation case 1, with $Fr_1 = 3.1$.

4.4.4 Simulation case 4

For simulation case 4, the upstream Froude number is $Fr_1 = 5.1$. The hydraulic jump is classified as form C, as discussed in Section 2.3. In Figure 4.27, contours of time averaged water volume fraction are shown. The location of the jump toe is $x_1 = 0.41$ m downstream of the inlet.

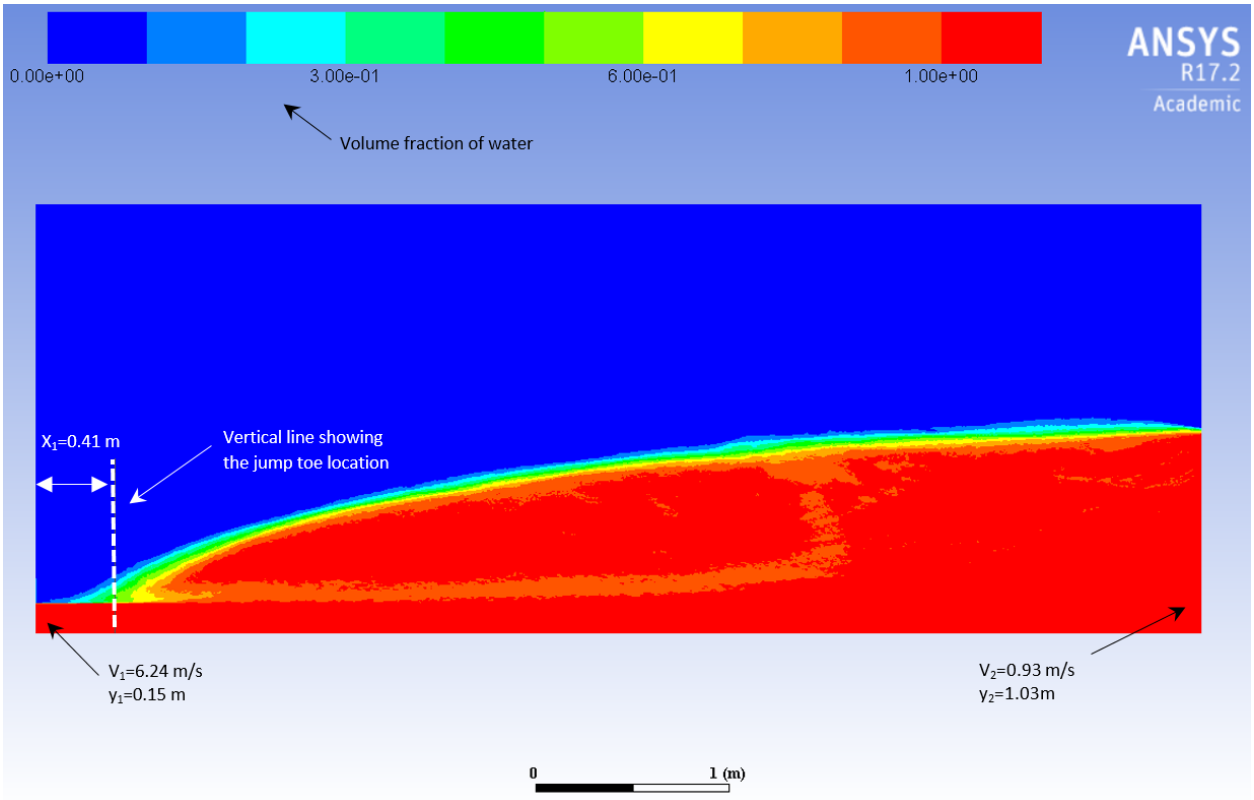

Figure 4.27 Time averaged distribution of water volume fraction for simulation case 4, in which the upstream Froude number is $Fr_1 = 5.1$.

In Figure 4.28, the distribution of flow velocity vectors, along with contours of time-averaged water volume fraction, at the last time step of the simulation, is plotted. The magnitudes of the vectors are shown by the lengths of the vectors. The colour scale for the vectors shows time-averaged water volume fraction. The water surface profile after the jump toe clearly defines a hydraulic jump.

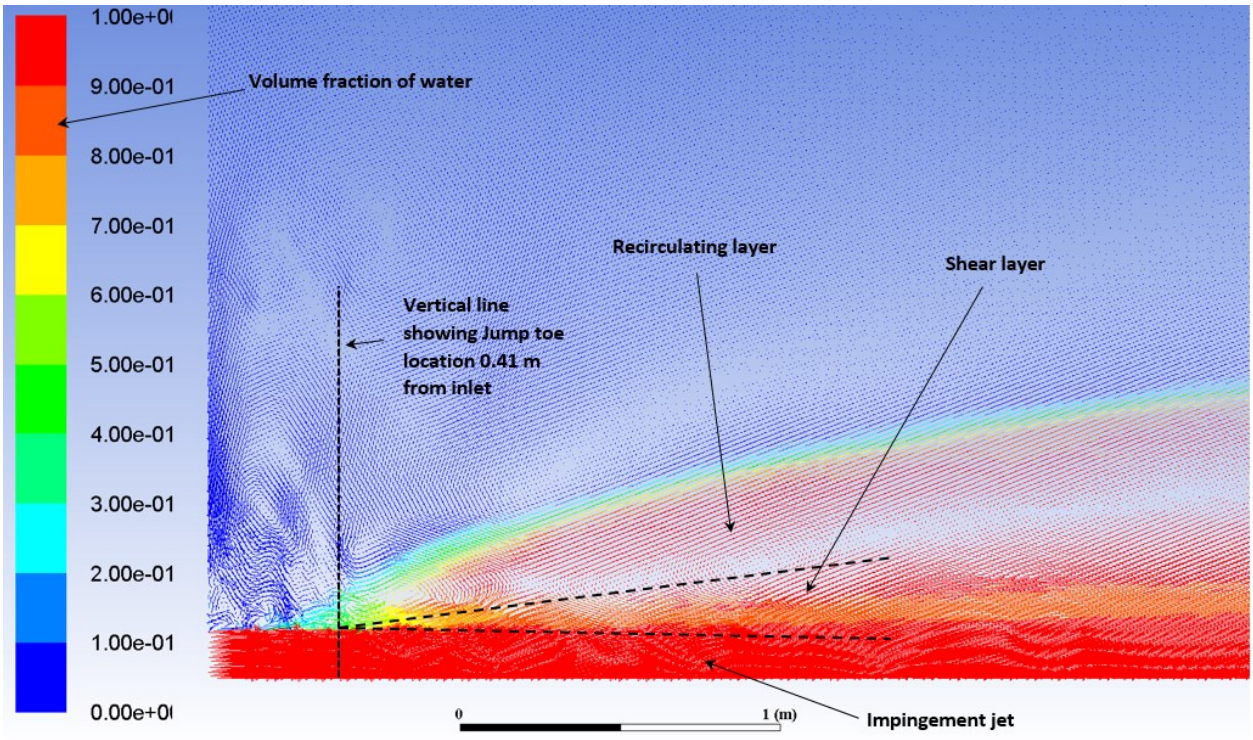

Figure 4.28 Distributions of flow velocity vectors and time-averaged water volume fraction in the hydraulic jump for simulation case 4. The upstream Froude number is $Fr_1 = 5.1$ (Table 4.1 and Table 4.2)

In Figures 4.29 to 4.32, we plotted vertical profiles of predicted time-averaged air volume fraction at four selected locations (Table 4.6) along the length of the model channel downstream of the jump toe. The experimental data of Chachereau and Chanson (2010) are shown as solid circles in the Figures for comparison purposes. Note that the predictions and experimental data match in location in terms of $(x - x_1)/y_1$. In Figure 4.29, the predicted maximum air volume fraction occurs in the shear region (Figure 4.28), whose upper boundary is located at $y = 0.32$ m above the channel bottom. The maximum air volume fraction is equal to 0.19, and occurs at $y = 0.19$ m. The predicted profile (Figure 4.29) gives a depth-averaged air volume fraction of $C_{mean} = 0.16$ at $(x - x_1)/y_1 = 3.8$. C_{mean} is defined in Equation (4.1).

Table 4.6 Selected longitudinal locations for the examination of air entrainment and flow velocity pattern sampling lines for simulation case 4 (Tables 4.1 and 4.2). The distance of the jump toe from the inlet is 0.41 m.

Selected location	1	2	3	4
Distance from the inlet (m)	0.989	1.567	2.147	2.726

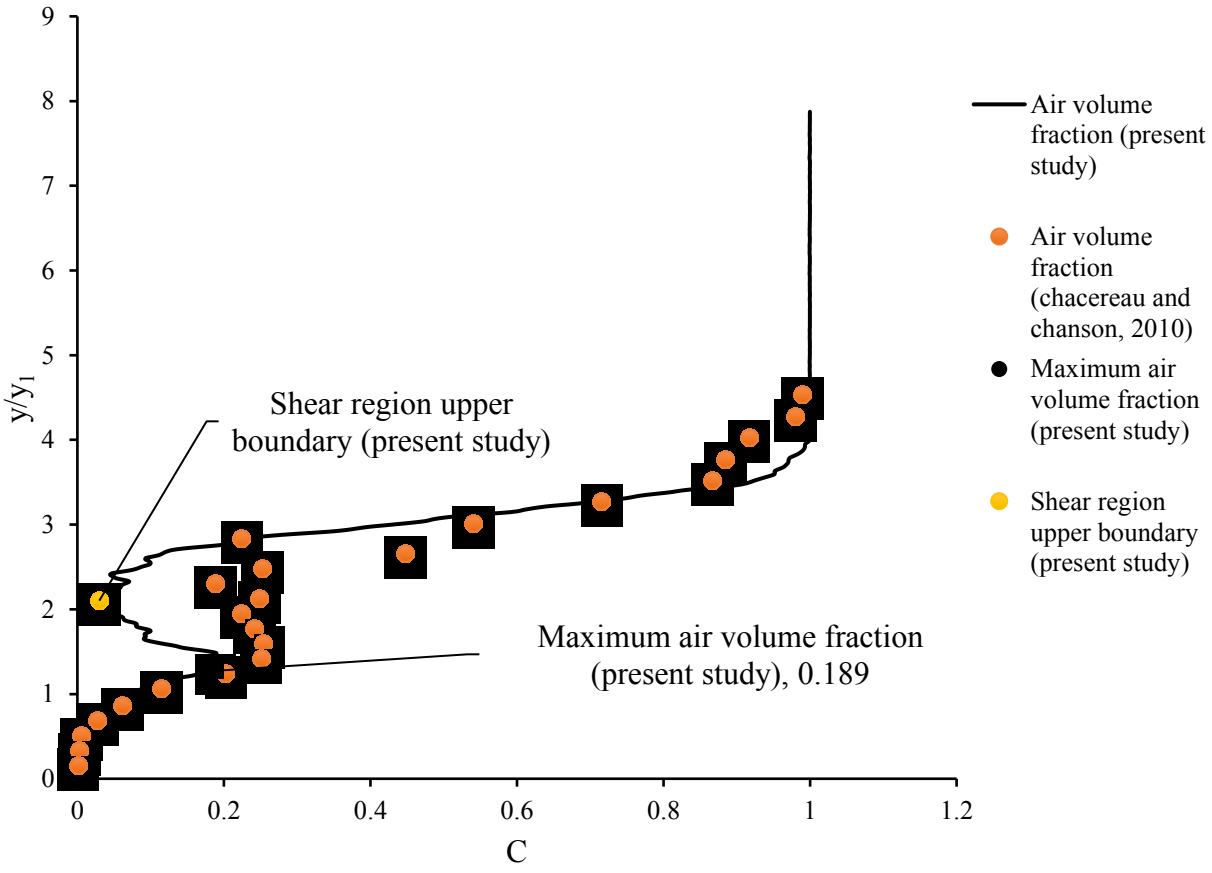

Figure 4.29 Vertical profile of time-averaged air volume fraction at $(x - x_1)/y_1 = 3.8$ for simulation case 4 with $Fr_1 = 5.1$.

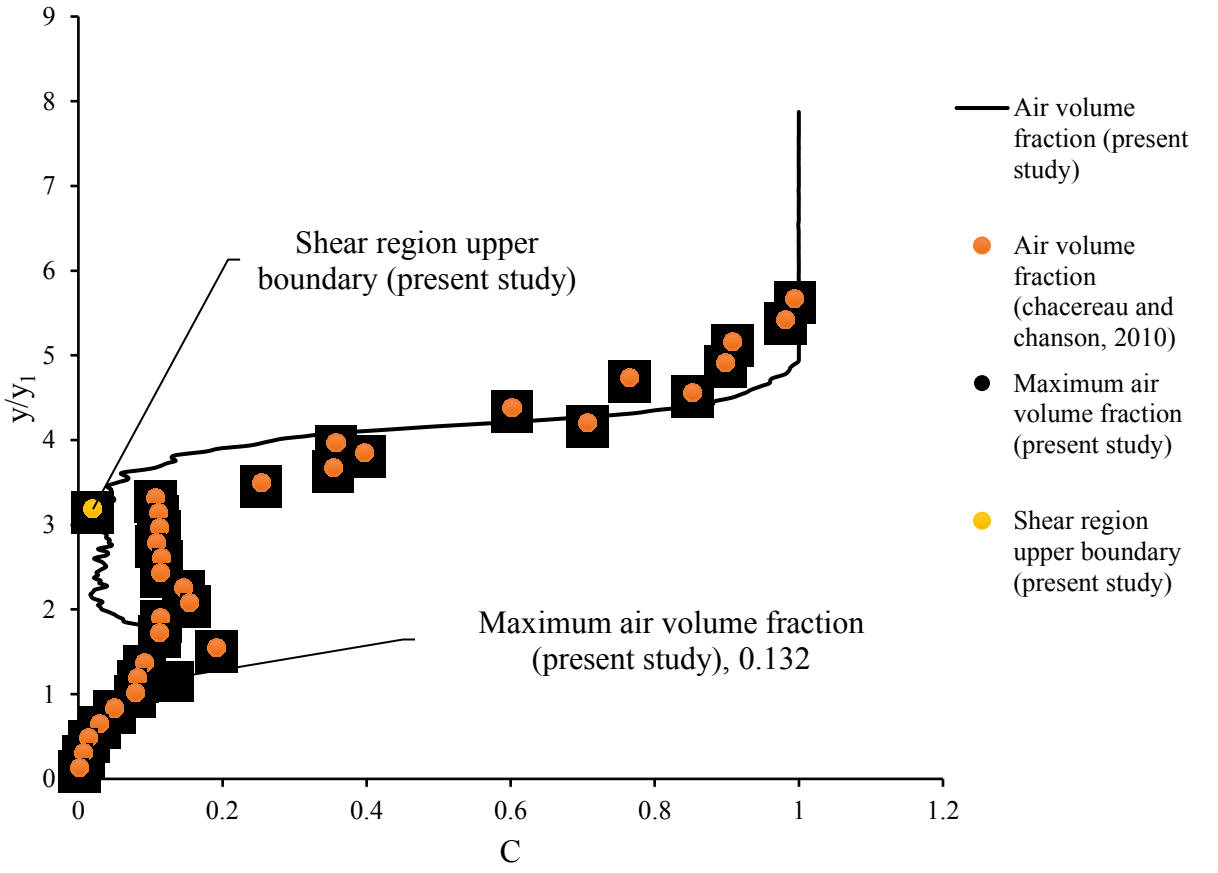

Figure 4.30 Vertical profile of time-averaged air volume fraction at $(x - x_1)/y_1 = 7.59$ for simulation case 4 with $Fr_1 = 5.1$.

In Figure 4.30, the predicted maximum air volume fraction is 0.13, occurring at y = 0.18 m in the shear region (Figure 4.28). The upper boundary of the shear region is located at 0.49 m above the channel bottom. The predicted profile (Figure 4.30) gives a depth-averaged air volume fraction of $C_{mean} = 0.12$ at $(x - x_1)/y_1 = 7.59$.

In Figures 4.29 and 4.30, the CFD predictions are in a good agreement with Chachereau and Chanson's (2010) measurements except for the upper part of the shear region. The discrepancies for the upper part of shear region are possibly due to the scale effect. Chachereau and Chanson's (2010) experiments used a setup of smaller dimensions, as explained in Section 4.4.2.

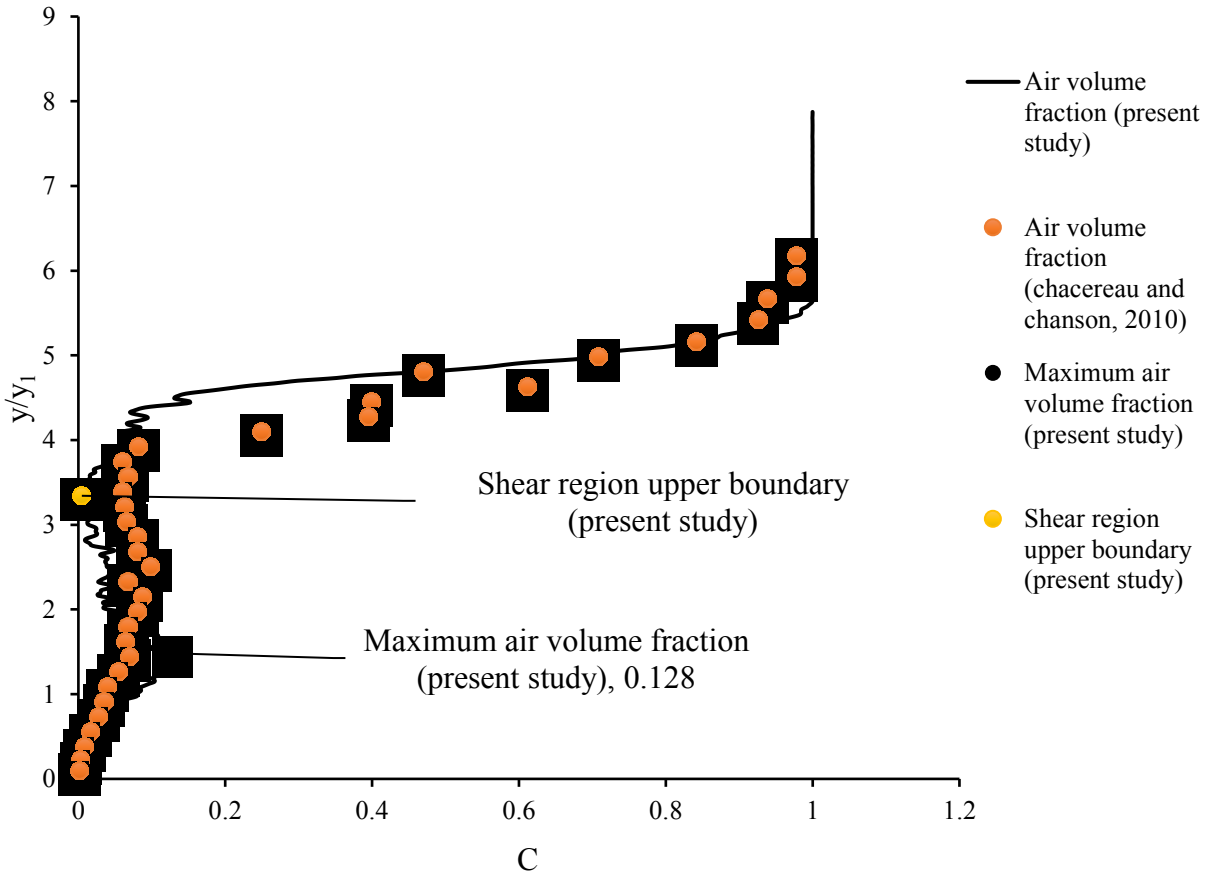

Figure 4.31 Vertical profile of time-averaged air volume fraction at $(x - x_1)/y_1 = 11.4$ for simulation case 4 with $Fr_1 = 5.1$.

In Figure 4.31, the predicted maximum air volume fraction is 0.13, occurring at y = 0.23 m in the shear region (Figure 4.28). The upper boundary of the shear region is located at 0.51 m above the bottom. The predicted profile (Figure 4.31) gives a depth-averaged air volume fraction of $C_{mean} = 0.11$ at $(x - x_1)/y_1 = 11.4$.

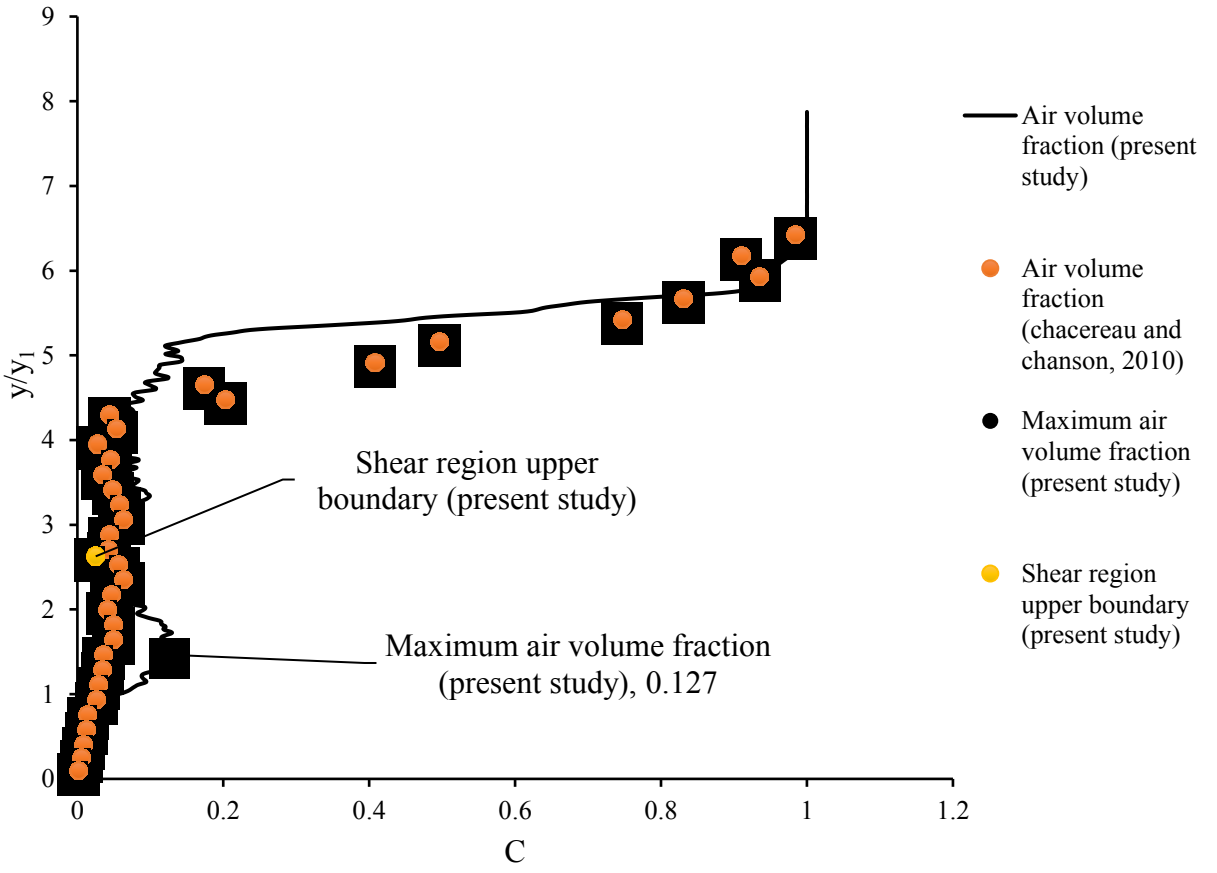

Figure 4.32 Vertical profile of time-averaged air volume fraction at $(x - x_1)/y_1 = 15.2$ for simulation case 4 with $Fr_1 = 5.1$.

In Figure 4.32, the predicted maximum air volume fraction is 0.13, occurring at y = 0.22 m in the shear region. The upper boundary of shear region from the channel bottom is located at 0.40 m. Below the water surface, the predicted profile (Figure 4.9) gives a depth-averaged air volume fraction of $C_{mean} = 0.11$ at $(x - x_1)/y_1 = 15.2$. In Figures 4.31 and 4.32, there is a very good agreement between the CFD predictions and laboratory measurements.

The vertical profiles (Figures 4.29 – 4.32) show variations in air volume fraction with depth below the water surface. For the analysis of hydraulic jumps, depth-averaged air volume fraction, C_{mean}, given in Equation (4.1), between the water surface and the channel bottom is a useful parameter. In Figure 4.10, we compare the predicted distribution of C_{mean} along the length of the model channel with Chachereau and Chanson's (2010) experimental data. The predictions appear to give lower values of C_{mean}.

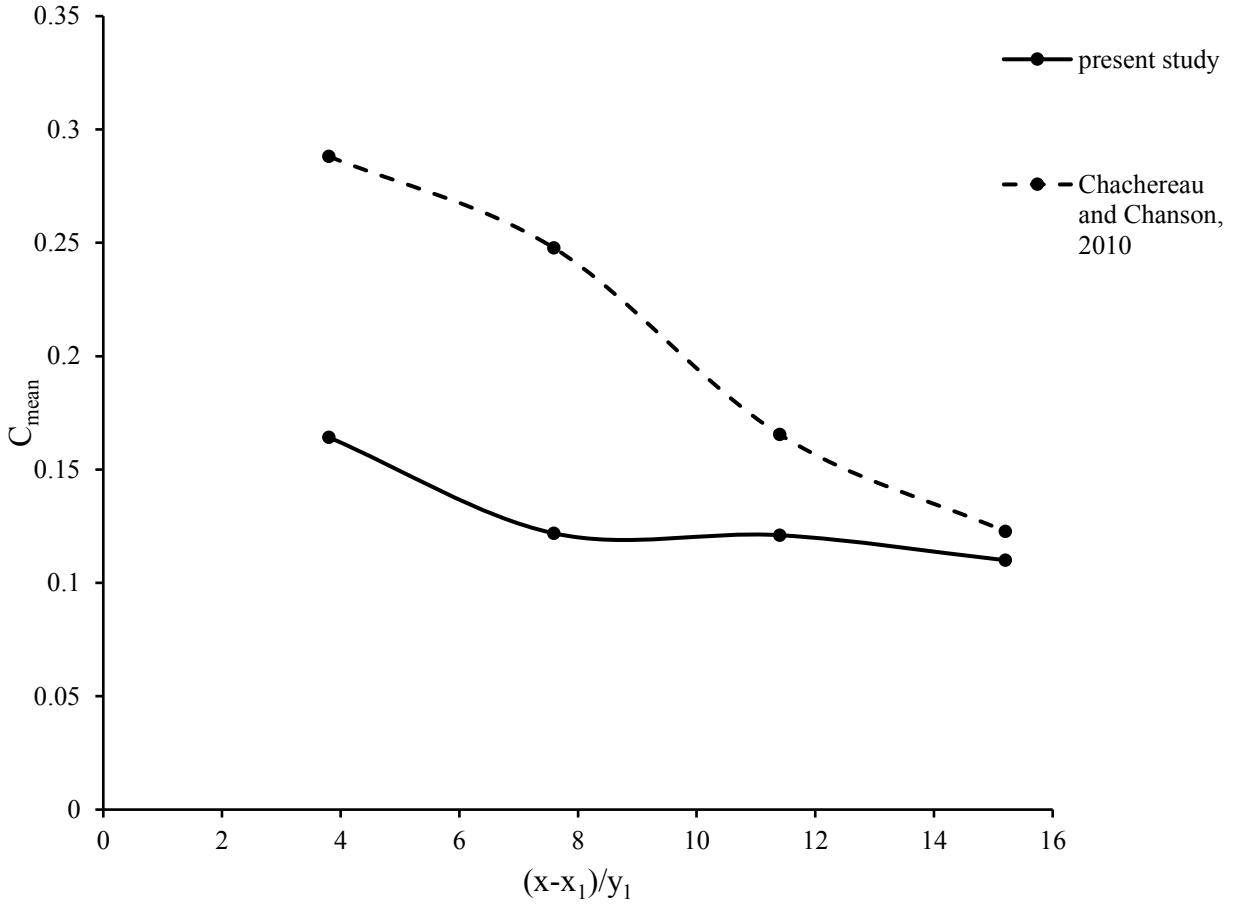

Figure 4.33 Distributions of predicted and measured depth-averaged air volume fraction for simulation case 4. The upstream Froude number is $Fr_1 = 5.1$.

In Figure 4.33, for $Fr_1 = 5.1$, the double averaged air volume fraction, C_{mean}, is shown to decrease with increasing longitudinal distance from the jump toe, both in the simulation and in the experiments. The simulation produced lower values of C_{mean} than the experiments. This is opposite to the previous comparisons for simulation cases 1, 2 and 3, where the hydraulic jumps are oscillating jumps, belonging to B group. With $Fr_1 = 5.1$, the hydraulic jump is stable jump. For stable jumps, it is possible that a higher Reynolds number does not necessarily lead to an increase in entrainment of air into the flow.

The CFD model produced distributions of the longitudinal velocity component, V_x, at different depth between the channel bottom and the free surface, which are difficult to measure from laboratory experiments. In Figure 4.34(a)-4.34(d), we show the time- averaged vertical distributions of V_x between the channel bottom and the height, at which the air volume fraction is

C ≥ 0.5, at four selected longitudinal locations. At each of the location, the maximum value of time - averaged V_x and the vertical distance above the channel bottom where the maximum value occurs are indicated. In Figure 4.34(a)-4.34(d), V_x has negative values in the top portion of the profiles. These negative values mean reverse flow in the recirculation region immediately below the free water surface.

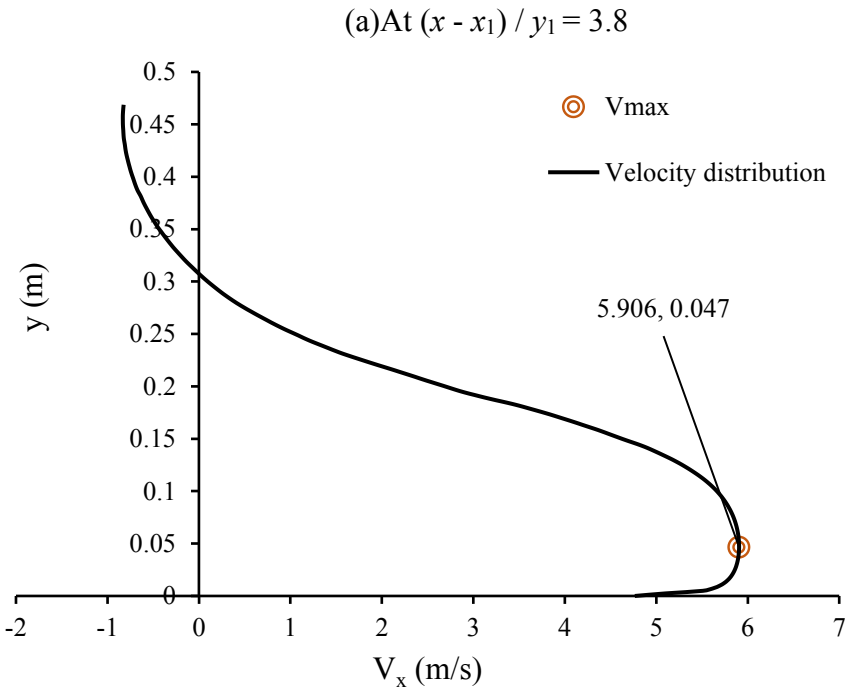

(b)At $(x - x_1) / y_1 = 7.59$

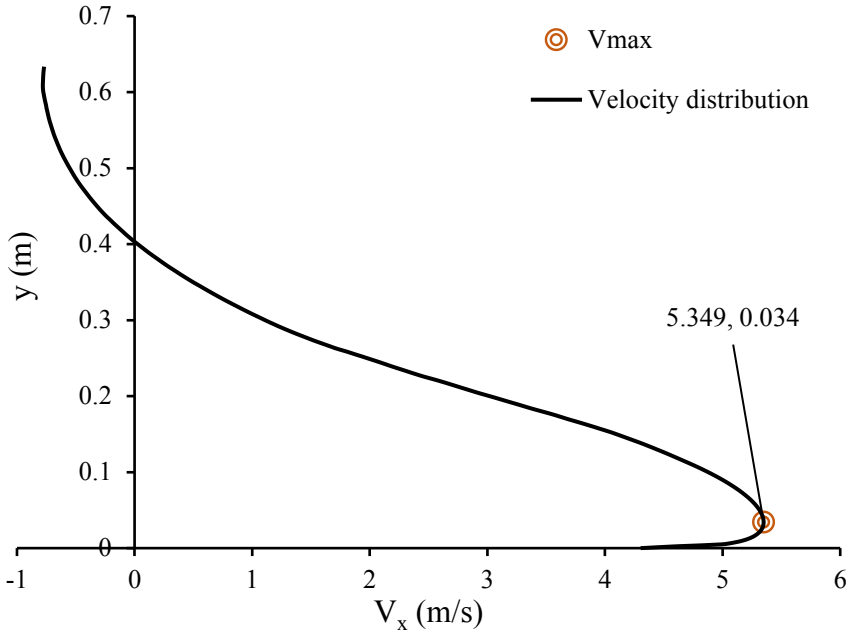

(c)At $(x - x_1) / y_1 = 11.4$

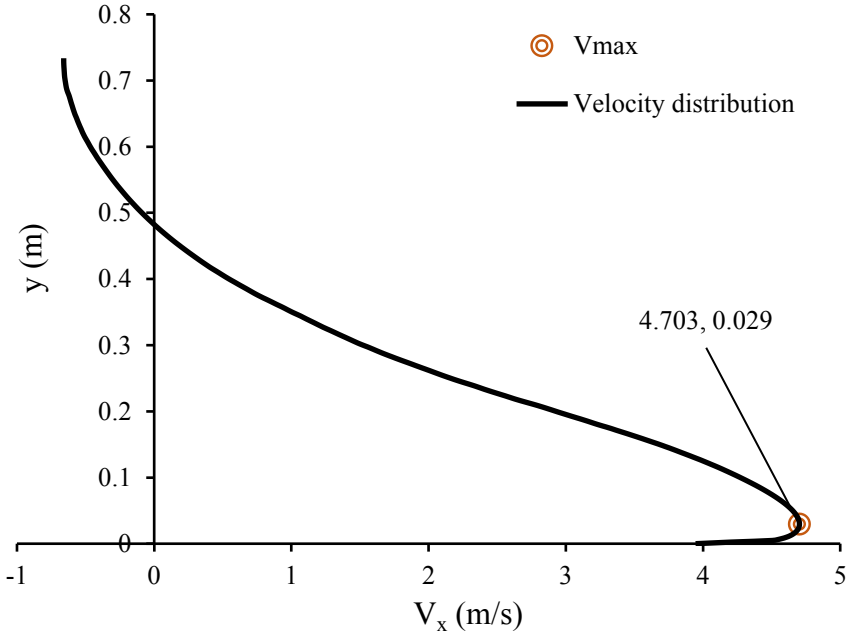

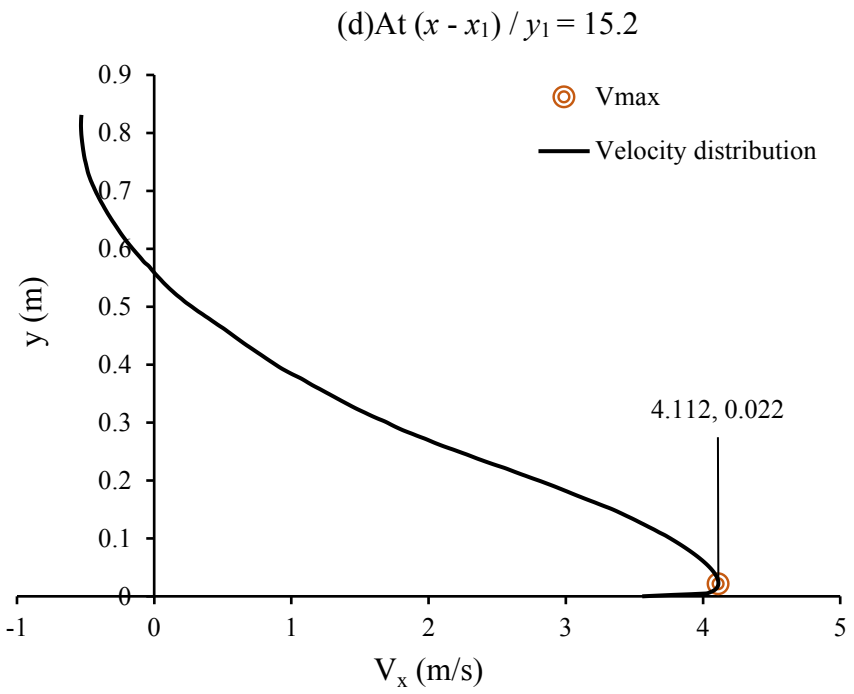

Figure 4.34 Vertical profiles of the time - averaged longitudinal velocity component below the free surface for simulation case 4, with $Fr_1 = 5.1$.

4.5 Summery

For the four simulation cases, distributions of air entrainment and flow velocity are summarised below: The predicted distributions from this study are consistent with the general characteristics reported in earlier studies of hydraulic jumps [Figures 4.3(a) and 4.3(b)]. Except for simulation case 2, there is a good agreement between predictions of vertical distributions of air volume fraction and Chachereau and Chanson's (2010) measurements. As for the discrepancies for simulation case 2, it is possible that the measurements in some regions of the jump contain significant errors. The measurement data points are seen to scatter to a large extent, which shows significant limitations of a laboratory model for hydraulic jump experiments.

For all four simulation cases, the maximum air volume fraction, C_{max}, occurs in the shear layer, and the maximum volume fraction decreases with increasing longitudinal distance from the jump toe. This decreasing trend is shown in Figure 4.35. The double averaged air volume fraction, C_{mean}, decreases with increasing distance from the jump toe. This can be interpreted by the buoyancy of air bubbles. As air bubbles move toward downstream, they rise upward toward the free surface and de-aeration is expected to occur.

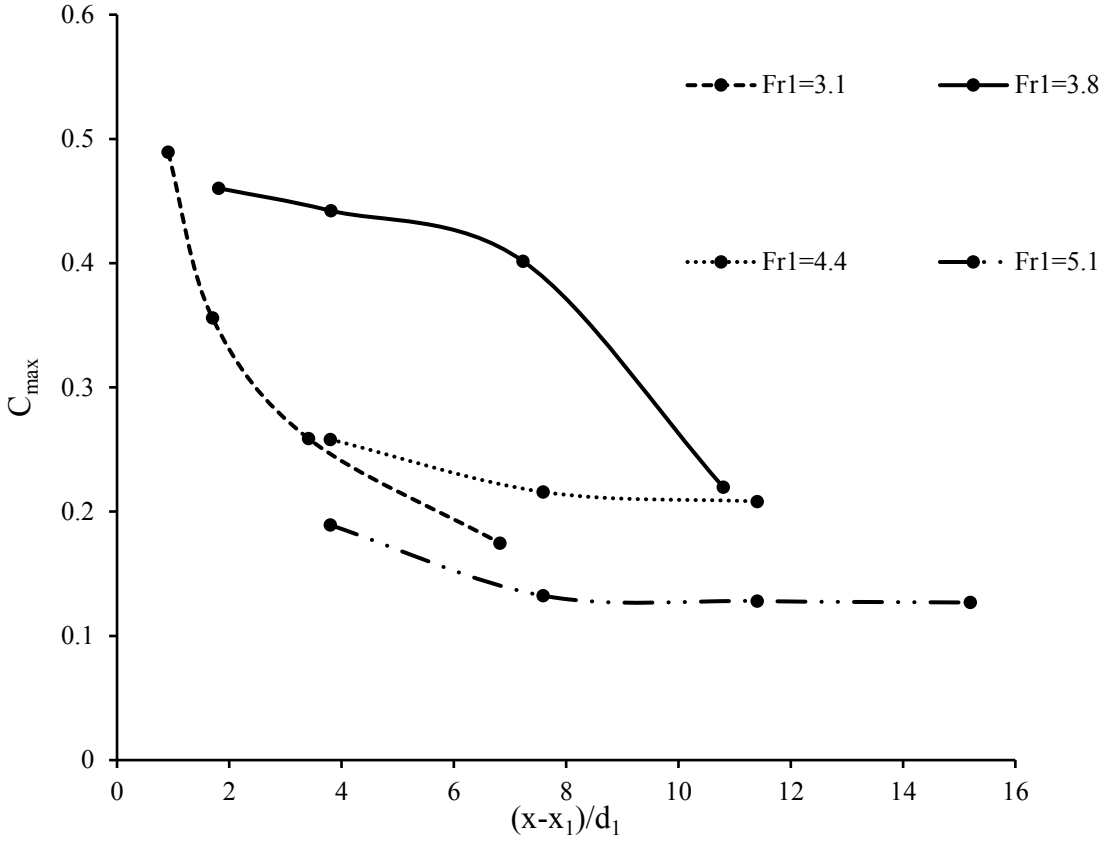

Figure 4.35 The maximum air volume fraction in the shear region in different distances from the jump toe in all four test cases in the present study

For the first three simulation cases with the approach flow Froude number Fr_1 = 3.1 to 4.4, the predicted C_{mean} values are higher than the measured values from Chachereau and Chanson (2010). The differences are possibly due to the depth of approach flow is larger in our simulations than in their experiments. Note that a larger depth corresponds to a larger Reynolds number, which is a fundamental dimensionless parameter for turbulence. Thus, for Fr_1 = 3.1 to 4.4, the amount of air that enters the hydraulic jump appears to be proportional the vertical dimension of the approach flow.

This proportional relationship ceases to exist when the Froude number exceeds a certain threshold. For example, for simulation case 4 (with Fr_1 = 5.1), predicted C_{mean} values are plotted below the corresponding measured values. This means a decrease in the amount of air entrainment with an increase in the vertical dimension of the approach flow (or equivalently the hydraulic jump) from the laboratory channel (Chachereau and Chanson, 2010) to the model channel (this study). This inverse relationship between average air entrainment and the vertical dimension of

the hydraulic jump can be true for jumps at $Fr_1 > 5.1$. It must be noticed that this generalisation needs further verifications for a wide range of hydraulic jumps at various Froude numbers and dimensions.

Note that the processes that are responsible for producing spray above the water free surface are not taken to account in the CFD simulations of this research. In fact, 2.5-mm mesh resolutions are inadequate to resolve spray.

Chapter 5 Conclusions

5.1 Concluding remarks

This thesis reports a successful computational fluid dynamics (CFD) investigation of hydraulic jumps as two-phase flow, with air as the gas phase and water as the liquid phase. The two-phase flow treatment much more closely reflects a real-world hydraulic jump than the traditional approach, which considers hydraulic jumps as pure water flow and ignores the presence of air bubbles in the flow. In this research work, the computational domain is a two-dimensional, flat-bottom model channel of 6 m long and 2.2 m deep. These dimensions are large, in comparison to the typical channel dimensions in earlier studies of hydraulic jumps.

The model channel is covered with rectangular finite volume mesh of high resolutions, being approximately 2.5 mm in both the longitudinal and vertical directions. The mesh consists of more than two million computing nodes. The use of such high resolutions has enabled us to capture the flow details of hydraulic jumps. This is important because hydraulic jumps are rapidly varied flow. The computations use the volume of fluid method for tracking the free surface, and the standard k-ε model for turbulence closure. For given hydraulic conditions, the computations produce finite volume solutions to the Reynolds-averaged continuity and momentum equations.

The hydraulic conditions used in the computations are such that the approach flow Froude number Fr_1 is in the range of 3.1 to 5.1, the depth of approach flow is 15.24 cm at the channel inlet, and the flow Reynolds number before the jump toe is in the range of 577662 to 950347. It is worth noting that the approach flow depth of 15.24 cm is an order of magnitude higher than that commonly used in earlier studies. The above-mentioned Reynolds numbers are high enough to reflect reality. This has proven to be difficult to achieve in laboratory experiments, which typically maintain Froude number similarity but scarify Reynolds number similarity with prototype models. From this perspective, this research work has produced computational results complementary to experimental data.

The computational results of air volume fraction are in a reasonable comparison with available experimental data. The computations are shown to produce distributions of time-averaged air volume fraction and flow velocity [Figures 4.3(a) and 4.3(b)], consistent with features reported in the literature. At a given longitudinal location, the vertical distribution of air volume fraction shows a local maximum value in the shear region. In the longitudinal direction toward

downstream, the local maximum air volume fraction decreases with increasing distance from the jump toe, and so does the average air entrainment in the jump.

A comparison of the computational results to the experimental data reveals the significant effects of the Reynolds number on air entrainment into hydraulic jumps. Up to a certain threshold value of the Froude number, higher Reynolds numbers appear to correspond to higher average air entrainment. In general, the effects of the Reynolds number in applications to open channel flow problems have not been investigated thoroughly.

Because of the typically unsteady nature of the hydraulic jump phenomenon, it is practical and necessary to apply time average to computational or experimental results. This is particularly true for oscillating hydraulic jumps, which is the case for the simulation with $Fr_1 = 3.8$ (simulation case 2). It is critical to accurately locate the jump toe. The uncertainties in locating the jump toe are much lower in the CFD simulations that in the laboratory experiments, for the simple reason that the simulations give continuous distributions of air-water volume fraction and flow velocity in each cell. We have successfully located the toes of highly dependent hydraulic jumps and obtained meaningful time averaged results.

This research work has demonstrated the advantage that CFD computations have the capability to simulating hydraulic jumps at high and practical Reynolds numbers (with minimal scale effects) in an efficient and cost-effective manner. Reliable simulation results have been obtained. As for the key to success, we used a very fine mesh and very small time step that are essential for accurate and stable calculations, and more importantly, appropriate strategies for modelling the air entrainment process.

5.2 Suggestions for future research

It is worthy of further investigations of the problem of hydraulic jumps by considering the following:

- Simulate two-dimensional hydraulic jumps for a wide range of Froude numbers, up to $Fr_1 = 9.0$ and at Reynolds numbers corresponding to laboratory experiments. This will facilitate direct comparisons between simulations and laboratory experiments.
- Perform three-dimensional simulations of hydraulic jumps because of the irregular nature of turbulence in three dimensions, which is responsible for air entrainment.

- Obtain simultaneous measurements of flow velocity and air entrainment for hydraulic jump experiments for validation of CFD predictions.
- To investigate air entrainment in hydraulic jump, in detail, for a wide range of upstream Reynolds numbers with values of upstream Froude numbers that matches available experiments.

References

Akan, A.O., 2011. Open channel hydraulics. Butterworth-Heinemann.

Brackbill, J.U., Kothe, D.B. and Zemach, C., 1992. A continuum method for modeling surface tension. Journal of computational physics, 100(2), pp.335-354.

Chachereau, Y. and Chanson, H., 2010. Free-surface Turbulent Fluctuations and Air-Water Flow Measurements in Hydraulic Jumps with Small Inflow Froude Numbers. School of Civil Engineeering, The University of Queensland.

Chanson, H. and Qiao, G.L., 1994. Air bubble entrainment and gas transfer at hydraulic jumps (No. CE149).

Chanson, H., 1995a. Air Bubble Entrainment in Free-Surface Turbulent Flows: Experimental Investigations (No. CH46/95).

Chanson, H., 1995b. Air entrainment in two-dimensional turbulent shear flows with partially developed inflow conditions. International Journal of Multiphase Flow, 21(6), pp.1107-1121.

Chanson, H., 1996. Air bubble entrainment in free-surface turbulent shear flows. Academic Press.

Chanson, H. and Brattberg, T., 1998, January. Air entrainment by two-dimensional plunging jets: the impingement region and the very-near flow field. In Proc. 1998 ASME Fluids Eng. Conf (pp. 21-25).

Chanson, H. and Brattberg, T., 2000. Experimental study of the air–water shear flow in a hydraulic jump. International Journal of Multiphase Flow, 26(4), pp.583-607.

Chanson, H., 2006. Air bubble entrainment in hydraulic jumps: Similitude and scale effects (No. CH57/05).

Chanson, H. and Murzyn, F., 2008. Froude similitude and scale effects affecting air entrainment in hydraulic jumps. In World Environmental and Water Resources Congress 2008: Ahupua'A (pp. 1-10).

Chanson, H., 2009. Current knowledge in hydraulic jumps and related phenomena. A survey of experimental results. European Journal of Mechanics-B/Fluids, 28(2), pp.191-210.

Fluent, A., 2013. 15.0: Theory guide, ansys. Inc., Canonsburg, PA.

Gualtieri, C. and Chanson, H., 2007. Experimental analysis of Froude number effect on air entrainment in the hydraulic jump. Environmental Fluid Mechanics, 7(3), pp.217-238.

Henderson, F.M., 1996. Open channel flow. Macmillan.

Hirt, C.W. and Nichols, B.D., 1981. Volume of fluid (VOF) method for the dynamics of free boundaries. Journal of computational physics, 39(1), pp.201-225.

Houghtalen, R.J., Osman, A. and Hwang, N.H., 2017. Fundamentals of hydraulic engineering systems. Prentice Hall.

Jasak, H., 2009. OpenFOAM: open source CFD in research and industry. International Journal of Naval Architecture and Ocean Engineering, 1(2), pp.89-94.

Launder, B.E. and Sharma, B.I., 1974. Application of the energy-dissipation model of turbulence to the calculation of flow near a spinning disc. Letters in heat and mass transfer, 1(2), pp.131-137.

Launder, B.E. and Spalding, D.B., 1974. The numerical computation of turbulent flows. Computer methods in applied mechanics and engineering, 3(2), pp.269-289.

Lin, C., Hsieh, S.C., Lin, I.J., Chang, K.A. and Raikar, R.V., 2012. Flow property and self-similarity in steady hydraulic jumps. Experiments in Fluids, 53(5), pp.1591-1616.

Ma, J., Oberai, A.A., Lahey, R.T. and Drew, D.A., 2011. Modeling air entrainment and transport in a hydraulic jump using two-fluid RANS and DES turbulence models. Heat and mass transfer, 47(8), p.911.

Murzyn, F., Mouaze, D. and Chaplin, J.R., 2005. Optical fibre probe measurements of bubbly flow in hydraulic jumps. International Journal of Multiphase Flow, 31(1), pp.141-154.

Rajaratnam, N., 1962. An experimental study of air entrainment characteristics of the hydraulic jump. J Inst Eng India, 42(7), pp.247-273.

Reclamation, U.B.O., 1987. Design of small dams. Water Resources Technical Publication, 860p.

Resch, F.J. and Leutheusser, E.H., 1972. Le ressaut hydraulique: mesures de turbulence dans la région diphasique. La Houille Blanche, (4), pp.279-293.

Reynolds, O., 1883. An experimental investigation of the circumstances which determine whether the motion of water shall be direct or sinuous, and of the law of resistance in parallel channels. Proceedings of the royal society of London, 35(224-226), pp.84-99.

Te Chow, V., 1959. Open channel hydraulics. McGraw-Hill Book Company, Inc; New York.

Walters, D.K. and Wolgemuth, N.M., 2009. A new interface-capturing discretization scheme for numerical solution of the volume fraction equation in two-phase flows. International journal for numerical methods in fluids, 60(8), pp.893-918.

Wang, H. and Chanson, H., 2015. Air entrainment and turbulent fluctuations in hydraulic jumps. Urban Water Journal, 12(6), pp.502-518.

Wilcox, D.C., 2006. Turbulence modeling for CFD (Vol. 1, 522 pages). La Canada, CA: DCW industries.

Witt, A., Gulliver, J. and Shen, L., 2015. Simulating air entrainment and vortex dynamics in a hydraulic jump. International Journal of Multiphase Flow, 72, pp.165-180.

Xiang, M., Cheung, S.C.P., Tu, J.Y. and Zhang, W.H., 2014. A multi-fluid modelling approach for the air entrainment and internal bubbly flow region in hydraulic jumps. Ocean Engineering, 91, pp.51-63.